Development and Application of Noncontact Near-Infrared Spectroscopy System for Measuring Biological Tissue

August 2012

A thesis submitted in partial fulfillment of the requirements for the degree of
Doctor of Philosophy in Engineering

Keio University
Graduate School of Science and Technology
School of Integrated Design Engineering

Funane, Tsukasa

Abstract

The *in vivo* application of near-infrared spectroscopy (NIRS) for brain-activity measurements was first described by Jöbsis in 1977. Over the past 35 years, this technique has been developed as a useful tool for the clinical monitoring of tissue oxygenation, for neuroimaging studies, and for the measurement of tissue structures. The NIRS system for detecting the absorption change in deep biological tissues must currently use contact fiber-optic probes on the skin in order to avoid artifacts induced by direct skin-reflected light or tissue movement. On the other hand, noncontact NIRS imaging may have many promising applications such as for monitoring the biological state of drivers and sleeping people. The purpose of this thesis is the development and application of a noncontact NIRS system.

To establish a noncontact NIRS system for the measurement of deep biological tissues, a noncontact brain activity measurement system using a phosphor which is excited by and emits near-infrared light was developed. To optimize and validate this system, the influence of the fluorescence lifetime on the amplitude of the lock-in detection was investigated to determine the optimal frequency of the light source's intensity modulation. The sensitivity of the system to the internal absorbance change was estimated using a phantom measurement. To clearly show that this system can detect the absorbance changes in the cerebral blood instead of those in the superficial regions, the hemoglobin changes in the same area of the prefrontal cortex were measured during a working memory task by simultaneously using this system and a conventional contact optical topography system. The precision of the system was also evaluated.

As an example of promising applications, the noncontact system was extended to a system with flexible source positions using a galvano scanner. An 808-nm laser, whose focal point on the surface of the biological tissue is controlled by the galvano scanner, is used as the light source. The system is used to measure twenty points on the tissue surface at which the source-detector (S-D) distances are 7–45 mm (with

2-mm intervals). Neither the light source nor the detector contacts the tissue surface. The system was validated by using it to measure the absorption change of an absorber (which is embedded in a deep layer of a tissue-simulating phantom) while the surface-layer thickness of the phantom was changed from 1 to 12 mm. It was demonstrated that both the relative absorption change of the absorber and the absolute thickness of the surface layer can be estimated from the measured optical-density change (ΔOD) and the dependence of the ΔOD on the S-D distance, respectively.

Combined with the multi-distance measurement, a dynamic phantom was developed for mimicking hemoglobin changes in the superficial and deep tissues, thus allowing us to experimentally validate the discrimination methods between the brain-scalp effects on the NIRS signal. In NIRS for monitoring brain activity and cerebral functional connectivity, the effect of the superficial tissue needs to be considered. Although some methods for determining the effect of scalp and brain have been proposed, direct validation of the methods has been difficult because the actual absorption changes are not known. In response to this problem, a dynamic phantom with two absorber layers that are independently driven by two one-axis automatic stages was developed. The phantom can be used to design any type of waveform (e.g., brain activity or systemic fluctuation) of an absorption change, which can then be reproducibly measured. To determine the effectiveness of the phantom, I used it for a multiple source-detector distance measurement. The performance of a subtraction method with a short-distance regressor was also investigated. The most accurate lower-layer change was obtained when a shortest-distance channel was used. Furthermore, when an independent component analysis was applied to the same data, the extracted components were in good agreement with the actual signals. These results demonstrated that the proposed phantom can be used for evaluating the methods of discriminating the effects of superficial tissue.

Next, a noncontact optical scanning system was used for human biological tissue measurements. First, the measurement of the forearm during an ischema test, and second, the measurement of the forehead while performing a working memory task are described. The measurement results showed that the developed scanning system

can be successfully used for human tissue measurement.

Finally, I discuss the future prospects of the noncontact NIRS system and promising application. The technique should be valuable, especially for the S-D distance optimization during the initial measurement of muscle tissue, the tissue thickness determination for a layered tissue structure, fast and high density deep tissue imager using an infrared CCD camera, and pressure-free long term measurement during sleep.

Contents

Chapter 1

Introduction

1.1. NIRS for biological tissue measurement

1.1.1. Principle of brain activity measurement with NIRS

Near-infrared spectroscopy (NIRS) has been used to measure brain functions noninvasively by monitoring cerebral blood changes (Brazy et al., 1985; Chance et al., 1993; Hoshi and Tamura, 1993; Jöbsis, 1977; Kato et al., 1993; Rea et al., 1985; Villringer et al., 1993; Wyatt et al., 1986). The NIRS system radiates weak visible or near-infrared light into the head and detects the transmitted light. This technique has been applied to an optical topography (OT) system that obtains images of brain function with multiple light sources and detectors (Koizumi et al., 1999; Maki et al., 1995; Yamashita et al., 1996). NIRS has also been applied for clinical use such as psychiatric diagnosis (Kameyama et al., 2006; Suto et al., 2004) or preoperative diagnosis in epilepsy treatment (Watanabe et al., 1998; Watanabe et al., 2000). Furthermore, it has been used for measuring oxygen saturation in skeletal muscle (Boushel and Piantadosi, 2000; Feng et al., 2001; Ferrari et al., 1997; van Beekvelt et al., 2001), in particular, during exercise (Perrey, 2008; Quaresima et al., 2003). In sports medicine, NIRS has been used to investigate the metabolism of skeletal muscle by measuring the oxygenation of hemoglobin (Hb) and myoglobin (Boushel and

Piantadosi, 2000; Ferrari et al., 1997; Quaresima et al., 2003).

OT systems have near-infrared laser diodes with two or more wavelengths, for example, 695 and 830 nm, and light detectors such as avalanche photodiodes or photomultiplier tubes. The wavelengths used in OT systems are usually between 690 and 900 nm (a range in which transmittance in biological tissue is high). This system measures hemoglobin change, in particular, the change in the product of Hb concentration (C, unit: mM = mmol/L) and effective optical path length (L, unit: mm) [$\Delta(C \times L)$ or more simply, ΔCL, unit: mM·mm], of biological tissue when continuous-wave (CW) light is used. Topographical images of brain activation can be obtained with multiple light sources and detectors placed in a two-dimensional (2D) lattice arrangement. Irradiation lights are intensity-modulated with a different frequency at each light source for the signal discrimination with lock-in detection. Fig. 1 shows the measurement principle with respect to photon propagation in human head tissue. Both oxygenated and deoxygenated Hb changes in the cerebral cortex lead to change in the intensity of detection light.

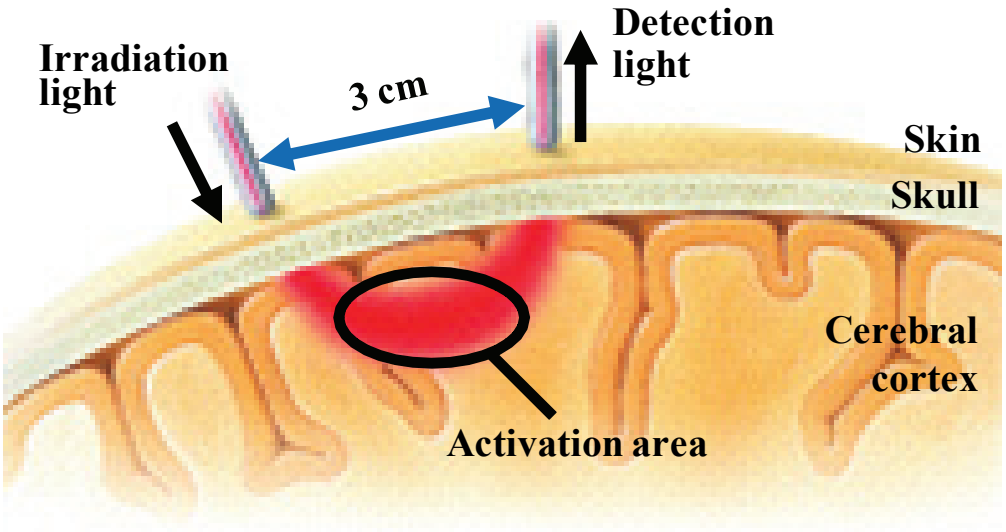

Fig. 1 Measurement principle with respect to photon propagation in human head tissue. The concentration change in blood of the cerebral cortex leads to change in the intensity of detection light.

In analysis, the two types of Hb change, oxygenated (oxy-) and deoxygenated (deoxy-), are calculated using two different absorption-coefficient spectra and the detected signals of two or more wavelengths according to the modified Beer–Lambert law (Maki et al., 1995; Delpy et al., 1988), which expresses the relationship between light attenuation and the concentration of the absorber in a light-scattering medium such as the living body. The original Beer–Lambert law can be applied only to a nonscattering medium. The detailed methodology including the formulas for Hb-change calculation is described in Appendix section.

Figure 2 shows extinction coefficients (ε) and absorption coefficients (a) of biological substances such as oxy- and deoxy-Hb (Matcher et al., 1995a), cytochrome oxidase (cyt-ox) (Matcher et al., 1995a), and water (Kou et al., 1993). In most studies using NIRS imaging, two types of hemoglobin are the objects being measured, while cytochrome oxidase and water content are assumed to be constant in a short measurement period.

1.1.2. Applications of NIRS

In the NIRS technique, the changes in two or more types of chromospheres, such as oxy- and deoxy-Hb, are usually calculated using absorbance change at two or more wavelengths (see Appendix section). In humans, the time series data of Hb change is very useful as a vital sign. Besides, the NIRS technique is valuable because blood volume change and tissue metabolism can be noninvasively monitored by small equipment. Examples of time series of changes in oxy-Hb, deoxy-Hb, and oxidized cytochrome oxidase obtained in the occipital area of the head during performance of a visual task are shown in Fig. 3 (adapted from Funane et al., 2009a).

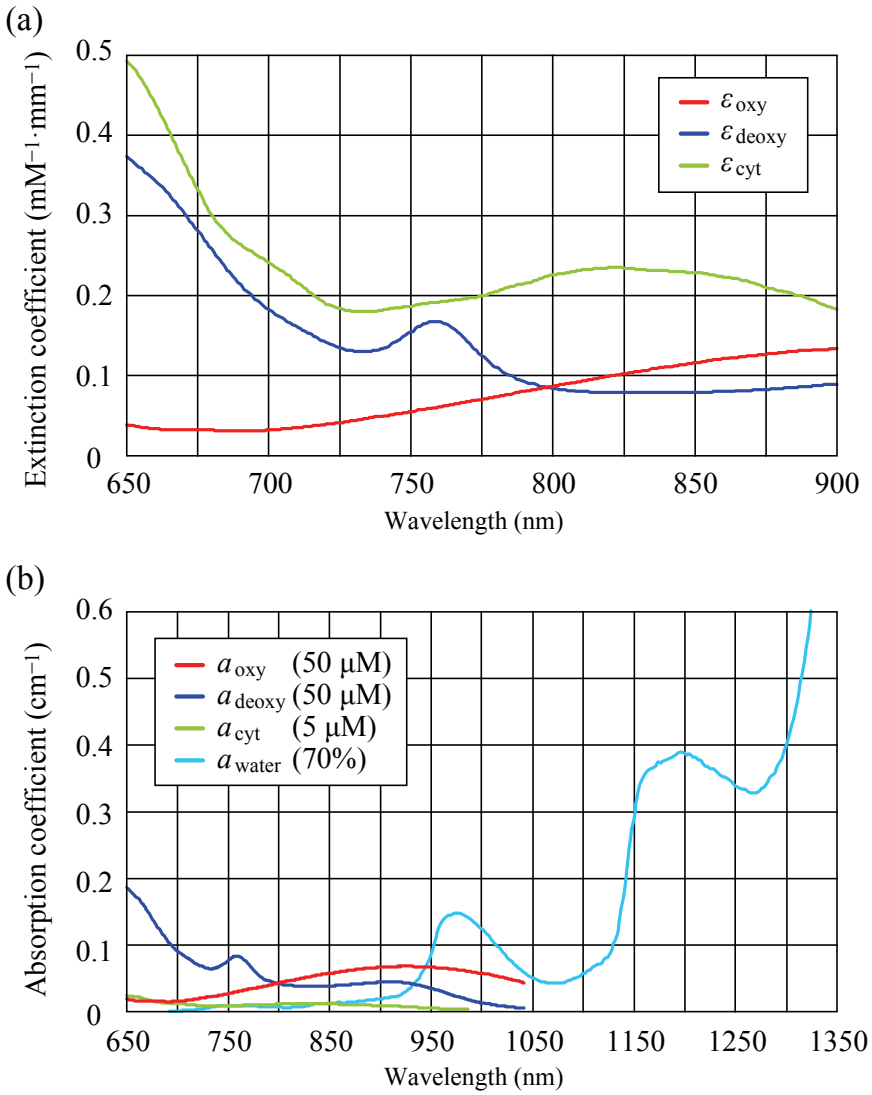

Fig. 2 (a) Extinction coefficient (ε) of oxy- and deoxy-Hb, and cytochrome oxidase (difference between oxy and deoxy ones); (b) absorption coefficient (a) of oxy- and deoxy-Hb, cytochrome oxidase (difference between oxy and deoxy ones), and water. These values are common-logarithm based.

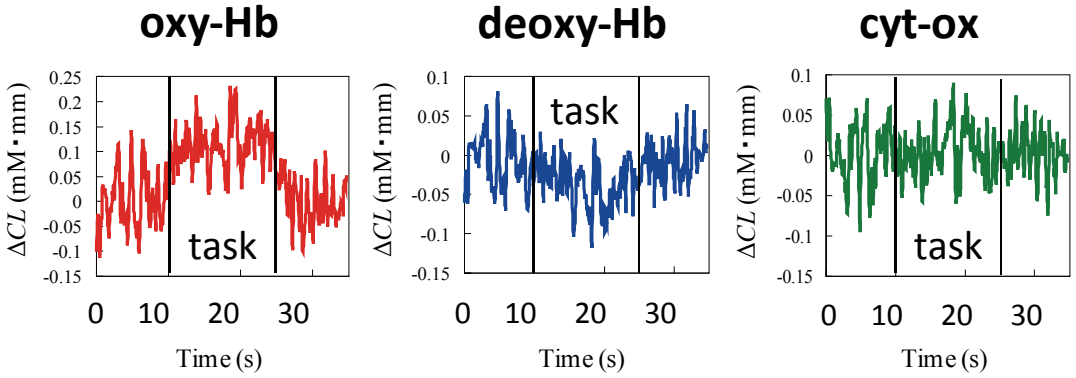

Fig. 3 Examples of time series of oxy-Hb, deoxy-Hb, and oxidized cytochrome oxidase (adapted from Funane et al., 2009a).

With these valuable parameters such as oxy- and deoxy-Hb change, NIRS or OT techniques have been widely used for research and clinical purposes (Koizumi et al., 1999; Maki et al., 1995; Obata et al., 2003; Obata et al., 2005; Sato et al., 1999; Taga et al., 2000; Watanabe et al., 1998) because of its noninvasiveness and few constraints (Ito et al., 2000; Kiguchi et al., 2007).

NIRS especially has advantages for the study of neurophysiology and development of language function in the brain because an NIRS system is very silent, providing a good setting for language studies, whereas functional magnetic resonance imaging (fMRI) systems make noise (Fuchino et al., 2006). Children and even infants can be tested while awake (Taga et al., 2000; Taga et al., 2003).

A recently developed wearable OT system (Atsumori et al., 2007; Atsumori et al., 2009; Atsumori et al., 2010; Kiguchi et al., 2012) is an effective tool for the study of brain activity in natural situations (Suda et al., 2010) such as face-to-face communications (Funane et al., 2011), walking (Atsumori et al., 2010), driving (Harada et al., 2007; Tomioka et al., 2009), and riding in moving vehicles (Krüger et al., 2012).

Application of NIRS is expanding as a brain-computer interface (BCI) (Utsugi et al., 2008), as the evaluation of cooperation (Funane et al., 2011; Cui et al, 2012), and for between-brain connectivity (Holper et al., 2012).

1.1.3. Limitations of NIRS and advantage of noncontact NIRS system

While NIRS has found a variety of applications and has many advantages over other neuroimaging modalities such as fMRI, PET, and EEG, it has several limitations (Koizumi et al., 2003; Hoshi, 2007; Hoshi, 2011), such as the quantification of NIRS data and influence of extracerebral tissue that has been recently reported by many researchers.

While these limitations should be addressed and investigated further, the limitation focused herein is the probe arrangement of NIRS, or the system-human

interface restriction by contact probes of the NIRS system. In an NIRS system, the light sources and detectors or light guides/fibers are usually attached to the skin so that the light detectors catch the light that propagates in the tissue rather than skin-reflected light or stray light. If the light source and detector are not in contact with the skin, the detector would certainly catch skin-reflected light or stray light as noise; however, the intensity of such noise is much higher than that of tissue-propagated light because the intensity of the tissue-propagated light is approximately 10^{-7}–10^{-9} times as high as that of the incident light (Okada et al., 1997). Consequently, the signal-to-noise ratio (SNR) deteriorates. Owing to this SNR reduction, the noncontact measurement of changes in cerebral blood volume is difficult. If the SNR reduction is avoided, a noncontact system would provide more degrees of freedom (with respect to both the system and subject) and enable new applications of brain activity measurement such as sleep research and other long-term brain monitoring.

If charge-coupled device (CCD) or complementary metal-oxide semiconductor (CMOS) imaging sensors are used for detectors, large amounts of data can be effectively and quickly obtained, and the effect of motions by the subject could be corrected in the image processing analysis.

1.2. Review of noncontact NIRS system

To overcome several limitations of NIRS as stated above, several researchers have recently reported noncontact optical measurement systems for the application of diffuse optical tomography (DOT) and brain activity measurement (Sase et al., 2006; Schulz et al., 2003; Turner et al., 2005; Wang et al., 2005; Konecky et al., 2008). These studies can be divided into two categories: 1) transmission DOT and 2) reflection DOT.

A transmission DOT system has an optical emitter and detector that are located on opposite sides, sandwiching the sample. A reflection DOT system has an optical emitter and detector that are located on the same side, against the sample. Some

literature on these two systems is described in the following section.

1.2.1. Transmission DOT

Schulz et al. (2003) reported a noncontact optical tomography system using CCD cameras for tomographic image reconstruction and three-dimensional (3D) surface extraction (Fig. 4). This noncontact transmission DOT system is only applicable to objects in a chamber such as *in vitro* biological tissue and small animals, and therefore, it is difficult to apply it to *in vivo* reflection-mode measurements such as for human brain activity and human muscle oxygenation.

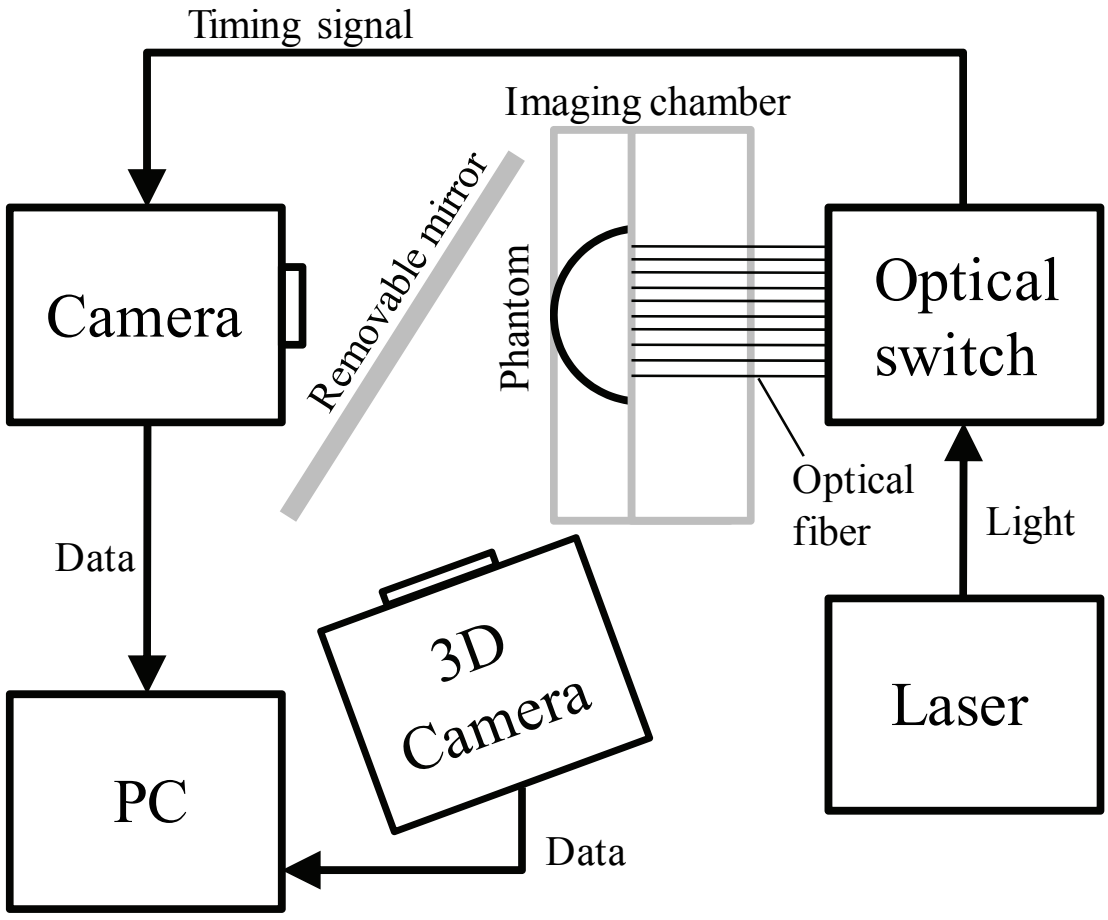

Fig. 4 Experimental setup of noncontact optical tomography system with transmission (projection) arrangement (adapted from Schulz et al., 2003). The 3D surface was captured with a 3D camera to be simultaneously recorded as well as reconstructed in a 3D tomographic image.

Turner et al. (2005) reported a transmission DOT system using early-arriving photons (Fig. 5). The developed scanning system and CCD image sensor allow the noncontact measurement of biological tissue and high spatial sampling of transmitted photons. Reconstruction algorithms that are similar to those used for x-ray computed tomography can be applied. Imaging is based on a complete-angle projection tomographic technique that utilizes early transmitted photons. The system is available only for optically thin samples, and therefore, cannot be used for breast or brain imaging because sufficient signal cannot be obtained when it penetrates through a thick light-absorbing tissue. It is a promising technique for future fluorescence molecular tomography studies of small animals.

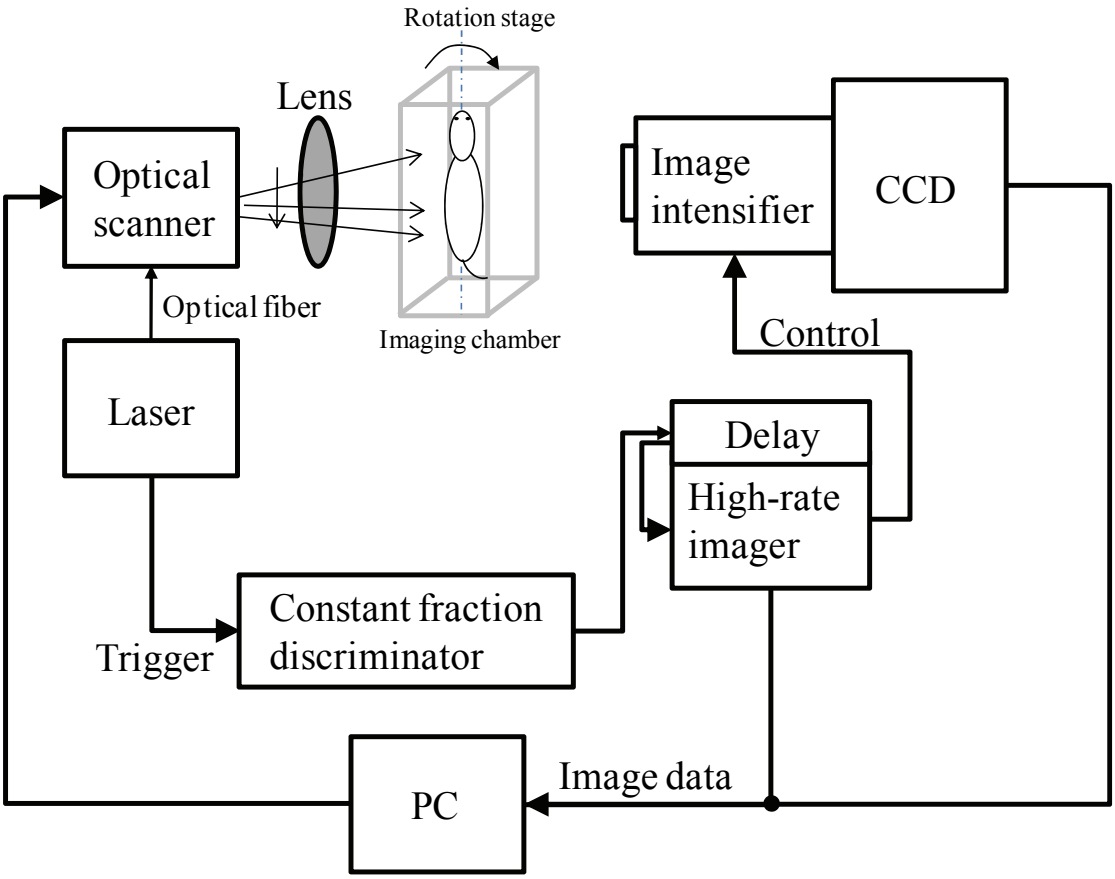

Fig. 5 Experimental setup of a time-resolved system using noncontact geometry (adapted from Turner et al., 2005).

Wang et al. (2005) reported an experimental demonstration of an analytical method for image reconstruction in optical diffusion tomography with large data sets (Fig. 6). A power meter is used to monitor the stability of the light source. The incident beam is scanned with an optical scanner. After propagating through the sample, the transmitted light passes through a band-pass interference filter and is imaged onto a front-illuminated, thermoelectrically cooled 16-bit CCD array. In their noncontact DOT system, data obtained at 10^8 source-detector pairs were employed to reconstruct the optical absorption of a highly scattering medium containing absorbing inhomogeneities. In an experiment, two absorbing black metal balls suspended in a liquid phantom (1% intralipid water) were successfully reconstructed by large data sets. The data were obtained by scanning the incident beam with galvanometer-controlled mirrors.

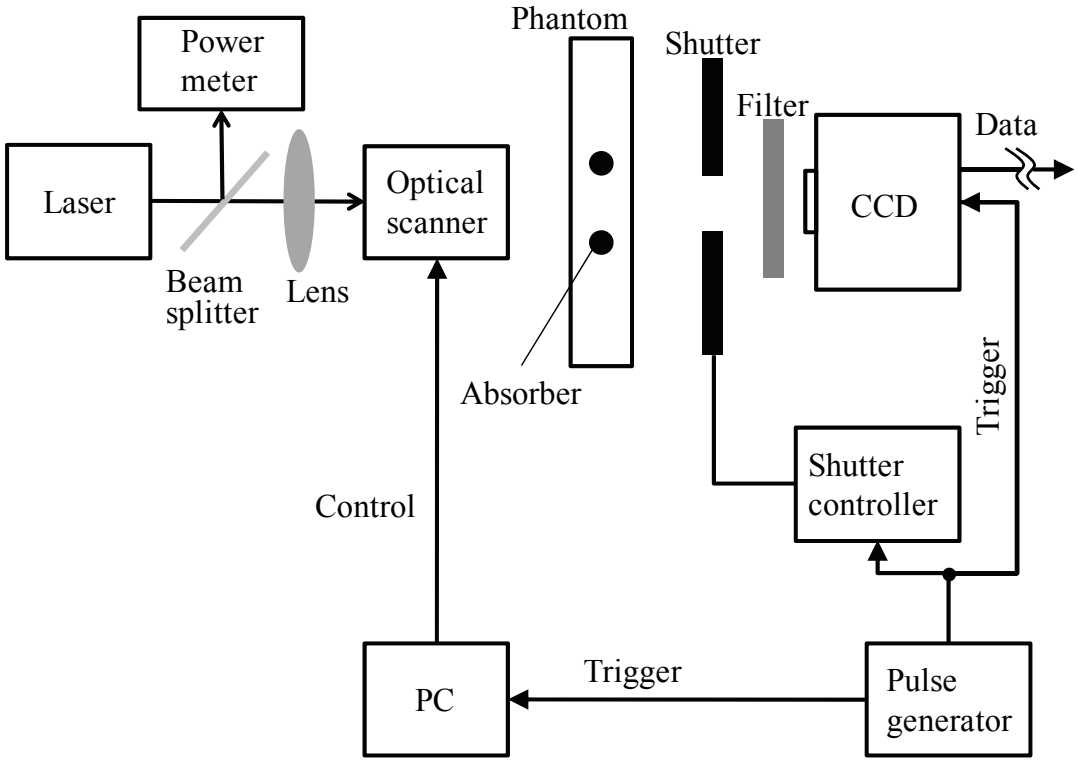

Fig. 6 Experimental setup of a noncontact optical tomography system (adapted from Wang et al., 2005).

1.2.2. Reflection DOT

Thompson et al. (2003) and Roy et al. (2005) reported a noncontact reflection-mode 2D and 3D, respectively, fluorescence imaging system using an intensified charge-coupled device (ICCD) camera with a 830-nm band-pass filter and a 785-nm band-rejection filter (Fig. 7). They used a tissue phantom with an indocyanine green (ICG) absorber that absorbs 780-nm light and emits 830-nm light (Mayer et al., 1999). In addition, they used optical filters to reject directly reflected light on the tissue surface and extracted the position of the fluorescent target.

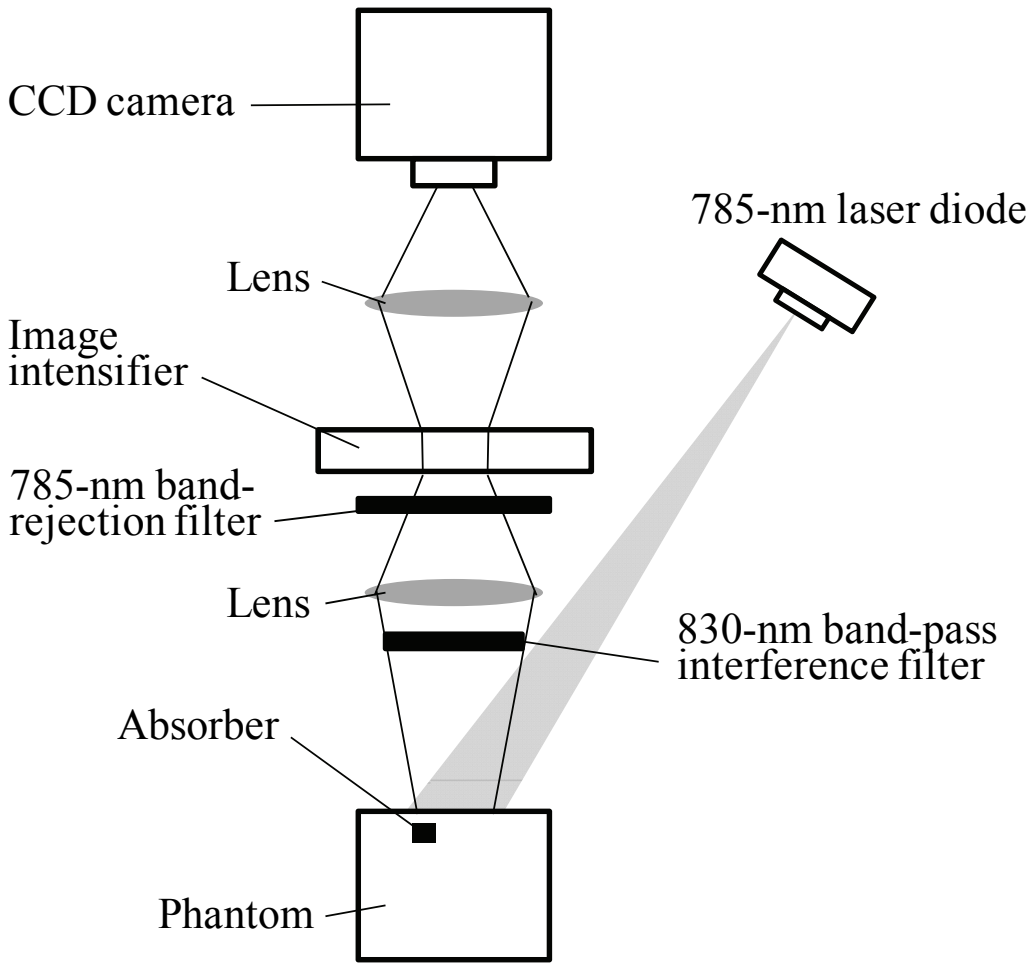

Fig. 7 Schematic of noncontact acquisition of fluorescence with ICCD camera by the illumination of plane light wave (adapted from Thompson et al., 2003; Roy et al., 2005).

Sase et al. (2006) developed a noncontact reflection-mode optical imaging system based on time-resolved imaging for applications of human brain activity measurement (Fig. 8). In their study, to cut backscattered light from the superficial area, the system uses a CCD camera equipped with an image intensifier having a time gate set to prevent photons that arrive earlier than specified from being captured.

A tissue-simulating phantom with a few small absorbers is measured by the system, and reconstructed absorbers were located on the same position as the true absorber position. In the analysis of reconstruction, the captured image without absorbers in the phantom was subtracted from that with absorbers.

Sawosz et al. (2010) reported an imaging system for brain oxygenation based on a time-gated, intensified CCD camera. It was demonstrated that the system reconstructed the position of the absorber in a phantom by on-off switching of nine light sources arranged in a circle on the phantom surface. Furthermore, *in vivo* human brain activity measurement, with two subjects, was performed at the position of C4 in accordance with the International 10-20 system (Jasper, 1958) during a finger-tapping task.

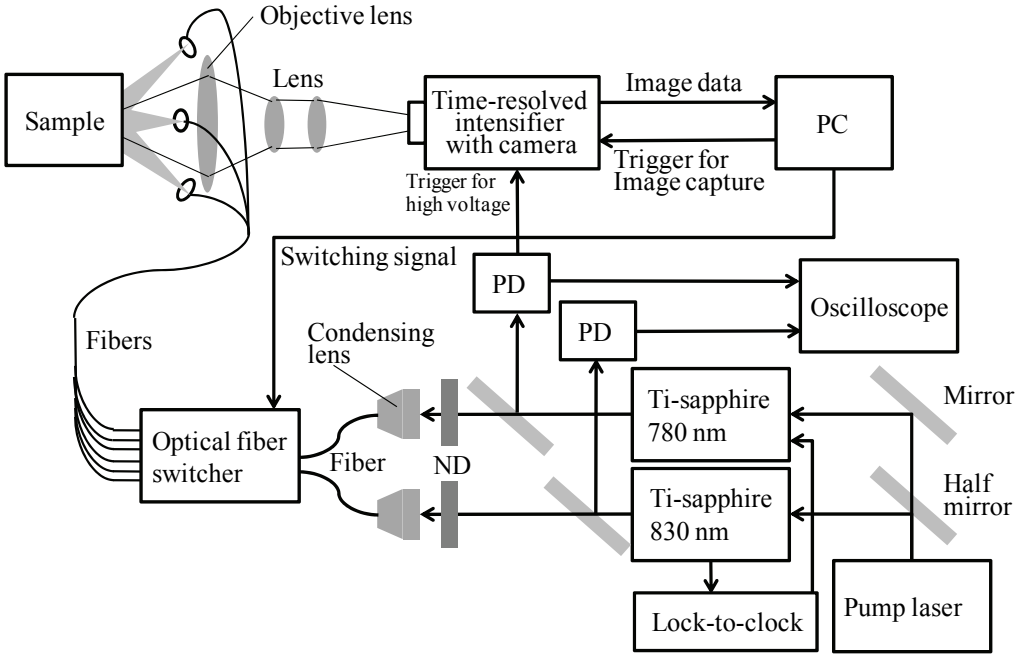

Fig. 8 Block diagram of noncontact system (adapted from Sase et al., 2006). ND denotes neutral density filter and PD denotes photodiode. Oscilloscope is used for monitoring PD signals.

Niwayama et al. (2006; 2007) reported that *in vivo* measurements of deep tissue absorption change in the human forearm were performed with a noncontact optical system (Fig. 9). They measured the muscle tissue of the human forearm during upper-arm occlusion with an ischemia test. The corrected oxygen consumption rate was obtained by considering the thickness of the fat layer.

Furthermore, Mazurenka et al. (2012) reported a noncontact system with null source-detector (S-D) distances based on time-domain NIRS utilizing a fast-gated single photon counting detector (Fig. 10). Radiation from a supercontinuum laser coupled to an acousto-optical tunable filter was used as a light source. To detect diffusively scattered photons as well as to suppress the directly reflected or minimally scattered photons, a polarization selective detection was implemented even though ~50% signal loss would occur. The detection system consists of a polarizer and a polarizing cube beam splitter. The polarizer serves to clean up the linear polarization of the incident light after an acousto-optical tunable filter. The polarizing cube beamsplitter is aligned to reflect the linearly polarized light coming from the acousto-optical tunable filter and the polarizer to a pair of image transfer lenses, focusing on the surface of the sample. Because light scattered by turbid media or biological tissues is randomly polarized, half of it, polarized perpendicularly to the incident light, passes through the polarizing cube beamsplitter and can be detected by a gated single-photon avalanche diode. Proof-of-principle tests were conducted, and the measured depth sensitivity and spatial resolution of this system were close to the values predicted by Monte Carlo simulations.

However, *in vivo* human brain activity measurement based on a noncontact NIRS system had not been reported until I reported (Funane et al., 2010) because there were several problems as follows: 1) the signal-to-noise ratio is low when reflection DOT without phosphor material is applied to human tissue measurement, 2) optical power should be low because of laser safety, and 3) the time-resolved spectroscopy measurement system is a rather large and expensive system that would be very difficult to miniaturize.

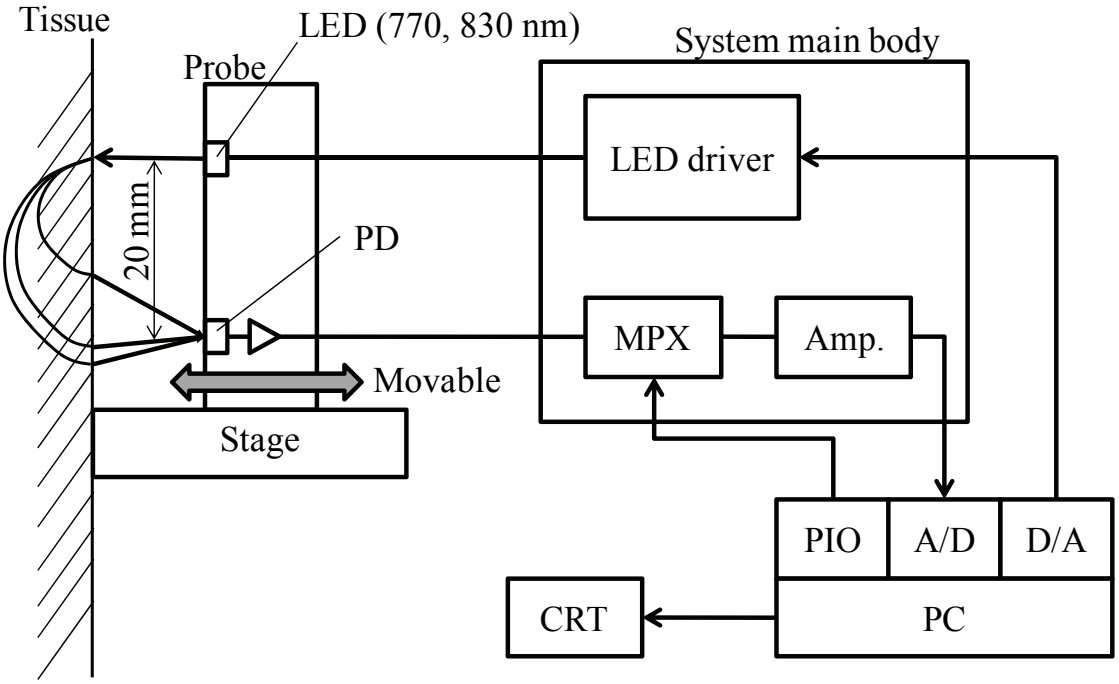

Fig. 9 Diagram of noncontact tissue oximeter. PD: photodiode, MPX: multiplexer, PIO: parallel input output (adapted from Niwayama et al, 2006; Niwayama et al., 2007).

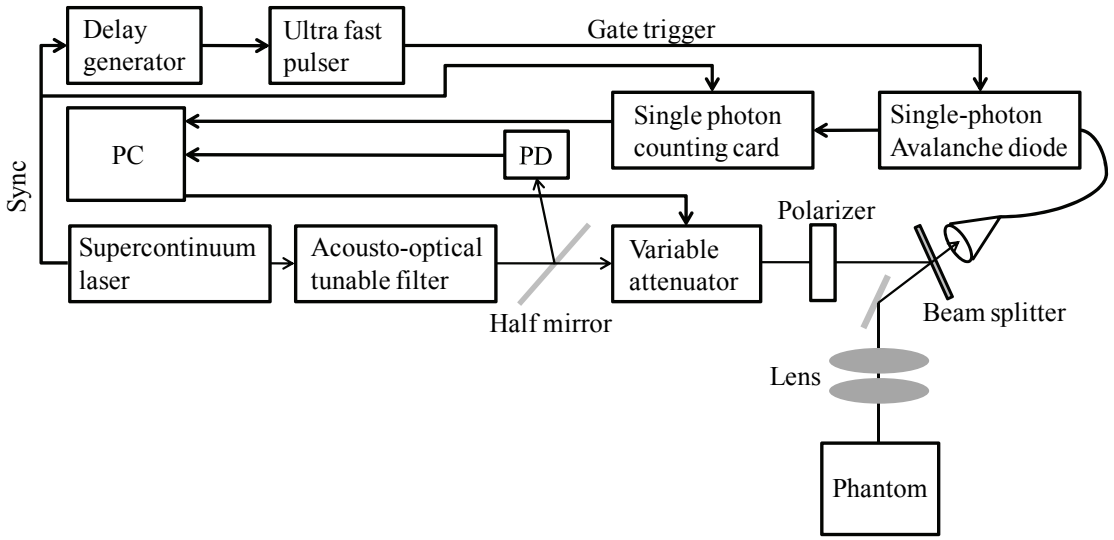

Fig. 10 Schematic of the noncontact brain scanning imaging system (adapted from Mazurenka et al., 2012).

1.3. Review of phantom development

1.3.1. Static phantom

The use of tissue-simulating objects to mimic the properties of human or animal tissues has been required for the development of biological imaging systems such as OT, DOT, sonography, X-ray CT, and MRI. These so-called “phantoms” are usually used for the following purposes (Pogue and Patterson, 2006):

1. Testing and evaluating system designs
2. Maximizing signal-to-noise ratio of obtained data by systems
3. Evaluating methodology of analysis and simulation
4. Comparing performance between systems

For evaluating NIRS instruments, many studies on phantom developments and phantom-based approaches have been reported (Delpy et al., 1988; Farrel et al., 1992; Firbank and Delpy, 1993; Patterson et al., 1989; Pogue and Patterson, 2006). To generate conventional phantoms for NIRS measurement, the photon-absorbing materials are made by mixing epoxy resin and hardener (Firbank et al., 1995). To control the absorption coefficient of the absorbers, an infrared dye is mixed into the absorber materials. To control the reduced scattering coefficient of the absorbers, titanium dioxide is mixed into the absorbers.

A static phantom (Firbank and Delpy, 1993; Firbank et al., 1995), however, cannot simulate time varying signals representing absorption changes that occur in actual biological tissues. Therefore, static phantoms cannot be used for evaluating time-domain analytical methods such as correlation analysis, principal component analysis, and independent component analysis. To materialize a more realistic phantom similar to biological tissue and provide evaluating time-domain methods, a dynamic phantom that can temporally change its optical properties is necessary.

1.3.2. Dynamic phantom

Kurth et al. (1995) reported a dynamic phantom that simulates neonatal brain for testing NIRS instruments. The brain model was made of a solid plastic structure containing a simulated vascular network perfused with blood equilibrated with O_2, N_2, and CO_2 in a closed circuit (Fig. 11). The potential utility of the dynamic phantom brain for testing NIRS instruments for accuracy and reliability was demonstrated.

Lohwasser and Soelkner (1999) reported a layered phantom for the human head consisting of a regular array of capillaries embedded in an epoxy matrix with tissue-like scattering and absorption properties for laser-Doppler flow measurements (Fig. 12). Capillaries were made by implanting nylon strings when the epoxy was malleable and removing them after the epoxy had solidified. To reproduce Doppler frequency spectra of biological tissue, diluted milk was pumped with compressed air. Constant fluid velocity was established with a height difference between the fluid levels in the supply and recirculation containers.

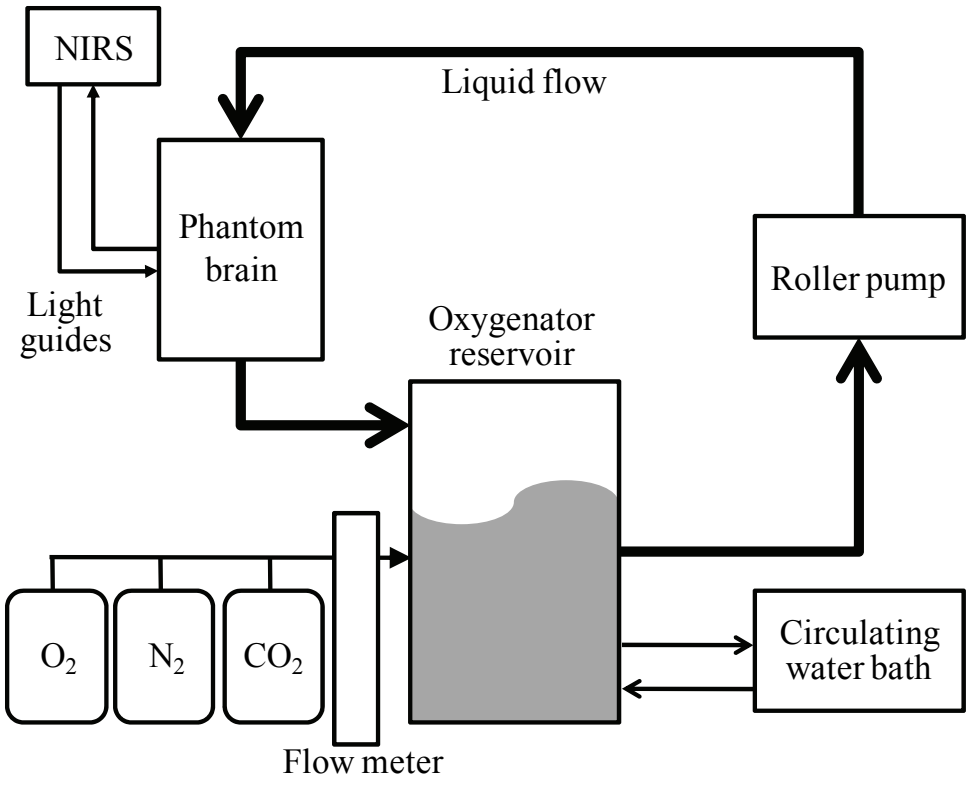

Fig. 11 Schematic diagram of blood-perfusion dynamic phantom (adapted from Kurth et al., 1995).

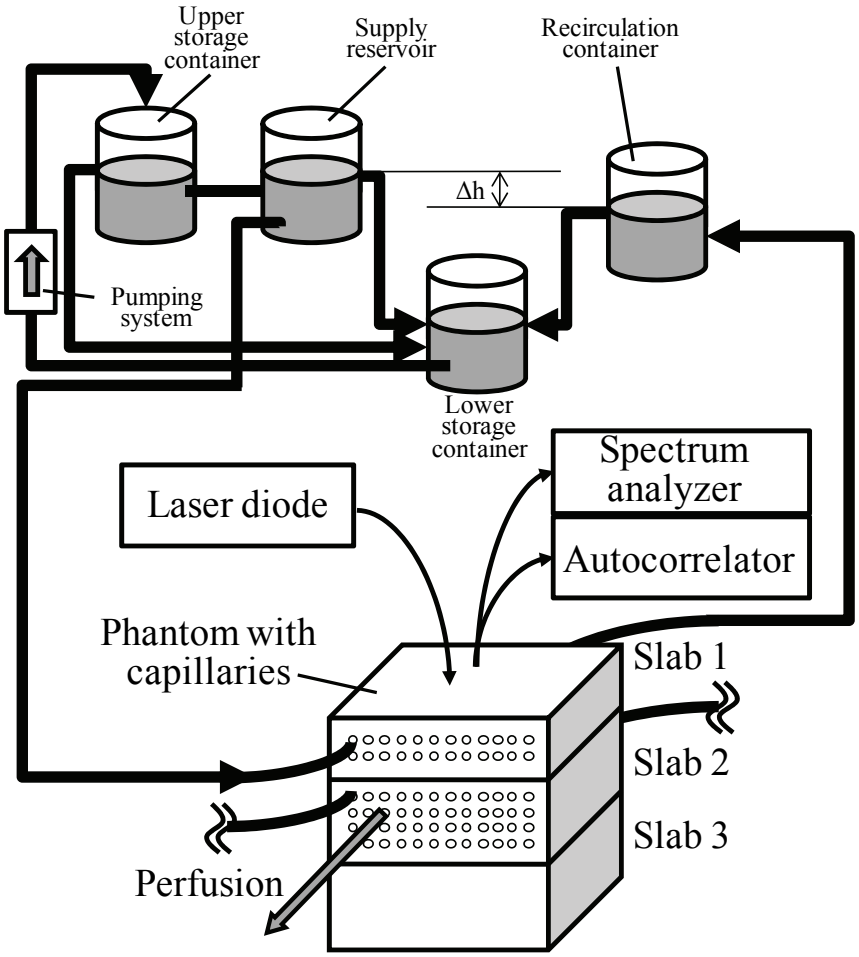

Fig. 12 Schematic of the liquid circuit for perfusing phantom for laser-Doppler flowmetry instruments (adapted from Lohwasser and Soelkner, 1999). Slab denotes a block consisting of a thick piece of tissue-simulating material. Slabs 1, 2, and 3 simulate each layer of the human head such as epidermis and dermis (Slab 1); skull, cerebrospinal fluid (CSF), and perfused cortex (Slabs 1 and 2); and nonperfused cortex (Slab 3).

Kim and Liu (2008) reported dynamic tumor vascular phantoms to investigate biphasic tumor oxygen dynamics induced by hyperoxic gas intervention. Driven by syringe pumps, ink solution flow was injected in plastic tubing embedded in a gelatin phantom. Several types of optical-density change (ΔOD) time series were generated by changing the position of ink flow and flow velocity (Fig. 13).

Koh et al. (2009) reported a dynamic phantom that consists of a modified liquid crystal display (LCD) sandwiched between two layers of tissue simulated by epoxy resin (Fig. 14). LCD enables flexible and rapid changes in attenuation across different regions of the phantom. The effect of size and shape of the attenuator region on

detected intensity was investigated. It can be used as a calibration tool for NIRS imaging systems.

A dynamic phantom that generates any waveform of absorption has not been realized because conventional dynamic phantoms are based on liquid perfusion or two-state control.

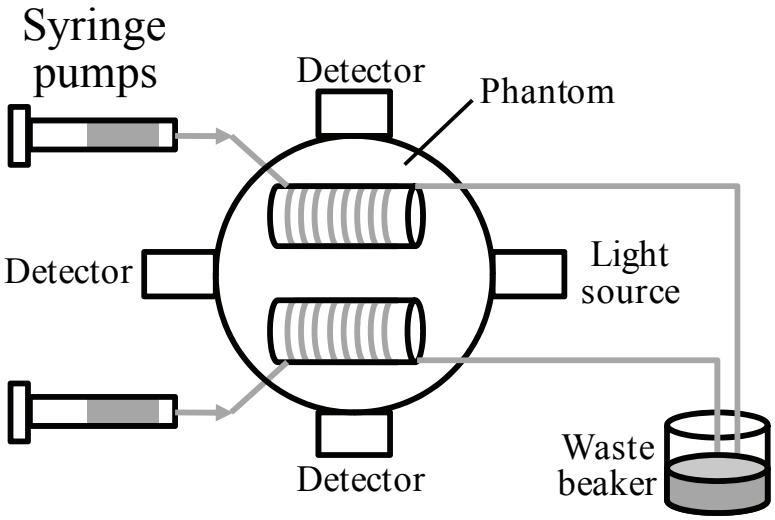

Fig. 13 Experimental setup for the tumor dynamic phantom study (adapted from Kim and Liu, 2008).

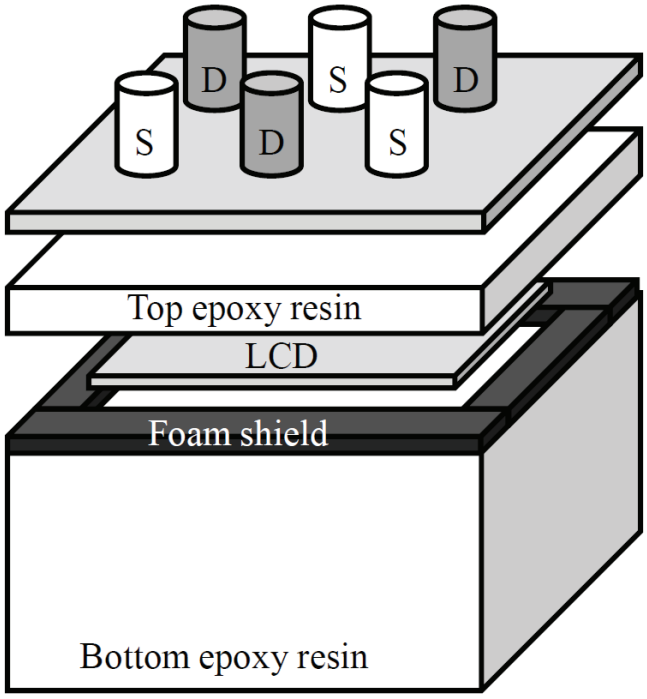

Fig. 14 Schematic of dynamic phantom with an LCD attenuator. S: source, D: detector (adapted from Koh et al., 2009).

1.4. Review of multi-distance NIRS measurement

1.4.1. Removal of surface-layer effects

NIRS is very sensitive to the superficial layers of the head because it is a back-reflection measurement. Therefore, the NIRS signal obtained during the performance of cognitive tasks is strongly contaminated by systemic interference of superficial origin. Several approaches based on a multi-distance method are proposed to overcome this problem. Figure 15 shows conventional cross-sectional photon paths in a multi-distance arrangement.

In the method used by Toronov et al. (2001) and Saager and Berger (2005), the deep-tissue signal is extracted by linearly fitting the short-distance channel to the long-distance channel by the least-mean-squares method and subtracting the fitted signal from the long-distance channel. The evaluation function E is defined as the square sum of the linear subtraction of the short-distance channel from the long-distance channel in the following equation.

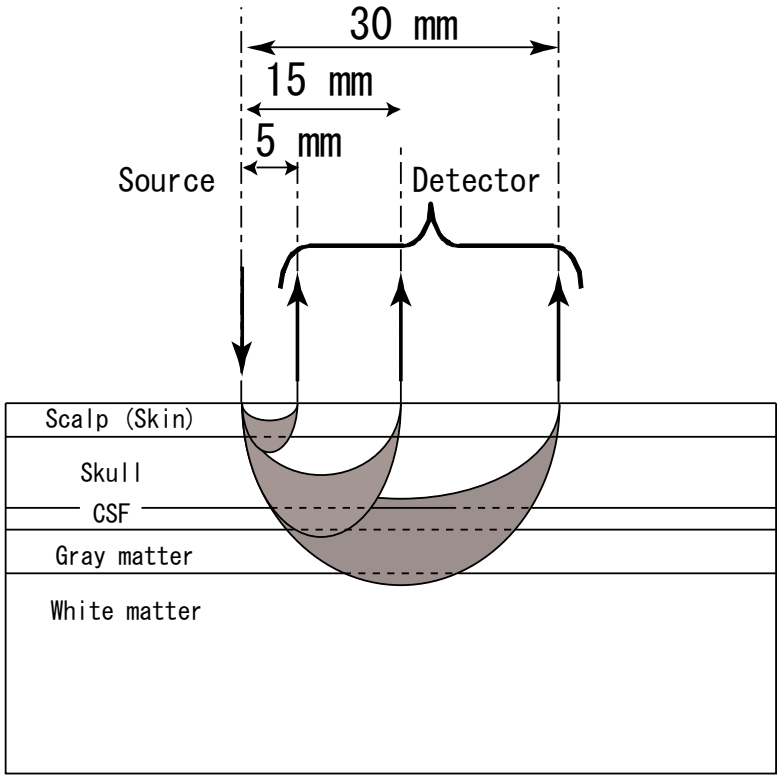

Fig. 15 Cross-sectional photon paths in a multi-distance arrangement.

$$E = \sum_{t} \left[\Delta OD_{\text{long}}(t) - (a\Delta OD_{\text{short}}(t) + b) \right]^2 , \quad (1)$$

where t denotes time, ΔOD_{short} denotes optical density change (ΔOD) at short S-D distance, ΔOD_{long} denotes ΔOD at long S-D distance, and a and b denote constant values. ΔOD is a dimensionless variable. After determining constant values (a and b) that minimize E, the fitted signal (ΔOD_{fit}) expressed as Eq.(2) is calculated.

$$\Delta OD_{\text{fit}} = a\Delta OD_{\text{short}} + b \quad (2)$$

By subtracting ΔOD_{fit} from ΔOD_{long}, the deep-tissue signal (ΔOD_{deep}) is obtained as:

$$\Delta OD_{\text{deep}} = \Delta OD_{\text{long}} - \Delta OD_{\text{fit}} \quad (3)$$

To calculate a and b on line, Zhang et al. (2007a; 2007b; 2009) reported adaptive filtering to reduce global interference such as systemic fluctuations in evoked brain activity detection induced by some cognitive tasks. In an adaptive filtering algorithm, using past M data points and filter coefficients w, the deep-tissue signal (ΔOD_{deep}) is determined by Eq. (4).

$$\Delta OD_{\text{deep}}(i) = \Delta OD_{\text{long}}(i) - \sum_{k=0}^{M} \left[w_{k,i} \Delta OD_{\text{short}}(i-k) \right]. \quad (4)$$

The filter coefficients are sequentially determined using ΔOD_{deep} in Eq. (5).

$$w_{k,i+1} = w_{k,i} + 2\mu \Delta OD_{\text{deep}}(i) \Delta OD_{\text{short}}(i-k) , \quad (5)$$

where the constant μ is the step size that controls the convergence rate of iterative calculations.

Gagnon et al. (2011) reported a Kalman filtering method for the removal of systemic interference in superficial layers. Moreover, it has been reported that the general linear model (GLM) method (Aqil et al., 2012), principal component analysis, or independent component analysis (Funane et al., 2011d) is effectively combined with multi-distance NIRS data.

1.4.2. Spatially resolved spectroscopy (SRS)

Multi-distance NIRS measurement has also been used for the measurement of absolute values of absorption coefficient based on the spatially resolved spectroscopy (SRS) technique (Matcher et al., 1995b; Suzuki et al., 1999).

In the SRS method, the slope of absorbance values ($\partial A/d\rho$) obtained at multiple detection points is calculated (source-detector separation: ρ) (Fig. 16). Using $\partial A/d\rho$, the product of absorption and reduced scattering coefficients of homogeneous scattering medium can be calculated by Eq. (6) based on photon diffusion theory (Patterson et al., 1989). If the reduced scattering coefficient is known, absolute absorption can be quantified.

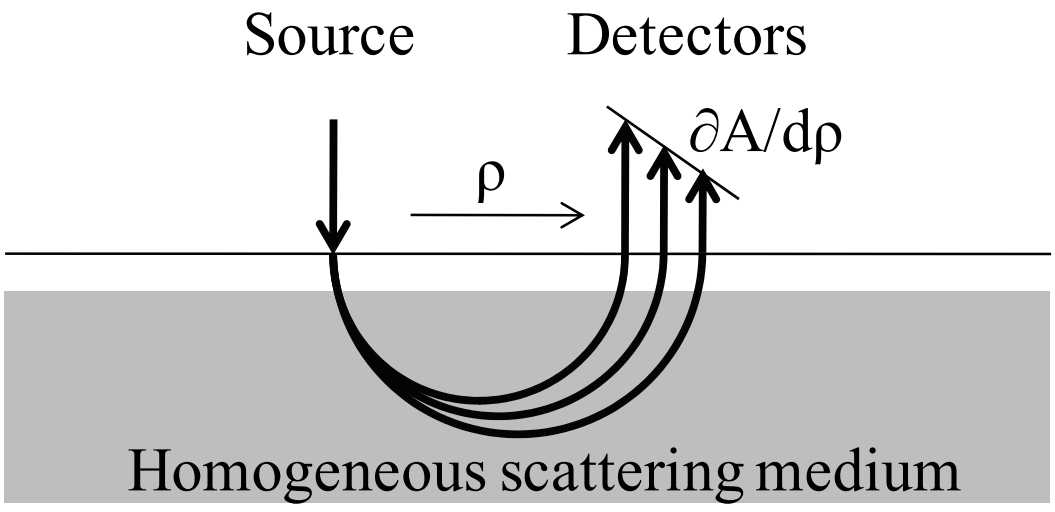

Fig. 16 Spatially resolved spectroscopy (adapted from Suzuki et al., 1999).

$$\frac{\partial A}{\partial \rho} = \frac{1}{\ln 10} \cdot \left(\sqrt{3\mu_a \mu'_s} + \frac{2}{\rho} \right), \tag{6}$$

where μ_a and μ'_s denote the absorption coefficient and reduced scattering coefficients of the tissue, respectively.

1.5. Purpose of this thesis

In this dissertation, I addressed a limitation of NIRS that contact probes are necessary and optimal source-detector (S-D) distance cannot be easily obtained. The purpose of this dissertation is the development of a noncontact NIRS system, validation of the proposed method, and demonstration for application to human muscle tissue and brain activity measurements.

As an introduction, Chapter 1 describes the principle, application, and challenges of the NIRS technique. Advantages of noncontact NIRS systems are also discussed in view of degrees of freedom with respect to both system and subject. In connection with this dissertation, literature on the noncontact NIRS technique, tissue-simulating phantoms, and methods using multiple S-D distance probes is reviewed.

Chapter 2 describes a noncontact measurement system. I propose a principle of noncontact NIRS system, and hemoglobin changes in a specific area of the prefrontal cortex are measured during a working memory task by simultaneously using this system and a conventional contact optical topography system. As a result, it was confirmed that the noncontact system measured human brain.

Chapter 3 describes an optical scanning system utilizing the noncontact NIRS technique. The system has a noncontact light emitter and detector with a galvano scanner and can measure the absorption change at variable S-D distances. A phantom with an inner absorber layer and a surface scattering layer whose thickness is changeable was measured by the system. The estimation of surface-layer thickness using optical density change at multiple S-D distances was demonstrated.

Chapter 4 describes the evaluation of the surface layer effect discrimination

method with multiple S-D distance measurements given by the optical scanning system. A dynamic phantom with two absorber layers that can be independently controlled was developed. Quantitative evaluation of a signal discrimination method was performed.

Chapter 5 describes application of the noncontact optical scanning system to human biological tissue measurement. The measurement of optical density change caused by blood volume change in the human forearm muscle during upper-arm occlusion and relief is described. The optical density change depending on S-D distance was obtained, which demonstrated the possibility that the optimal S-D distance for oxygenation monitoring on the human forearm can be determined by the scanning system. Furthermore, human brain activity was measured using the scanning system, and it was demonstrated that cerebral blood volume change was successfully extracted.

A summary of the work done and the conclusions drawn from it are given in Chapter 6. A description of further work is also presented.

Chapter 2

Noncontact measurement system

2.1. Principle of noncontact NIRS system

In a conventional reflection-mode noncontact NIRS system mentioned in Section 1.2.2, cerebral blood change signal is detected by using photon's time of flight (Fig. 17). Pulsed light source is used and time-resolved measurement is necessary, which mean the system should be large and expensive. Detection timing is time-gated and thus signal-to-noise ratio is theoretically low unless high peak power light source is used.

We proposed a new principle of a noncontact optical brain activity measurement system using phosphor placed on the scalp of the forehead of a subject, which requires less constraint, imposes no pressure on the skin, and is more comfortable for subjects being measured (Funane et al., 2010). The phosphor is excited only by tissue-propagated light (around 735 and 805 nm), and the emitted fluorescence (980 nm at peak) is detected by a light detector. The direct skin-reflected light and disturbance light are eliminated with optical filters placed on the phosphor and in front of the light detector (Fig. 18).

The intensity of fluorescence is proportional to that of the tissue-propagated light that excites the phosphor if there is no fluorescence photobleaching. The changes in

the product of hemoglobin (Hb) concentration (C) and effective optical path length (L), called "Hb change [$\Delta(C \times L)$]" here, can therefore be calculated by the changes in the intensity of fluorescence.

The use of phosphor solved the problem of SNR loss induced by disturbance light and made it possible to do the measurements with an arrangement of noncontact light sources and detectors. For practical use, it is important to optimize system parameters and clearly show that the system can detect the absorption changes in deep tissue, especially in the blood volume of the cerebral cortex, instead of detecting the absorption changes in superficial layer such as scalp.

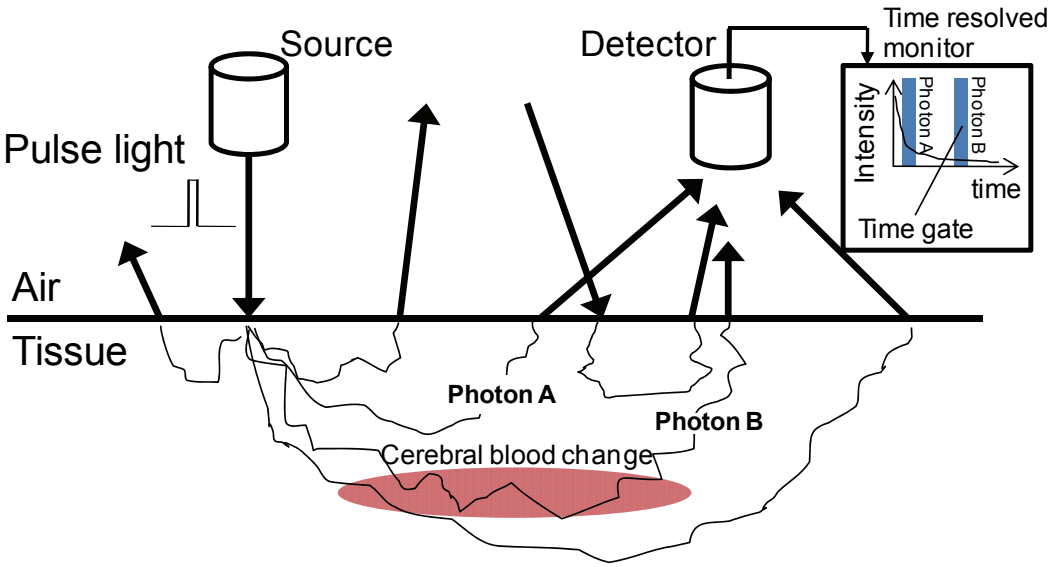

Fig. 17 Conventional principle of noncontact NIRS system. To cut backscattered light from the superficial area, the system incorporates a time gate set to prevent photons (Photon A) that arrive earlier than specified from being captured. Only photons (Photon B) that propagate in deep region where cerebral blood change occurs are detected.

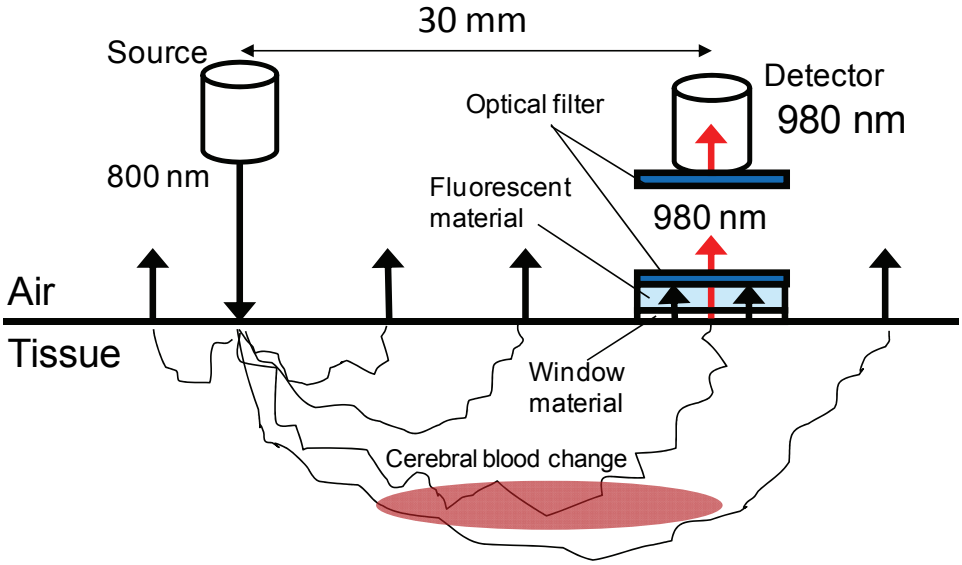

Fig. 18 Newly proposed principle of noncontact NIRS system. A fluorescent material (phosphor) is placed on the tissue surface and emits fluorescence. Excitation light or stray lights are cut by optical filters. The phosphor is excited only by the light that propagates in deep regions of tissue and detector detects only fluorescence.

In this work, first, the relationship between fluorescence lifetime and the amplitude of lock-in detection was investigated to determine the intensity-modulation frequency. Second, a phantom (the absorption of which was adjustable in deep areas) was measured to show that the system with phosphor and optical filters improved the SNR of the absorption change in the deep area. Third, to confirm that the noncontact system could detect the change in the cerebral blood rather than in the skin blood, the same area of the human prefrontal cortex was measured by simultaneously using this noncontact system and a conventional contact NIRS system during a spatial working memory task. Finally, based on the data obtained in the human brain measurement, the precision of the system was evaluated.

To achieve a noncontact optical system for the measurement of biological tissue, we used phosphor for wavelength conversion and optical filters to eliminate unnecessary wavelengths of light. The measurable parameters are oxy- and deoxy-Hb changes, which can be calculated with the change in absorbance of two wavelengths in a way similar to that with OT systems. However, the wavelengths should be

selected from the range where phosphor can be excited. Because the fluorescence emitted from the phosphor has the same spectrum regardless of excitation wavelength, the detected signals cannot be discriminated by the emission wavelength, but can be discriminated by the lock-in detection with intensity-modulated light sources at different frequencies.

2.1.1. Theoretical efficiency of phosphor measurement

When several losses caused by the requirements of our noncontact system are taken into account, optical power $P(\lambda)$ (unit: W) of detected fluorescence light at wavelength λ (unit: m) is theoretically expressed as the following equation:

$$P(\lambda) = P_0(\lambda) \cdot T_{tissue}(\lambda) \cdot A_r \cdot [T_{filter}(\lambda)]^2 \cdot \Omega \cdot k \cdot \int [S_{phosphor}(\lambda, x) \cdot S_{detector}(x)] dx, \qquad (7)$$

where $P_0(\lambda)$ (unit: W) denotes optical power of irradiation light at the tissue surface, $T_{tissue}(\lambda)$ (unit: $m^{-2}sr^{-1}$) denotes optical transmittance of tissue per unit detection area and per unit solid angle, $T_{filter}(\lambda)$ (dimensionless variable) denotes optical transmittance of optical filter, $S_{phosphor}(\lambda_{excitation}, \lambda_{emission})$ (dimensionless variable) denotes fluorescence emission spectral density at wavelength $\lambda_{emission}$ (unit: m) excited by light of wavelength $\lambda_{excitation}$ (unit: m), $S_{detector}(\lambda_{emission})$ (unit: m^{-1}) denotes sensitivity spectral of detector device at wavelength $\lambda_{emission}$, A_r (unit: m^2) denotes effective detection area, k denotes constant value, and Ω (unit: sr) denotes solid angle. $\int [S_{phosphor}(\lambda, x) \cdot S_{detector}(x)] dx$ (dimensionless) represents effective efficiency of the combination of phosphor and detector.

2.1.2. Phosphor selection

For the biological fluorescence imaging, a phosphor that is excited by and emits near-infrared light (around 700–1400 nm) that can easily penetrate in biological tissue ("biological optical window") because below 700 nm hemoglobin absorption dominates, while above 1400 nm water absorption dominates. Table 1 shows the comparison of phosphors that can be excited by near-infrared light.

Indocyanine green (ICG) is often used for biological fluorescence imaging because it is an FDA-approved tricarbocyanine dye that is used typically for ophthalmic angiography studies and hepatic function studies. It has also been used as an absorption contrast agent for biological imaging (Sevick-Muraca et al., 1997).

3,3'-diethylthiatricarbocyanine iodide (DTTCI) is similar to ICG in its excitation and emission spectra, but is different in their fluorescence lifetime. Fluorescent decays of ICG and DTTCI are well described by single-exponential decay functions (Mayer et al., 1999). ICG and DTTCI are thus used for fluorescence lifetime tomography (Godavarty et al., 2005).

$1.0Yb_2O_3$–$4.0Nd_2O_3$–$47.0Bi_2O_3$–$47.0B_2O_3$–$1.0Sb_2O_3$ has been reported as a near-infrared light source for optical coherence tomography (Fuchi et al., 2009).

$LiNdP_4O_{12}$ and $Li(Nd_{0.9}Yb_{0.1})P_4O_{12}$ have been reported as typical phosphors for use in marking (Shionoya and Yen, 1998). For example, phosphor mark in data card can be quickly read by a phosphor reading apparatus. These kinds of system were used for postage stamps.

We selected $Li(Nd_{0.9}Yb_{0.1})P_4O_{12}$ (Shionoya and Yen, 1998; Suzuki et al., 1978; Suzuki et al., 1979) as the phosphor used in our noncontact system because it has enough discrete two excitation-wavelength bands (735 and 805 nm) for Hb measurement and an emission-wavelength band (980 nm) where long-wavelength type Si APD has a high sensitivity. The phosphor is an inorganic material; therefore, fluorescence photobleaching does not generally occur with repeated excitation, so it may be suitable for a long-term measurement.

Table 1 Comparison of phosphors that are excited by near-infrared light

Phosphor	Excitation wavelength	Emission wavelength	Notes
ICG	780 nm	830 nm	lifetime: 0.57 ns (Mayer et al., 1999)
DTTCI	750 nm	830 nm	lifetime: 1.3 ns (Mayer et al., 1999)
$1.0Yb_2O_3$–$4.0Nd_2O_3$ –$47.0Bi_2O_3$–$47.0B_2O_3$ –$1.0Sb_2O_3$	584, 748 nm	1014 nm	Fuchi et al., 2009
$LiNdP_4O_{12}$	735, 805 nm	1047 nm	Shionoya and Yen, 1998
$Li(Nd_{0.9}Yb_{0.1})P_4O_{12}$	735, 805 nm	980, 1047 nm	lifetime: 0.93 ms (Funane et al., 2011a)

2.1.3. Excitation and emission spectrum of phosphor

The excitation spectrum and the emission spectra of the phosphor were measured using a spectrofluorometer (Nanolog, Horiba Jobin Yvon, Japan). The transmittance spectrum of an indium phosphide (InP) wafer was measured using a spectrometer (USB4000, Ocean Optics, U.S.A.) with a tungsten halogen light source (LS-1, Ocean Optics, U.S.A.).

The excitation spectrum of the phosphor is shown in Fig. 19 (a). The horizontal axis indicates the excitation wavelength, and the vertical axis indicates the emission intensity. There are roughly two peaks (around 730 and 800 nm) in the excitation

spectrum of this phosphor. Therefore, light-wavelength ranges of 730–760 and 790–820 nm are suitable for excitation of the phosphor. Light in these wavelength ranges has good transmittance in biological tissue (Boas et al., 2004).

Figure 19 (b) shows the emission spectra of a phosphor excited with 733- and 800-nm light, the transmittance spectrum of an InP wafer, and the sensitivity of an avalanche photodiode (APD) used in this study. The horizontal axis represents the wavelength, the left vertical axis represents emission intensity, and the two right vertical axes represent the sensitivity of the APD and the transmittance of InP. The peak wavelength of the emission spectrum of this phosphor is 980 nm. InP wafers used as the optical filters in this study were undoped and double-side polished and had a thickness of 0.5 mm, an orientation of 100 ± 0.5°, and a peak transmittance at about 975 nm. A silicon APD with peak sensitivity at about 940 nm (S8890-30, Hamamatsu Photonics, Japan) was used as a light detector.

In consideration of the excitation spectrum of the phosphor stated above, a widely available 808-nm laser diode (LD) was used for the phosphor excitation in the phantom measurement, and 735- and 805-nm light-emitting diodes (LEDs) were used in the human brain measurement.

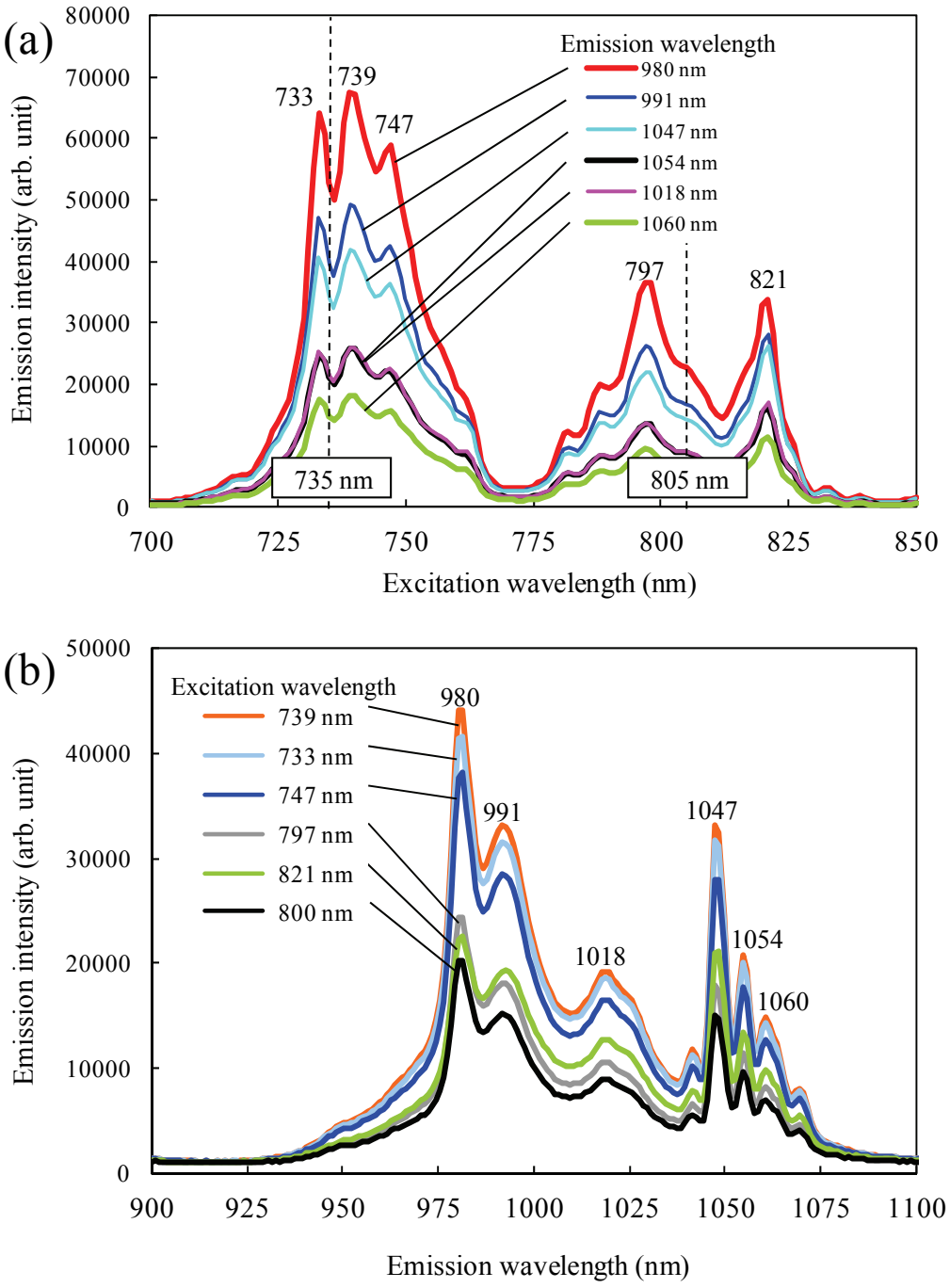

Fig. 19 (a) Excitation spectra and (b) emission spectra of the phosphor used in this study.

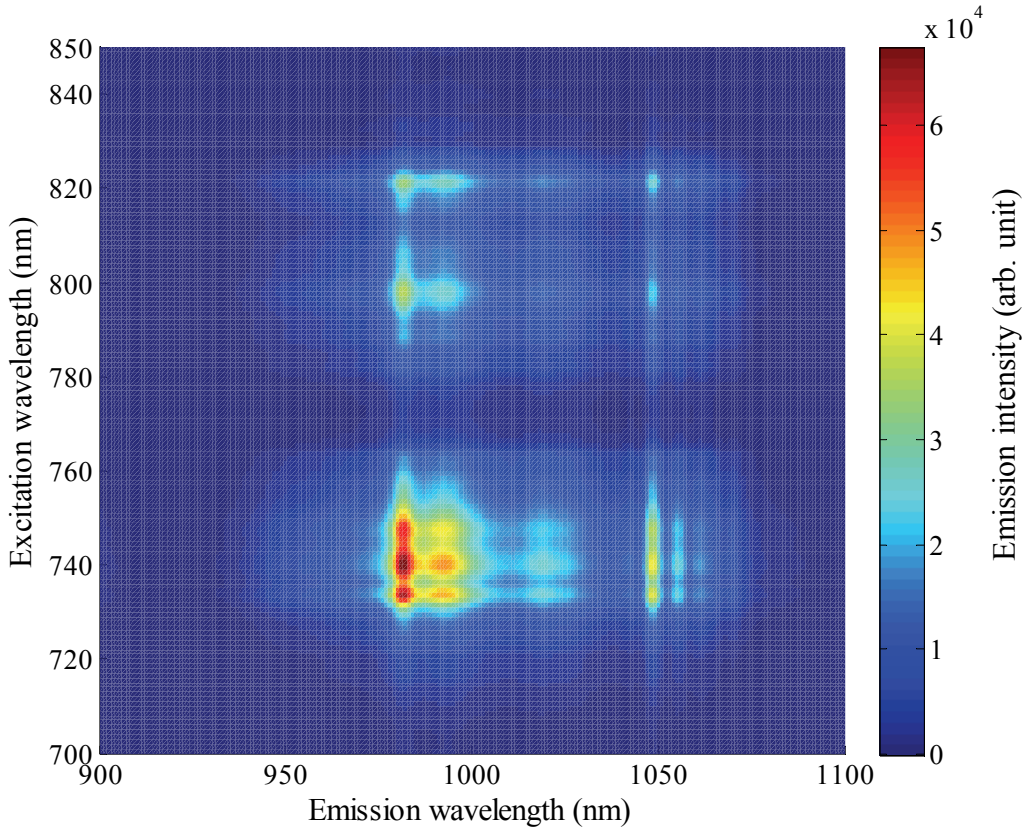

Fig. 20 Emission intensity map of phosphor [$Li(Nd_{0.9}Yb_{0.1})P_4O_{12}$] under the conditions of combination of excitation and emission wavelengths (nm)

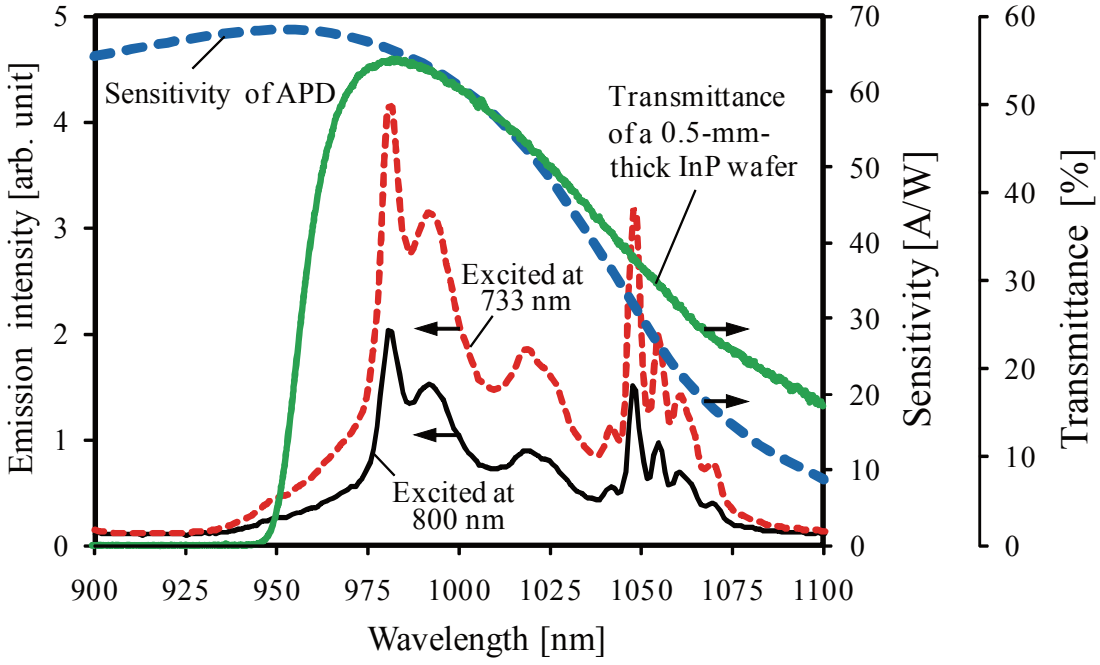

Fig. 21 Emission spectra of the phosphor [$Li(Nd_{0.9}Yb_{0.1})P_4O_{12}$] excited by 733- and 800-nm light beams, transmittance spectrum of a 0.5-mm-thick InP wafer used as optical filter, and sensitivity of APD (avalanche photodiode) used in this study.

2.1.4. Effect of fluorescence lifetime

The upper-limit frequency of intensity modulation for the lock-in detection is restricted by the fluorescence lifetime. To obtain the fluorescence lifetime of the phosphor used in this study, the time-resolved waveform of excitation light and fluorescence was measured by using an 810-nm LED driven with a 0.03-ms rectangular pulse as a reference. The experimental setup for measuring fluorescence lifetime of phosphor is shown in Fig. 22.

The fluorescence lifetime, namely, the time for the fluorescence amplitude to become 1/e times as large as the initial amplitude, was determined by the slope of the fluorescence-emission decay function on a log scale. It was assumed that the decay function can be modeled by a single-exponential decay. In an iterative calculation, the convolution of the detected excitation light pulse and a decay function with fluorescence lifetime was calculated, and the convolution and the measured fluorescence decay data were compared. A fluorescence lifetime of 0.933 ms was obtained by the least-mean-square method using data between 0.4 and 2 ms. Figure 23 plots the detected pulse waveforms of the excitation light and the fluorescence and the convolution of the excitation light and the decay function.

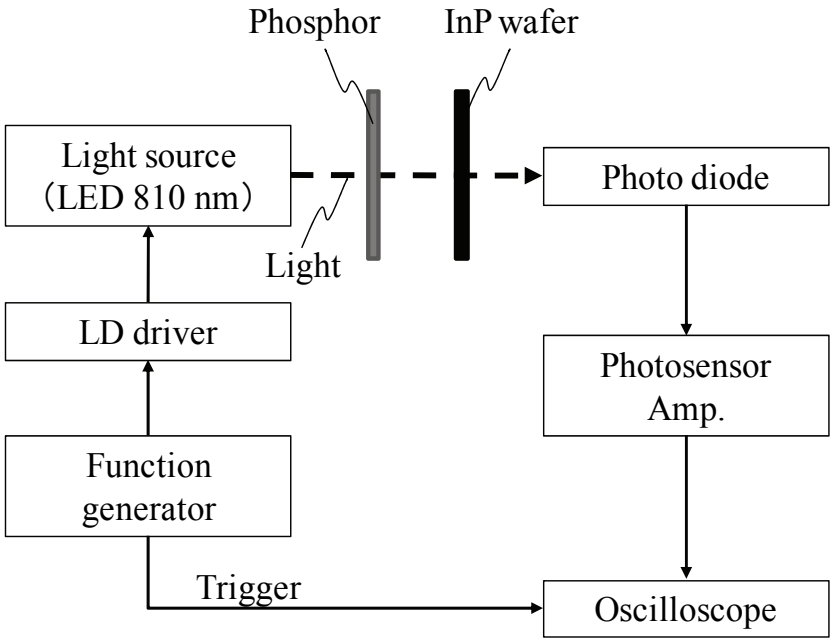

Fig. 22 Experimental setup for measuring fluorescence lifetime of phosphor.

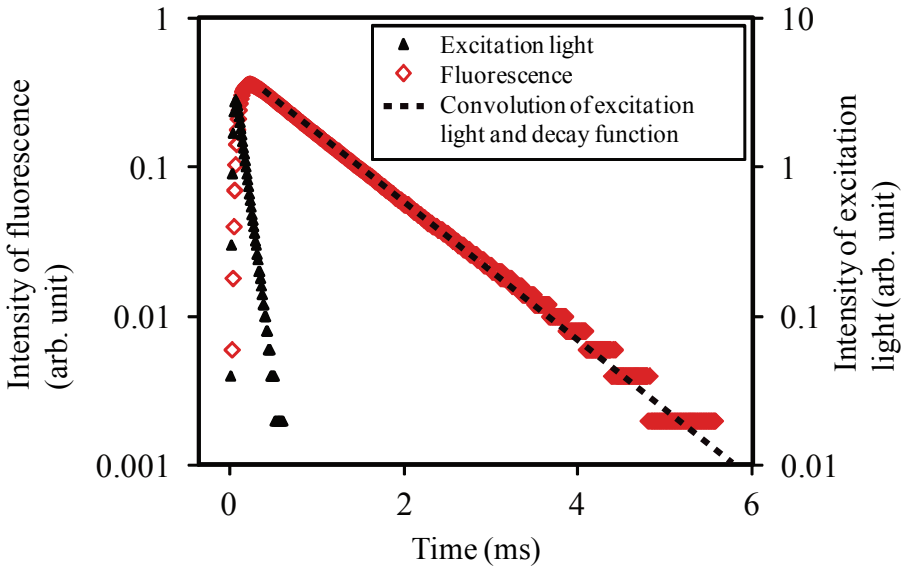

Fig. 23 Excitation light and fluorescence detected by a photodiode and convolution of the excitation light and a decay function modeled by a single-exponential decay with a time constant of 0.933 ms.

The deformed intensity-modulation fluorescence signal induced by the fluorescence lifetime induces the impaired amplitude of lock-in detection. To quantitatively investigate the effect of the fluorescence lifetime on the amplitude of lock-in detection, the following simulation and experiment were performed. In a simulation, the output of a lock-in amplifier (LA) was calculated in consideration of a fluorescence response function modeled by a single-exponential decay in the following way. First, the convolution of a square wave $f_1(t)$ and the response function was calculated, and then input signal $g(t)$ of the LA was obtained as

$$f_1(t) = \begin{cases} 1\,(0 \le t < T/2) \\ 0\,(T/2 \le t < T) \end{cases}, \tag{8}$$

$$g(t) = \int_0^t f_1(t-t')e^{-(t'/\tau)}dt', \tag{9}$$

where t stands for time, τ is the fluorescence lifetime (for which 0.933 ms was used), and T is the time for one cycle of intensity modulation. Second, the time average of the multiplication of a zero-mean normalized LA input signal $g(t)$ and a bipolar square-shaped reference signal $f_2(t)$ was calculated, and an output signal $h(t)$ of the

LA was obtained as

$$f_2(t) = \begin{cases} 1 \ (0 \le t < T/2) \\ -1 (T/2 \le t < T) \end{cases}, \tag{10}$$

$$h(t) = \frac{1}{T_c} \int_0^{T_c} f_2(t)[g(t) - \bar{g}]dt \ , \tag{11}$$

where $\bar{g}$ denotes the mean of $g(t)$ in a cycle, and T_c denotes the time constant of the LA.

In an experiment using an LA (model 5207, EG&G, U.S.A.), the intensity of the fluorescence emission due to 50%-duty square-wave LED light was measured while the frequency of intensity modulation was increased from 5 Hz to 10 kHz with a function generator (FG; 1930A, NF, Japan). The frequency response of the LA output obtained by the simulation and experiment is shown in Fig. 24. The solid line indicates the simulation results, and the plotted diamonds indicate the experimental results. The amplitudes of the output of the LA were normalized to 1 at 1 and 5 Hz for the simulation and experimental results, respectively. The simulation frequency response agreed well with the experimentally measured one.

Practically, the commercial power frequency and its harmonics should be avoided as a lock-in frequency. Furthermore, if the frequency is lower than 100 Hz, for example, a long averaging time would be necessary to stabilize the signal. The lock-in frequency should thus be determined according to the commercial power frequency and the necessary sampling speed for the target object (such as cerebral blood). For the phosphor used in this study, taking into consideration fluorescence lifetime and commercial power frequency, a frequency range of 200 to 300 Hz is suitable for intensity modulation. In this study, the modulation frequency of the 808-nm excitation light was set to 229 Hz for the phantom measurement, and the modulation frequencies of the 735- and 805-nm excitation light were set to 229 and 242 Hz, respectively, for the human brain activity measurement.

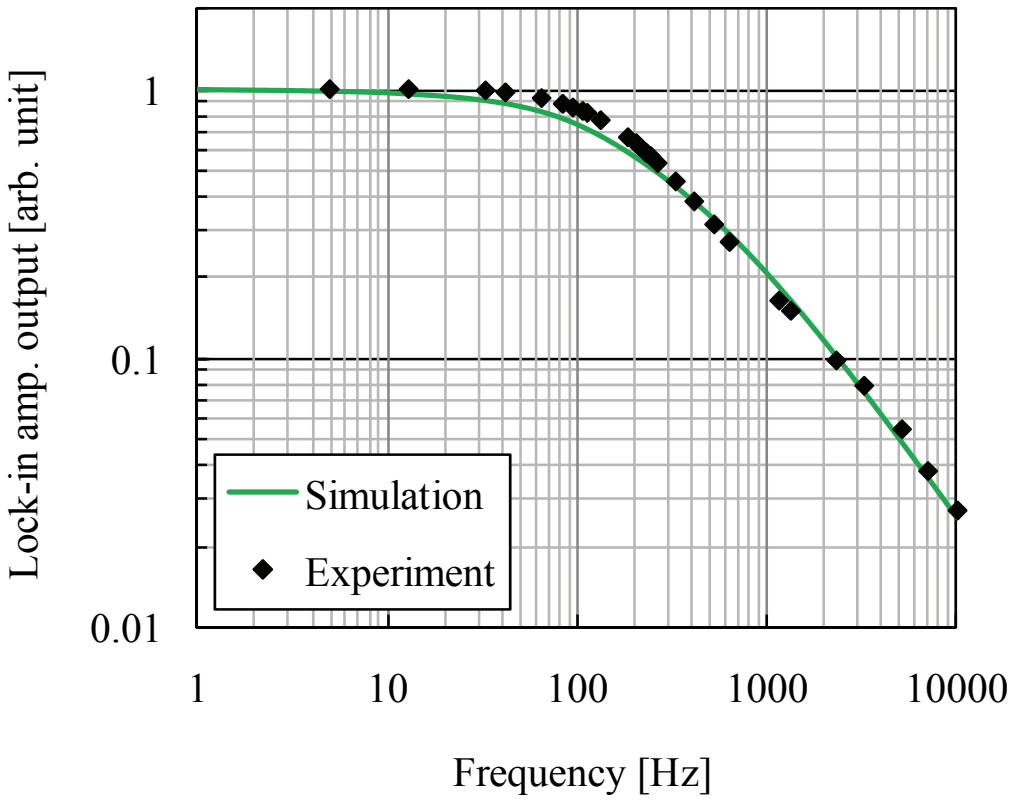

Fig. 24 Frequency response of lock-in amplifier output obtained in the simulation and experiment.

2.1.5. Effect of detection focal spot diameter

When our noncontact measurement system focuses the irradiation light on a specific position and detects light on another specific position, focal spot size of irradiation light and detection light on tissue surface is one of design parameters of the system. On the other hand, focal spot size may influence the effective path length of each layer of human head. Therefore, the effect of the diameter of irradiation and detection light on the effective path length of each layer of human head should be investigated to determine the requirement of focal spot size of irradiation and detection light and size of phosphor.

In order to investigate the effect of focal spot size on NIRS signals, the optical paths of photons propagated in tissue were simulated by a Monte Carlo method (Hiraoka et al., 1993; Okada et al., 1997; van der Zee and Delpy, 1987). Figure 25 shows human head model for Monte Carlo simulation. Table 2 shows optical

properties of human head tissue used in Monte Carlo simulation for light propagation in tissue. The assumed brain tissue model was taken from Fukui et al. (2003) and Okada and Delpy (2003a), and the inter-center distance of source and detector spot circle was set to 30 mm. When the diameter of irradiation focal spot was fixed to 1.5 mm and the diameter of detection focal spot was changed from 1.5 to 15 mm, partial effective path length of photons in scalp, gray matter and mean total effective path length were calculated by a Monte Carlo simulation. Based on the symmetric property of photon path, the calculated path lengths are equal to that when detection focal spot was fixed to 1.5 mm and irradiation focal spot was changed from 1.5 to 15 mm. In the simulation, the number of detected photons was 10000 and isotropic scattering (anisotropic parameter g = 0 for all tissues) was assumed.

Figure 26 shows photon paths calculated by Monte Carlo simulation applied for the assumed head layer model.

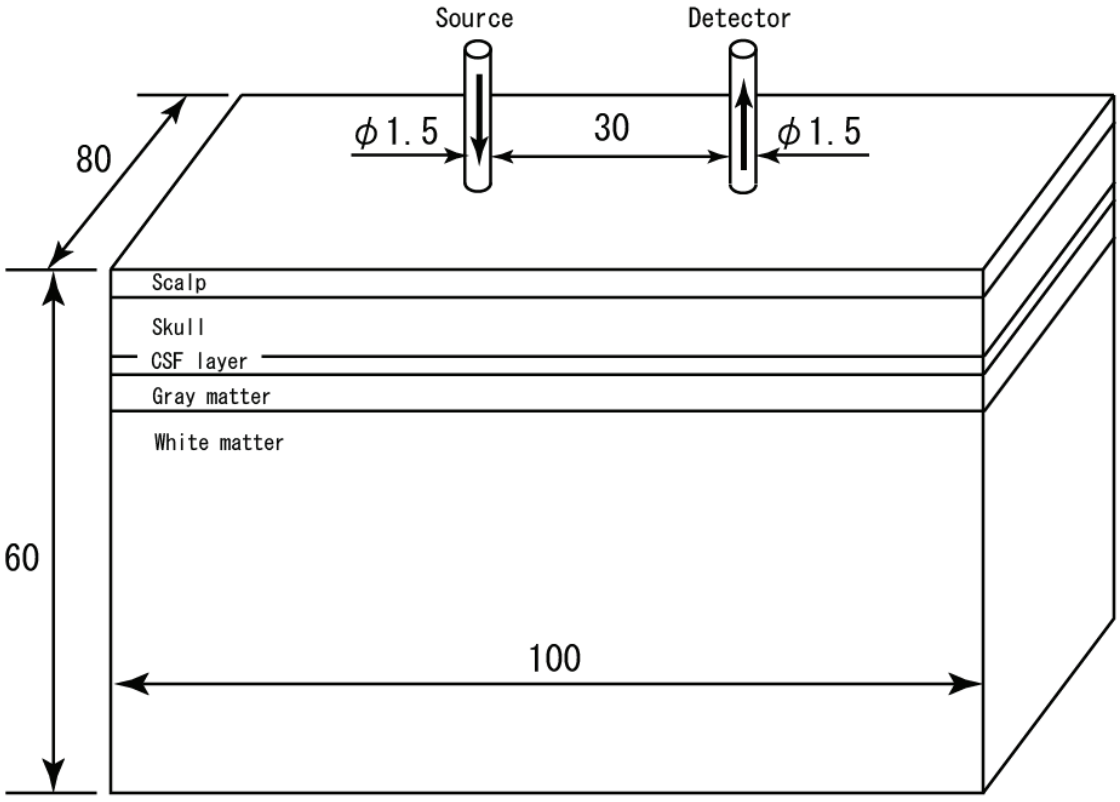

Fig. 25 Head model for Monte Carlo simulation (unit: mm).

Table 2 Optical properties of human head tissue used in Monte Carlo simulation for light propagation in tissue.

Tissue	Thickness (mm)	Reduced scattering coefficient (μ'_s) (mm^{-1})	Absorption coefficient (μ_a) (mm^{-1})
Scalp	3	1.9	0.018
Skull	7	1.6	0.016
CSF	2	0.25	0.004
Gray matter	4	2.2	0.036
White matter	44	9.1	0.014

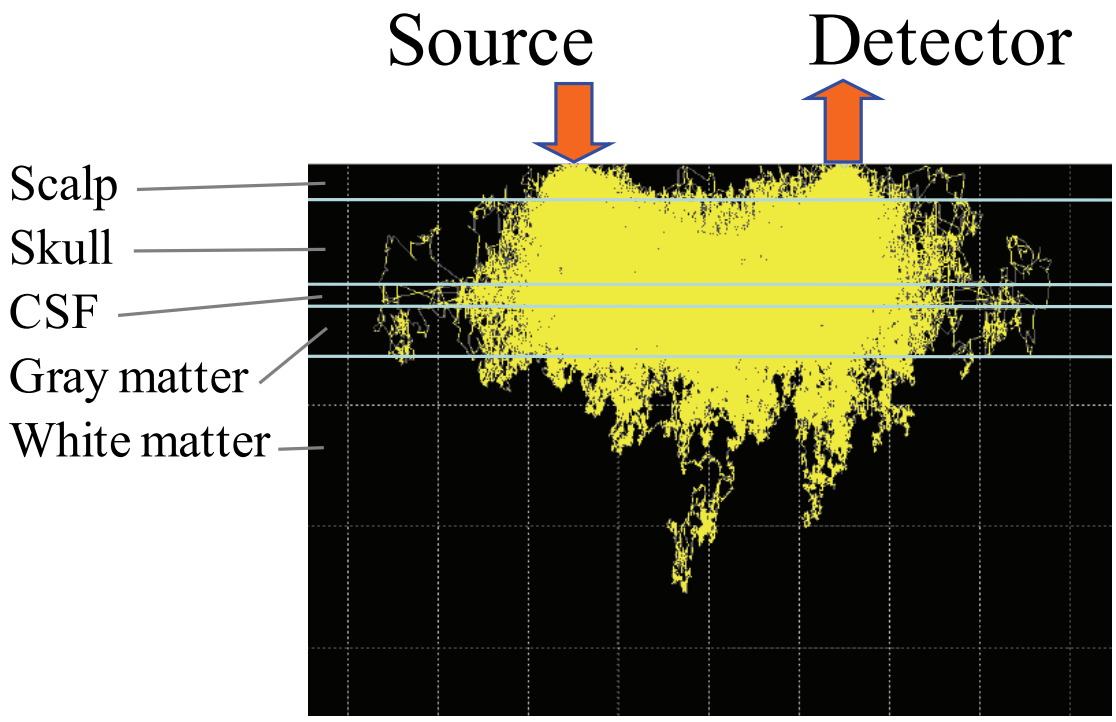

Fig. 26 Photon paths calculated by Monte Carlo simulation applied for assumed head model.

Figure 27 shows Monte Carlo simulation results: (a) optical path length in scalp and gray matter, (b) total optical path length, and (c) mean transmittance of photons, when the diameter of detector is changed. Black solid line is a fitting line for each

condition that is calculated using linear function for optical path length and exponential approximation for transmittance. The source-detector separation and irradiation focal spot diameter were set to 30, 15 mm, respectively. Numerical aperture (NA) was assumed to 1 at irradiation and detection point in the simulation.

Optical path length in scalp changes by only ± 2 mm even when the detection diameter changed from 1.5 to 15 mm (Fig. 27 (a)). Gray matter and total optical path length linearly decrease in accordance with increase of detection diameter (Fig. 27 (a)(b)). The photon transmittance is approximately proportional to the square of detection diameter (Fig. 27 (c)), which is a reasonable result.

When detection diameter increases from 1.5 to 15 mm, the photon transmittance becomes 100 times whereas gray matter optical path length becomes 0.83 times. The signal-to-noise ratio thus become larger when the detection diameter is larger.

2.1.6. Effect of phosphor use

The frequency of intensity modulation of the light sources is restricted in principle by the fluorescence lifetime. If phosphors with shorter fluorescence lifetime were used, a higher frequency of intensity modulation (which contains less noise) could be used. Otherwise, the CNR could become higher if a more efficient phosphor were used.

The effect of autofluorescence of biological tissues has been reported to be small in the near-infrared region (Amiot et al., 2008). When no phosphor was put on the scalp in an experiment, the fluorescent light obtained from the tissue was negligible. Therefore, the effects of autofluorescence from *in-vivo* tissues were ignored.

The SNR of Hb change depends on the combination of wavelengths used in NIRS (Funane et al., 2009b; Sato et al., 2004; Sato et al., 2006); therefore, it is a disadvantage that the available wavelength range for exciting phosphor is restricted by the characteristics of the phosphor used. To overcome this disadvantage, it is necessary to find or select other phosphor materials or quantum dots that have excitation wavelengths (between 690 and 900 nm) that make the SNR of Hb change higher.

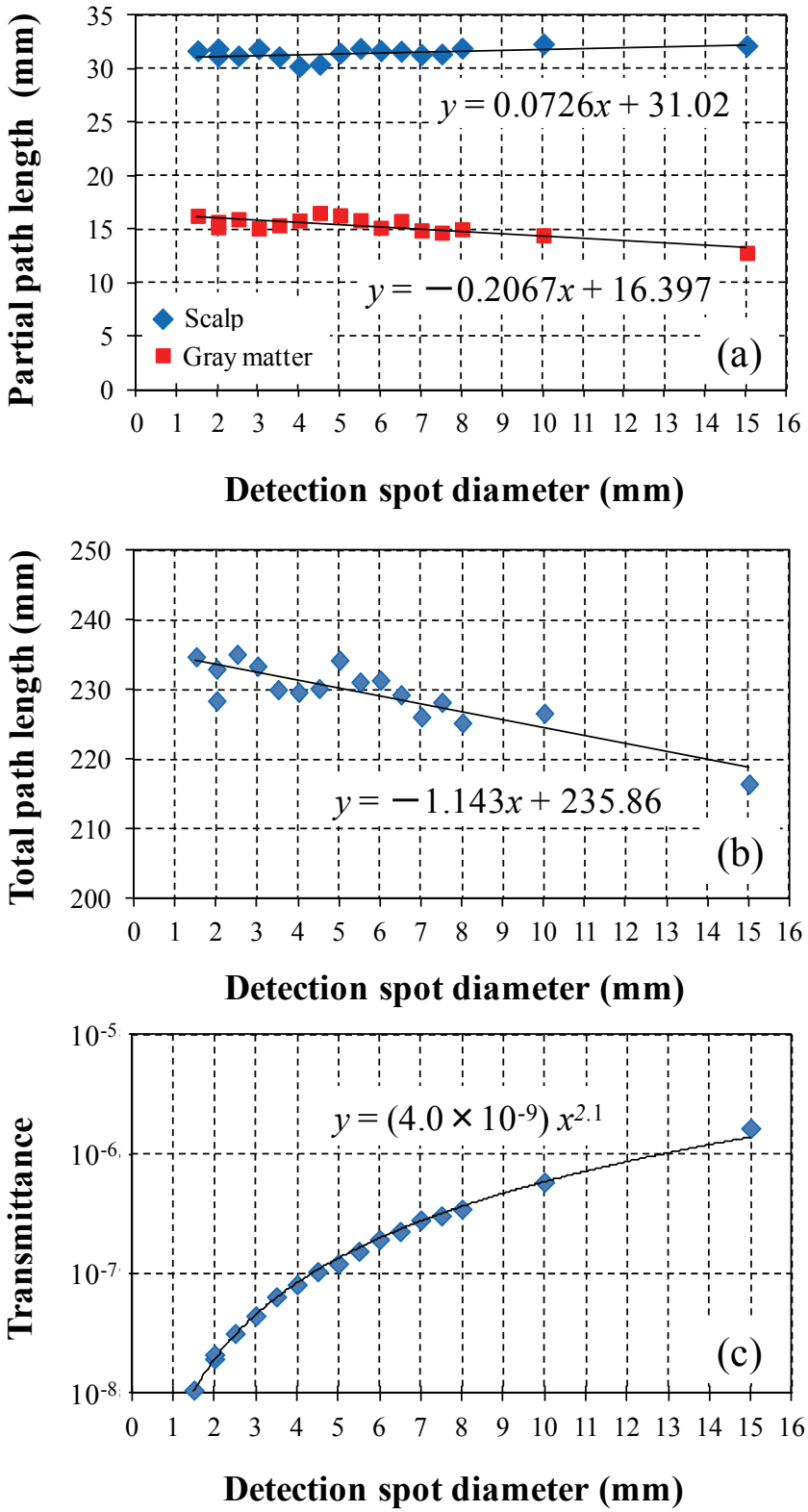

Fig. 27 Monte Carlo simulation results: (a) optical path length in scalp and gray matter, (b) total optical path length, and (c) mean transmittance of photons, when the diameter of detector is changed.

2.2. Phantom measurement

2.2.1. Methods of phantom measurement

To confirm whether the noncontact system detects the absorbance change in the internal tissue, we measured the sensitivity to changes in an absorber embedded in a phantom. Changes in the optical density under the following two conditions were measured using a noncontact optical configuration: Condition 1: with the phosphor and the optical filters that cut the excitation light. Condition 2: without the phosphor and the optical filters.

The experimental setup of the phantom measurement in Condition 1 is illustrated in Fig. 28. An 808-nm laser diode (LD; DL-8141-035, SANYO Electric, Japan) was used as a light source, and an APD (S8890-30, Hamamatsu Photonics, Japan) was used as a light detector. The power of irradiating light was 3 mW on the phantom surface. The LD was driven by an LD driver (ALP-7033CB, Asahi Data Systems, Japan). As a reference signal, a signal from a function generator was fed to the LD driver and an LA (model 5210, EG&G, U.S.A.). The modulation frequency of excitation light was set by an FG (1930A, NF, Japan). The fluorescence signal was detected with the APD and then detected with the LA, the time constant of which was set to 1 s. The analog output of the LA was converted into a digital signal by an analog-digital converter and stored on a personal computer (PC).

The base material of the phantom was epoxy resin containing titanium oxide as a light-scattering substance and greenish-brown dye as a light-absorbing substance. The absorption coefficient μ_a and transport scattering coefficient μ'_s were designed to be 0.033 and 1.0 mm^{-1}, respectively, at 800 nm. The black or white polyoxymethylene (POM) resin used to make an optical absorption contrast had a cylinder shape (30 mm long and 10 mm in diameter) and was embedded (10–40 mm deep) in the phantom in the center between the irradiation and detection positions. The distance between the irradiation and detection positions was 30 mm.

Biconvex lenses used to focus the excitation light and fluorescence light had 25-mm diameters and 25-mm focal lengths and were fixed in lightproof tubes that

were coaxially placed in parallel between each optical device (LD or APD) and the skin. The phosphor was fixed on the phantom using a cell (consisting of a 0.4-mm-thick 18 × 18-mm heavy paper frame with an 8 × 9-mm square hole) and clear adhesive tape. Both surfaces of the cell were covered with clear tape, and a small amount of phosphor was enclosed in the cell so that the thickness of the phosphor was evenly distributed. After that, when the cell was fixed on the phantom surface, the upper surface of the cell was covered with an InP wafer, which was fixed with clear tape onto the cell and the skin (Fig. 29).

Before the experiment was performed, it was confirmed that the excitation light and fluorescence were able to transmit through the clear tape. Two InP wafers were used in this system: one was placed on the phosphor to prevent excitation of the phosphor by stray light, and the other was placed in front of the APD to cut backscattered excitation or stray light.

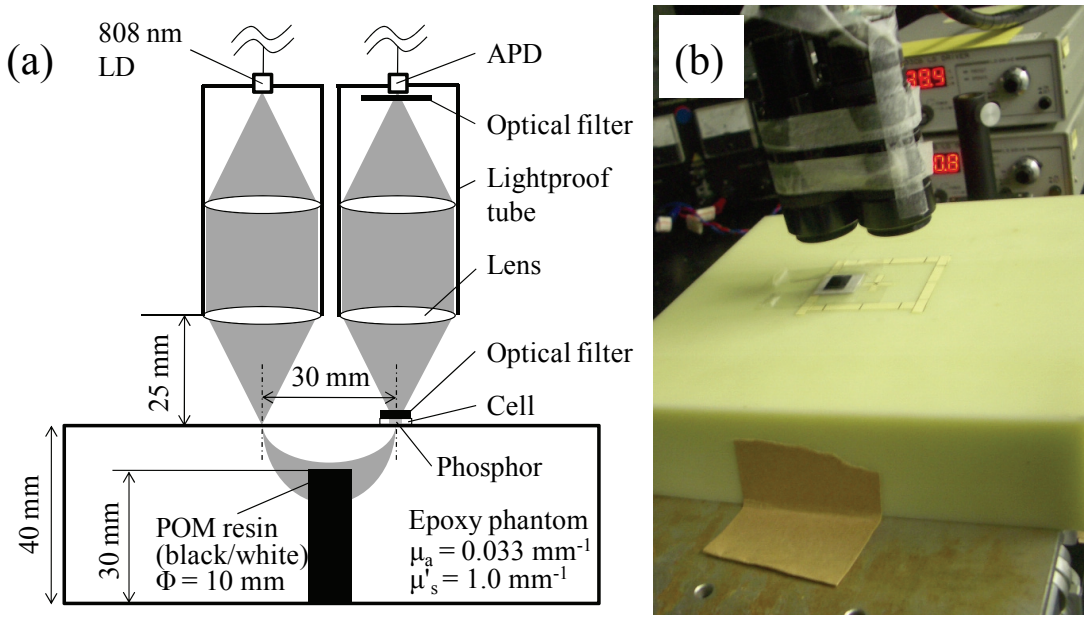

Fig. 28 (a) Experimental setup of phantom measurement with phosphor and optical filters. (b) Photograph of the setup. LD stands for laser diode, APD stands for avalanche photodiode, and POM stands for polyoxymethylene. The change in detected power was used to calculate ΔOD when the embedded object was changed from a white POM resin to a black one.

In the measurement sequence, first, a black POM resin was inserted into the phantom, and 10-s mean intensity of the detected light (I_{black}) was measured. Second, a white POM resin was inserted into the phantom, replacing a black POM resin, and 10-s mean intensity of the detected light (I_{white}) was measured. This sequence was repeated five times. No refractive-index matching liquid was used. Using each I_{black} and I_{white} pair, the change in optical density (ΔOD) was calculated according to Eq. (12) based on the modified Beer-Lambert law (Delpy et al., 1988; Maki et al., 1995) when the white POM resin was assumed to be the base absorber. Then we calculated mean and standard deviations of the five results of ΔOD:

$$\Delta OD = -\ln(I_{black} / I_{white}) = \Delta\mu_a L_{eff}, \tag{12}$$

where I_{black} and I_{white} indicate the detected optical power as the black and white POM resins, respectively, were inserted into the phantom, and $\Delta\mu_a$ is the change in the absorption coefficient of POM resin. L_{eff} stands for the mean effective optical path length in POM resin that is usually the function of the distance (ρ) between the irradiating and detection positions if the ρ is assumed to be unique. In the two conditions (with or without phosphor and optical filters) stated above, $\Delta\mu_a$ did not change because the same black and white POM resins were used for both conditions, therefore ΔOD can be changed by the change in L_{eff}.

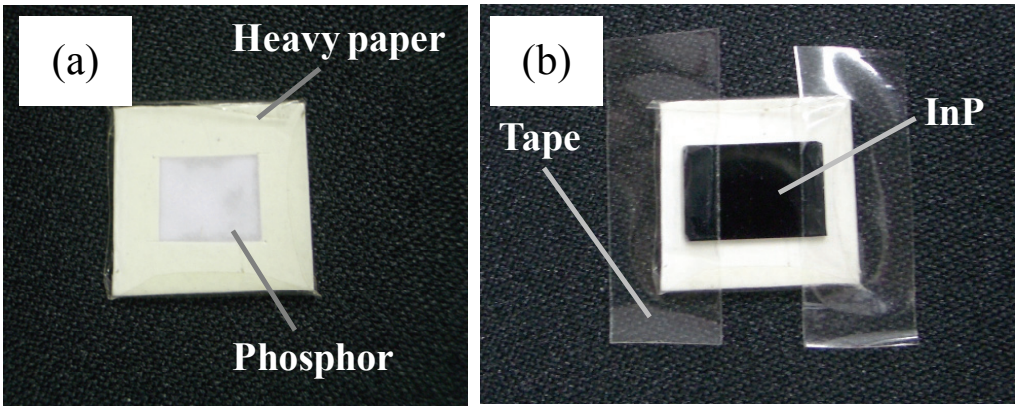

Fig. 29 (a) Phosphor that is enclosed in a cell made of heavy paper and adhesive tape; (b) InP put on the phosphor cell and fixed with adhesive tape.

2.2.2. Results of phantom measurement

The results of the phantom measurement are shown in Fig. 30. The horizontal axis indicates each condition, and the vertical axis indicates the change in optical density (ΔOD). Means and standard deviations of ΔOD that were measured five times for Conditions 1 and 2 are shown. Bar charts indicate the means, and error bars indicate the standard deviations of ΔOD. In Condition 1, phosphor and optical filters were used, whereas they were not used in Condition 2. Means and standard deviations for Conditions 1 and 2 are 0.067 ± 0.008 and 0.0024 ± 0.0017, respectively.

The mean ΔOD in Condition 1 was about 30 times as large as that in Condition 2. This difference was induced by the difference in mean effective path length (L_{eff}) in POM resin. In Condition 2, the light detector catches the photons from various positions on the phantom surface because of the light reflected from the superficial layer. If there are multiple distances between irradiation and detection positions, L_{eff} is expressed as

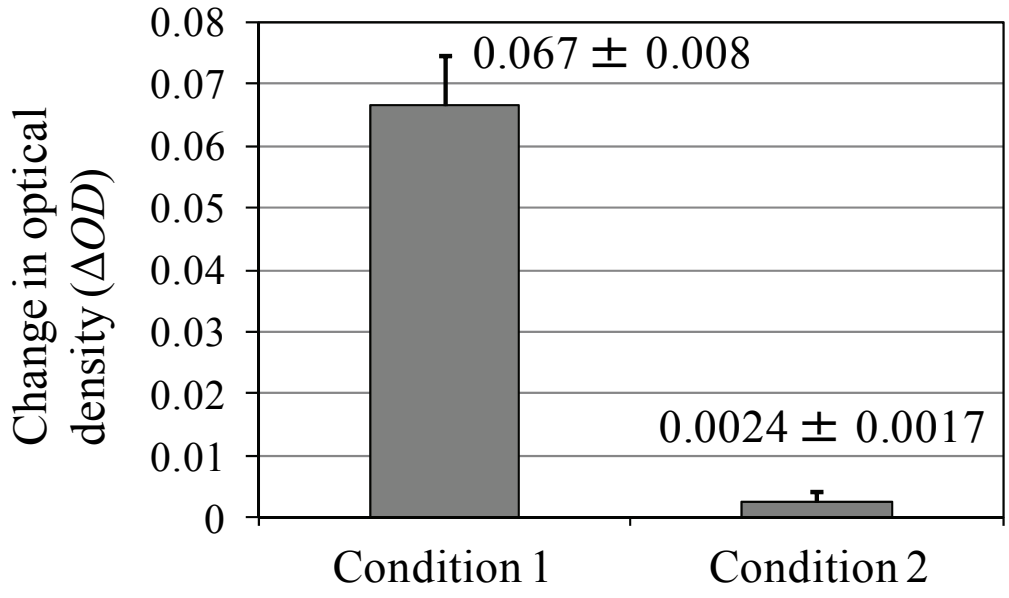

Fig. 30 Results of phantom measurement. Means (bar charts) and standard deviations (error bars) of the changes in optical density (ΔOD) that were measured five times in Conditions 1 and 2 are shown. In Condition 1, phosphor and optical filters were used, whereas they were not used in Condition 2.

$$L_{eff} = \frac{\int p(\rho)L(\rho)d\rho}{\int p(\rho)d\rho}, \tag{13}$$

where ρ represents SD distance, $L(\rho)$ represents mean effective path length in POM resin, and $p(\rho)$ represents detected power, both of which are the functions of ρ. According to Eq. (13), L_{eff} is the weighted mean of $L(\rho)$ by the intensity of the detected power. In Condition 1, L_{eff} is nearer to $L(\rho = 30$ mm) than that in Condition 2 is because ρ can be assumed to be approximately unique because only the position of phosphor on the phantom surface can be assumed to be a dominant detection point, whereas in Condition 2, APD might detect a lot of light from the positions where SD distances were less than 30 mm, including skin-reflected or stray light, instead of the desired detection position. Here, $p(\rho < 30$ mm) is larger than $p(\rho \geq 30$ mm) because if the SD distance is shorter, the photons propagate more shallow paths, and also, both $L(\rho)$ and the total optical path length in the phantom become shorter. This results in less attenuated light due to the absorption by POM resin and the base material of the phantom. Therefore, the contribution of $p(\rho < 30$ mm) in Condition 2 causes L_{eff} to be shorter than $L(\rho = 30$ mm), which caused the reduction in sensitivity to the absorption change in the deep region. In this way the use of phosphor and optical filters is very important to improve the sensitivity to the absorption change in the deep region.

2.3. Human brain activity measurement

2.3.1. Participant

One male adult (28 years old) participated as a volunteer subject in this study. The subject provided written informed consent after a complete explanation of the study.

2.3.2. Measurement system

We conducted a human brain activity measurement using our noncontact system. Figure 31 shows the experimental setup of the system. The system was almost the same as the one described in the phantom measurement section except for the lenses

and light sources. As light sources, two LEDs (735- and 805-nm wavelengths) were used. The diameter and the focal length of the lenses were both 15 mm (shorter than those in the phantom measurement) to achieve the simultaneous measurement with the conventional OT system stated below. On the light-detector side, the same lenses were placed in the same way between the APD and the detection point on the skin. The distance between the irradiation and detection focal points was 30 mm.

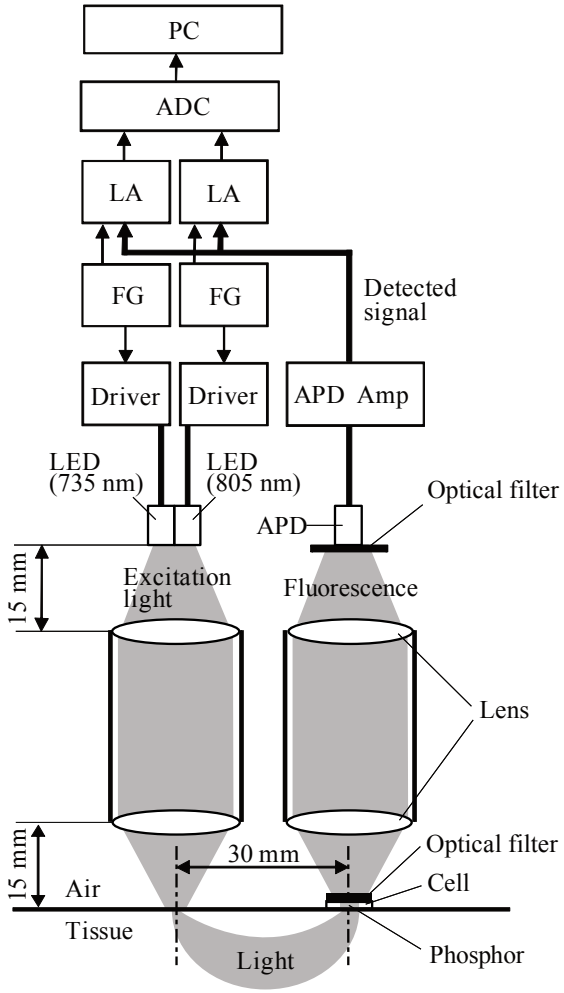

Fig. 31 Experimental setup of a noncontact brain activity measurement system. LED stands for light-emitting diode, APD stands for avalanche photodiode, FG stands for function generator, Amp. Stands for amplifier, LA stands for lock-in amplifier, ADC stands for analog-digital converter, and PC stands for personal computer. The phosphor placed on skin is only excited by tissue-propagated light. The APD detects only fluorescence, while excitation and stray light are cut using two InP wafers. Two light beams (each with a different wavelength) from two LEDs are intensity modulated at different frequencies, and the fluorescence signals excited by each beam are discriminated by lock-in detection.

The two LEDs were attached to each other's side surface so that they were focused on the same point on the skin. The output power of each LED was about 3 mW on the skin surface. The phosphor and an InP wafer were attached to the detection position on the skin. One adult male participated in the experiment as a volunteer subject.

In this study, to validate the noncontact system described above, the activity of the prefrontal cortex was measured by using the noncontact measurement system as well as a commercially available conventional OT system (ETG-7100, Hitachi Medical Corporation, Japan). The irradiation and detection position on a subject was determined in accordance with the International 10-20 system (Jasper, 1958), namely, the standard method for electrode placement in electroencephalography. Figure 32 shows the probe arrangement of the noncontact system and the conventional OT system. Figure 33 shows a photograph of experimental setup for simultaneous measurement with both noncontact system and conventional OT system. The source-detector (SD) distances in the noncontact and conventional OT systems were set to 30 and 35 mm, respectively. The center point between the irradiation focal point and the detection focal point in each system was located at the center of the forehead ("Fpz"). Although the SD distance is usually set to about 30 mm, the SD distance for the conventional OT system in this study was set to 35 mm because of the restriction of the probe placement. With the noncontact system, the phosphor and the InP wafer (used as an optical filter) were placed in the detection position labeled the "Noncontact detection focal point" in Fig. 32. The two systems did not interfere with each other because the wavelengths used in the conventional OT system (695 and 830 nm) are out of the range for phosphor excitation, and the frequency of the lock-in detection used in the conventional OT system was over 10 kHz that is much higher than that used in the noncontact system.

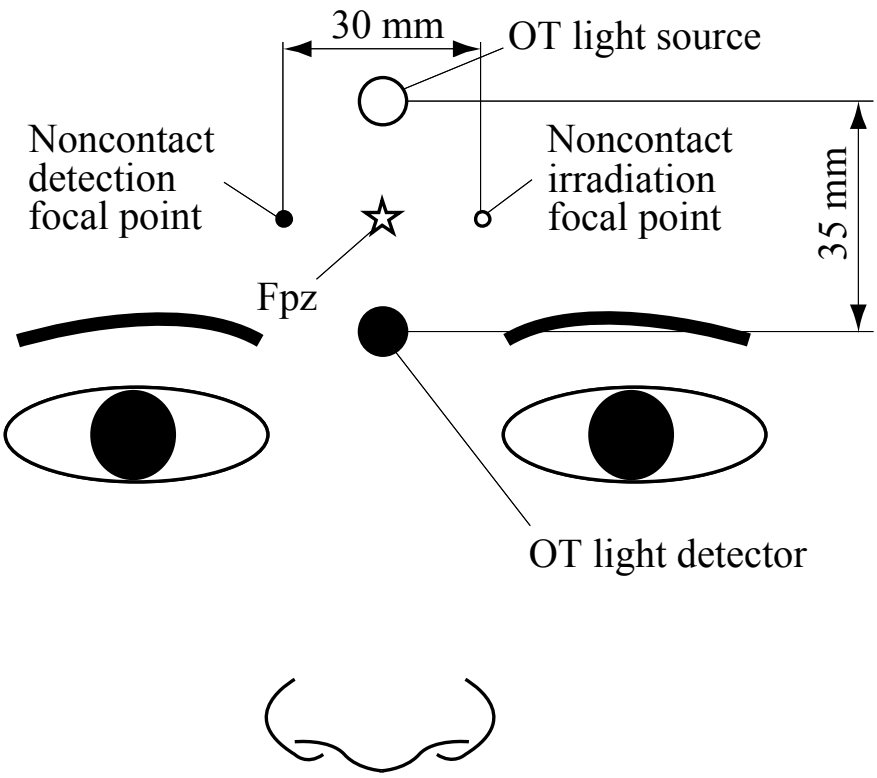

Fig. 32 Probe arrangement of the noncontact system and a conventional optical topography system. On the subject's forehead, the center point between the irradiation and detection focal points for each system is located at Fpz.

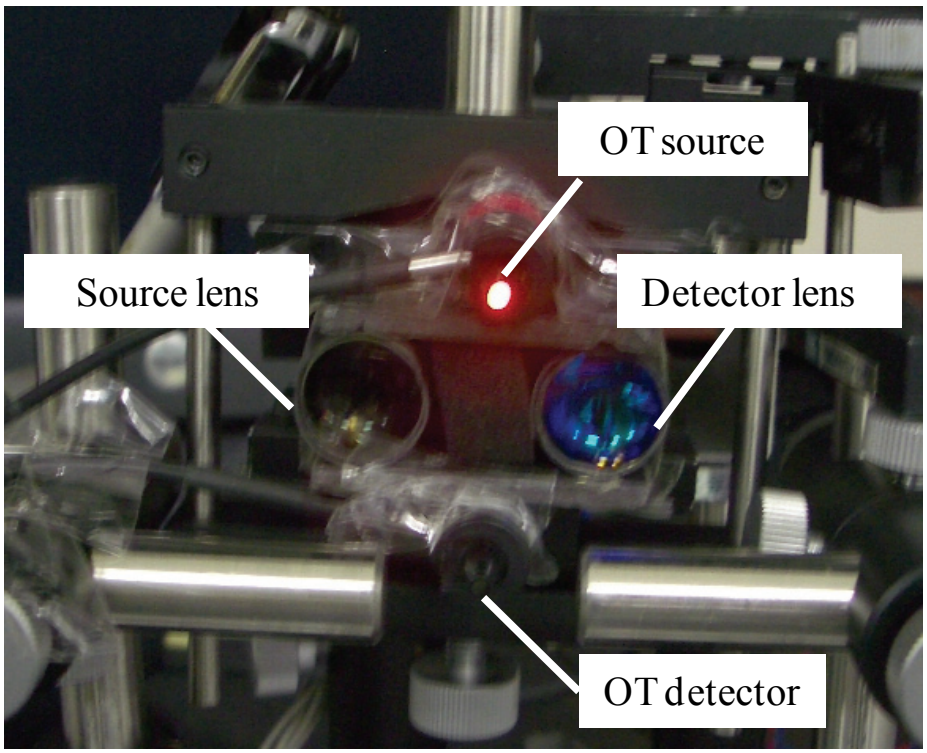

Fig. 33 Photograph of experimental setup for simultaneous measurement with both noncontact system and conventional OT system.

2.3.3. Cognitive task for brain activation

The anterior prefrontal cortex (or Brodmann's Area 10) is especially large in human compared with other animals, which activates during some cognitive processes, such as memorizing, planning, executive functioning, and language (Fuster, 1997). In this study, to activate the prefrontal cortex of the human brain, a spatial working-memory task was conducted. This task was used in a previous NIRS study (Tsujimoto et al., 2004), and therefore, the Hb response pattern in the prefrontal cortex generated by performing this task was already known.

The sequence of this task and examples of the presented screen images is shown in Fig. 34. In each trial, the subject was requested to memorize the positions of four white squares on a "target screen" displayed for 1.5 s. The subject holds the memory while a following 7-s "delay screen," on which a white fixation cross (+) sign was displayed in the center of a black screen, was presented. Then, while a "probe screen" with a white square was presented, the subject judged whether or not the white square on the "probe screen" was in the same position as any of the four squares on the "target screen." If so, the subject pushed the right button on a game pad in front of him/her as quickly as possible; otherwise, he/she pushed the left button in the same way. The "probe screen" was then switched to a "rest screen," which was the same as the "delay screen," within 2 s, and the "rest screen" was displayed for a randomized time period ranging between 16 and 21 s. The subject was required to look at a white fixation cross when the "delay screen" or "rest screen" was presented. This sequence was repeated for sixteen trials. In this task the subject had to hold the spatial information of squares in memory for 8.5 s in each trial.

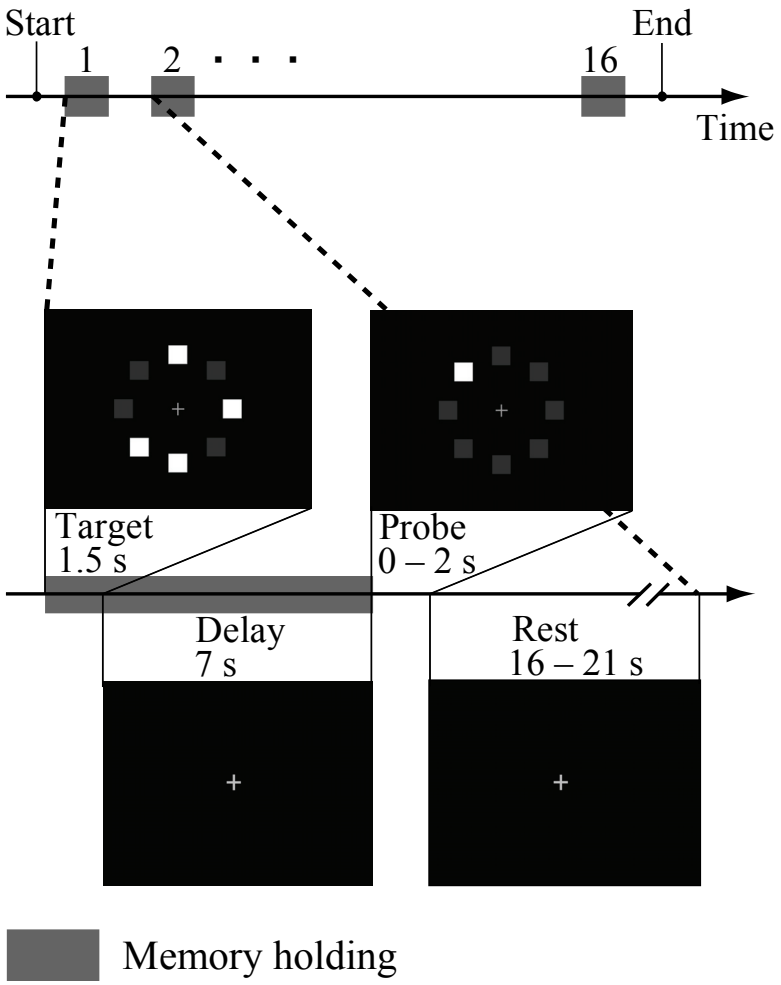

Fig. 34 Sequence of a spatial working memory task used for measuring brain activation. The subject was requested to look at the center of the screen during the experiment and to memorize the positions of four white squares on a target screen and judge whether a white square on a probe screen was in the same position as any of the squares on the target screen. The subject had to hold the initial square information in memory for 8.5 s during the target screen and delay screen in each trial.

2.3.4. Analysis of human brain activity measurement

The oxy- and deoxy-Hb changes were calculated from the absorbance changes of the excitation light with two different wavelengths according to the modified Beer-Lambert law (Delpy et al., 1998; Maki et al., 1995). In the calculation, the absorption coefficients (Matcher et al., 1995a) of the center wavelengths, 735 and 805 nm, were used even though the light beams of LEDs have a 40-nm spectral width. For both systems, the sampling rate was 10 Hz in the analysis after the data of the noncontact system were downsampled.

The data were processed with a 0.8-Hz low-pass filter and were smoothed with a convolution of a Gaussian function with a full width at half maximum of 2 s. All the trial data were fitted to a linear function to eliminate baseline fluctuations. Moreover, one-tailed Student's t-tests using the data obtained from the rest and memory-holding periods were conducted, and the data indicating that oxy-Hb was significantly increased ($p < 0.05$) in the memory-holding period were extracted and averaged. In the present study, only oxy-Hb change was used for the significance test because the SNR of deoxy-Hb change was lower, and the oxy-Hb change is a better indicator of cerebral blood volume (Hoshi et al., 2001).

2.3.5. Results of human brain activity measurement

Figure 35 shows time course data of the Hb changes [$\Delta(C \times L)$] at all blocks observed by the noncontact system and the conventional OT system during a spatial working memory task. The memory-holding period is between the onset of the target screen (t = 1 s) and probe screen (t = 9.5 s). Box frames indicate the blocks where oxy-Hb significantly increased.

Table 3 shows correlation coefficients between waveforms of our noncontact system and conventional OT system. In eight out of sixteen trials, the correlation coefficients between the oxy-Hb changes in both systems exceeded 0.6. In three trials, the correlation coefficients between the deoxy-Hb changes exceeded 0.7. The averages of the correlation coefficients for all trials were 0.51 and 0.16 for oxy- and deoxy-Hb, respectively. The oxy-Hb significantly increased in five of the sixteen trials in both systems.

The data in these five trials were used to calculate the averaged waveforms of the oxy- and deoxy-Hb changes [$\Delta(C \times L)$] observed by the noncontact system [Fig. 36 (a)] and the conventional OT system [Fig. 36 (b)]. The horizontal axis represents time, and the vertical axis represents the amplitude of the oxy- and deoxy-Hb changes (mM・mm). The bold line and thin line respectively indicate the oxy- and deoxy-Hb changes. The bold line on the time axis indicates the time range of memory holding. Error bars

indicate standard errors in the data in five trials.

The mean waveforms obtained by both systems had very similar shapes, and the peak times of oxy- and deoxy-Hb were almost the same. The correlation coefficients between the Hb changes obtained by both systems were 0.90 and 0.83 respectively for oxy- and deoxy-Hb. The data obtained by each system contained 255 points.

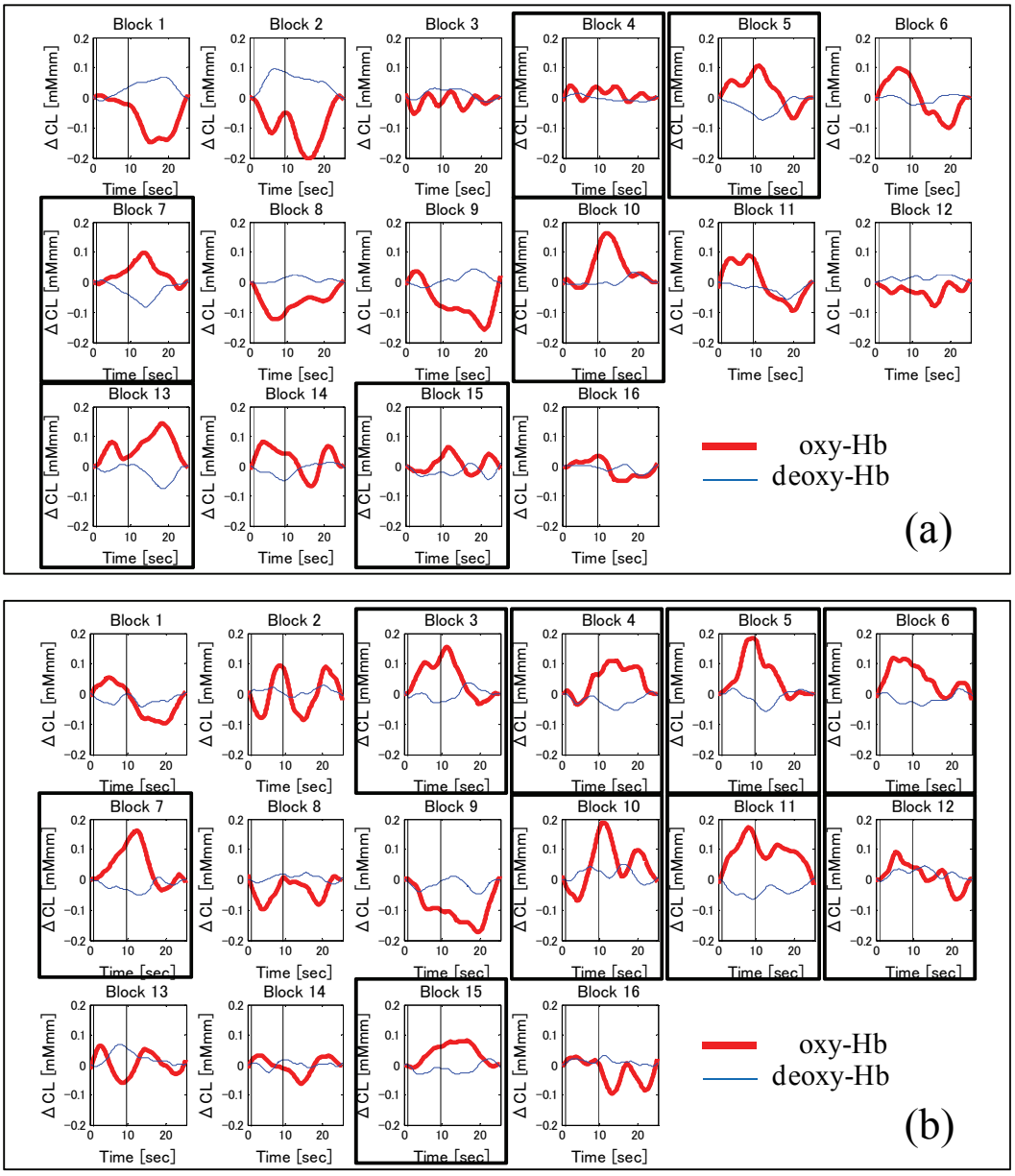

Fig. 35 Time sequence data of the Hb changes [$\Delta(C\times L)$] at all blocks observed by (a) the noncontact system and (b) the conventional OT system during performance of a spatial working memory task. The memory-holding period is between the onset of the target screen (t = 1 s) and probe screen (t = 9.5 s). Box frames indicate the blocks where oxy-Hb significantly increased.

Table 3 Correlation coefficient between waveforms of our noncontact system and conventional OT system.

	oxy-Hb	deoxy-Hb		oxy-Hb	deoxy-Hb
Block 1	0.95	-0.32	Block 9	0.84	-0.21
Block 2	0.44	0.01	Block 10	0.84	-0.18
Block 3	0.22	-0.40	Block 11	0.29	0.32
Block 4	0.24	0.15	Block 12	-0.22	0.18
Block 5	0.79	0.91	Block 13	0.33	0.39
Block 6	0.86	0.70	Block 14	0.69	-0.23
Block 7	0.75	0.75	Block 15	0.20	-0.18
Block 8	0.36	0.49	Block 16	0.60	0.24

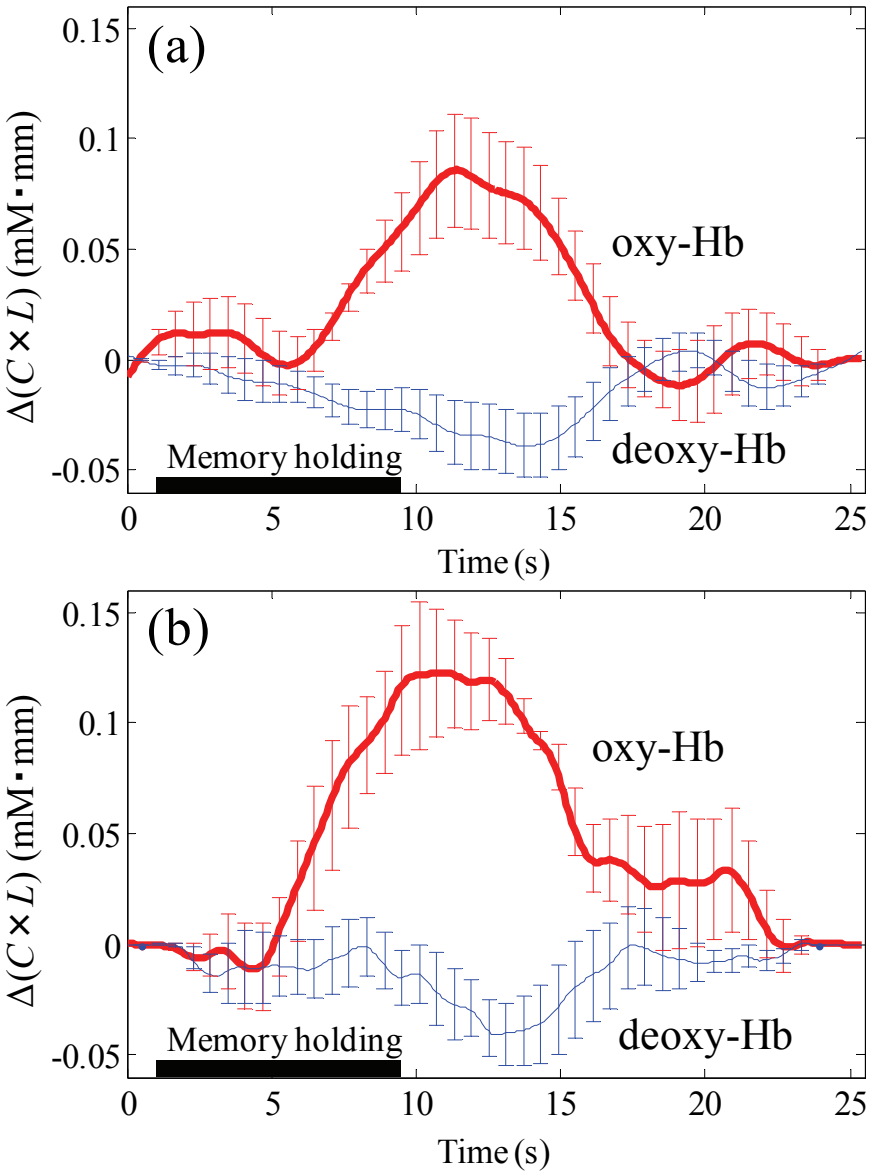

Fig. 36 Time course data of the Hb changes [$\Delta(C \times L)$] observed by (a) the noncontact system and (b) the conventional OT system during a spatial working memory task. Error bars indicate standard errors. The memory-holding period is between the onset of the target screen (t = 1 s) and probe screen (t = 9.5 s).

2.4. Comparison with conventional NIRS system

The mean optical paths of the two systems are different because the positions of irradiation and detection points of them are different. In the gray matter of the brain, however, the photons from both systems propagate through almost the same area because the midpoints of irradiation and detection points of these systems are the same. When the changes in the cerebral blood volume are obtained, similar waveforms would therefore be obtained. If the waveforms were not similar, it would be due to the effect of local changes in the extracranial blood volume during the experiment. It has been reported that superficial task-evoked artifacts are not homogeneous, but rather localized in the scalp draining veins (Kirilina et al., 2012). According to the results of this study, similar averaged waveforms were obtained with both systems. This similarity demonstrates that both systems measured changes in the cerebral blood volume.

The peak amplitude of the noncontact system was smaller than that of the conventional OT system. The slope of oxy-Hb increase is also smaller for the noncontact system. That was probably because the SD distance in the noncontact system was smaller than that in the conventional OT system. Based on the partial differential path-length factor of gray matter of an adult head model, reported by Fukui et al. (2003), the partial optical path length of gray matter with a 35-mm SD distance is about 1.4 times larger than that with a 30-mm SD distance. The experimental results of this study indicate that the peak amplitude of oxy-Hb obtained by the conventional OT system was 1.43 (0.123 mM･mm / 0.086 mM･mm) times larger than that obtained by the noncontact system. Thus, the difference between the peak amplitudes in both systems can be explained by the difference in SD distance.

The correlation coefficients between the Hb changes obtained by both systems were 0.90 and 0.83, for the oxy- and deoxy-Hb changes, respectively. There was a slight difference between the correlation coefficients for oxy- and deoxy-Hb changes [$\Delta(C \times L)$] for two reasons. First, the amplitude of deoxy-Hb change is much smaller than that of oxy-Hb change, so the SNRs of oxy- and deoxy-Hb changes are different.

The second reason is due to the effect of the changes in extracranial blood volume. In the two systems, the optical paths through the scalp were different, and the contribution ratio of the oxy- and deoxy-Hb changes in the scalp to the obtained Hb change is not necessarily equal to that in gray matter.

The Hb response in the prefrontal cortex induced by the spatial working memory task used in this study is already known (Aoki et al., 2011; Sato et al., 2011; Tsujimoto et al., 2004). The typical waveform of oxy-Hb has a large peak at 8–9 s after task onset of the target screen (t = 9–10 s). In this study, the averaged wave shape obtained with the noncontact system was similar to that obtained with the conventional OT system. Moreover, the data from both systems had a typical Hb response. Considering that the optical path lengths for the two systems are partly shared in the gray matter of the brain but are not shared in the extracranial tissue, we think that the noncontact system measures the brain activity as well as the conventional OT system. Although the results for only one subject are shown here, the results presented above are sufficient to validate the noncontact system because similar Hb data were obtained by both the noncontact system and the conventional OT system, and the data were consistent with those in the literature.

Compared at each single trial, some oxy-Hb signals obtained by two systems are positively correlated, whereas others are not correlated with each other. Especially in blocks 8 and 9, oxy-Hb signals decreased, which is not typical response expected by the literatures (Aoki et al., 2011, Sato et al., 2011; Tsujimoto et al., 2004). This might be caused by the physiological fluctuations (Tong et al., 2011). Decrease of the oxy-Hb change during cognitive tasks has been reported by several researches (Pfurtscheller et al., 2010; Kirilina et al., 2012). The effects of superficial layer should not be ignored because the optical paths in the superficial layer are not shared for both systems. To remove or suppress the effects caused by the superficial layer, the trial-averaging is calculated by using time series Hb signals measured at repeated trials.

It should be noted that there are some differences between ΔCL data obtained by the noncontact system and the conventional system. The onset time of oxy-Hb

increase is different. Moreover, a frequency characteristics of waveforms is different. These differences are mainly induced by difference of irradiation and detection positions, which have lead that each signal include different superficial-layer signal. These artifacts could be cancelled by repeating more trials. Because this effect probably depends on individuals, it would be important to perform this experiment on more subjects and to investigate physiological issues.

In this way, trial-averaging is not enough for eliminating artifacts induced by superficial layer, multiple distance optodes are therefore necessary to cancel the effect of superficial layer. To easily materialize the multi-distance measurement, optical scanning system is one of the effective solutions, which will be described in Chapter 3 in detail.

2.5. Evaluation of precision

A precision indicator of detected light, namely, carrier-to-noise ratio (CNR), was defined by considering the detected light as a carrier wave, whose amplitude is modulated by the oxy- and deoxy-Hb changes. CNR is expressed as

$$CNR_i \equiv 20 \log_{10} \frac{I(\lambda_i)}{\delta I(\lambda_i)} \text{ (dB)}, \tag{14}$$

where i is the i-th wavelength, $I(\lambda_i)$ is the intensity of detected light, and $\delta I(\lambda_i)$ is the measurement error of $I(\lambda_i)$.

The CNR of the noncontact system was calculated as 37 dB for downsampled 10-Hz data during a rest period in the human brain measurement. The CNR of the conventional OT system (sampling rate: 10 Hz) was about 40 dB for an SD distance of 30 mm. That is to say, the CNR of the noncontact system was about 3 dB lower than that of the conventional OT system.

The time constant of the LA was set to 1 s for the noncontact system. The hemodynamic response is 2–10 s (Aslin and Mehler, 2005), so the 1-s time constant is short enough to detect the cortical response to the working memory task. If the

frequency response of the system were as fast as that of the conventional OT system, the time constant would be less than 100 ms, so the change in heart rate could be efficiently obtained. A shorter time constant, however, would lower CNR by about 10 dB according to the following equation,

$$20\log_{10}\sqrt{1000/100} = 10 \text{ dB}, \tag{15}$$

because the noise (considered to be white) decreases in proportion to the square root of the averaging time.

The optical power for the two wavelengths of the noncontact system was 3 mW, whereas that of the conventional OT system was 2 mW. According to Eq. (14), it can be assumed that the CNR is proportional to the optical power of the detected light when the measurement error does not change. The CNR of the noncontact system would therefore be lowered by one third (–3.5 dB) if the optical power of the noncontact system were 2 mW.

When the time constant was 100 ms and the optical power of each wavelength was 2 mW in the case of the noncontact system, namely, the same conditions for averaging time and optical power as the conventional OT system, the CNR would become 23.5 dB (i.e., 37 – 10 – 3.5). The CNR of the noncontact system under that condition is less than that of the conventional OT system by 16.5 dB (i.e., 40 – 23.5). It is assumed that the deterioration in CNR was caused by the transduction loss in fluorescence generation and the loss of optical power due to optical filters and an alignment error of the optical system.

2.6. Benefits of noncontact system

Using the noncontact system, the focal positions of irradiation and detection on the skin can be easily changed and adjusted. By using mirrors and lenses and by quickly adjusting these focal positions, it is possible to obtain large data sets under various conditions of SD distances with a small number of light sources and detectors, which

leads to further improvement in the accuracy of measurement. The measurement position can be flexibly changed according to the shape or size of the subject.

Such a system might be able to create an image of Hb change with a higher depth resolution. The costs of light sources and detectors would then be reduced. The light detectors could be replaced by an infrared charge-coupled device (CCD) camera in the future if suitably sensitive and stable devices were available. The noncontact system imposes no skin compression, which is much more comfortable for subjects during measurement. This system can therefore be applied for long-term measurements, for example, monitoring resting-state spontaneous fluctuations in the brain.

2.7. Summary of the developed system

A noncontact optical measurement system based on NIRS was described. This system uses phosphor on the skin and optical filters to eliminate excitation and stray light. The optimization of the intensity-modulation frequency was also described. The phosphor used was $Li(Nd_{0.9}Yb_{0.1})P_4O_{12}$, for which suitable excitation-light wavelengths are within two ranges, 730 to 760 and 790 to 820 nm. In these wavelength ranges, light transmits well in biological tissues. We investigated the relationship between the fluorescence lifetime of the phosphor and the detected lock-in output in an experiment and a simulation, and demonstrated that the lock-in output decreased at higher frequencies of the intensity modulation. The frequency range of 200 to 300 Hz was practically suitable for the intensity modulation of the light sources in consideration of fluorescence lifetime and commercial power frequency in this study's experimental conditions.

A phantom measurement was conducted to investigate the effect of phosphor and optical filters in a noncontact system on the sensitivity to the absorption change in the deep region. The results showed that mean ΔOD with phosphor and optical filters was about 30 times as large as that without phosphor and optical filters. The use of phosphor and optical filters therefore greatly improved the signal-to-noise ratio of the

absorption change in the deep region in a noncontact system.

A simultaneous measurement of human prefrontal cortex during a working memory task using the noncontact system and conventional OT system was conducted to confirm that the noncontact system monitors the brain activity rather than changes in the skin blood. As a result, typical Hb responses were obtained with both systems. It was also found that the shapes of the Hb-change waveforms obtained by the two systems were similar (correlation coefficients between the data obtained by both systems were 0.90 for oxy-Hb and 0.83 for deoxy-Hb). This similarity of Hb responses and their typical waveforms confirmed that the noncontact system can monitor human brain activity as well as a conventional OT system.

Chapter 3

Optical scanning system

3.1. Introduction

The near-infrared (NIR) light inevitably propagates in superficial tissue even when a deep region of tissue is of interest; accordingly, the effects of superficial tissue on the NIRS signal should be taken into account if they are not negligible. It has been reported that for brain measurements, the absorption of NIR light by the scalp and the thickness of the skull influence the NIRS signal (Okada and Delpy, 2003). When skeletal-muscle oxygenation is optically measured by NIRS, the adipose-tissue thickness affects the intensity of detected light, signal-to-noise ratio, and the optimal source-detector (S-D) distance at which the sensitivity of NIRS to the muscle-tissue oxygenation is maximal (Feng et al., 1997; van Beekvelt et al., 2001; Yang et al., 2005).

Measurement utilizing multiple S-D distances (multi-distance measurement) has been proposed as a solution for discriminating and eliminating the effect of superficial tissue (Fabbri et al., 2004; Saager and Berger, 2005; Saager et al., 2011; Umeyama and Yamada, 2009; Yamada et al., 2009; Zhang et al., 2007a). For example, the signals from the layers were calculated on the basis of a two-layer head model by

solving simultaneous equations with data input obtained from two source-detector distances (Fabbri et al., 2004). Other solutions use subtraction methods with a short-distance reference incorporating either least-squares fitting (Saager and Berger, 2005; Saager et al., 2011), or an adaptive filter (Zhang et al., 2007a; Zhang et al., 2007b). Furthermore, for eliminating the effect of systemic hemodynamics from NIRS signal obtained from human head, a method utilizing a Monte Carlo simulation with multiple S-D distances was proposed (Umeyama and Yamada, 2009; Yamada et al., 2009). A method of compensating the effect of adipose-tissue thickness in measuring muscle-tissue oxygenation has also been reported (Niwayama et al., 2000; Niwayama et al., 2006); however, using this method necessitates measuring adipose-tissue thickness in advance by ultrasonography. Since the optical properties of skin vary across individuals, the S-D distance at which the sensitivity of NIRS is maximum changes even though the adipose-tissue thickness is constant. To determine the optimal S-D distance for individuals, the measurements at multiple distances are necessary. Accordingly, to obtain the optimal S-D distance and compensate for the effect of superficial tissue, an optical scanning system that can perform such multi-distance measurement is required (Niwayama et al., 2000; Niwayama et al., 2006; Saager and Berger, 2005; Saager et al., 2011; Umeyama and Yamada, 2009; Yamada et al., 2009; Zhang et al., 2007a).

In Chapter 3, I present an optical scanning system, which has a noncontact light emitter and detector and can measure the absorption change at variable S-D distances, as a methodology for multi-distance biological measurement. Few researches on noncontact optical scanning system for performing a multi-distance light-absorption measurement of deep biological tissue have been reported because it is a problem that a noncontact light detector detects surface-reflected light (originally from a noncontact light emitter) rather than tissue-propagated light. To solve this problem, we have devised a method using a phosphor (on the skin) and optical filters for cutting excitation light so that only fluorescence emitted from the phosphor (excited by tissue-propagated light) is detected (Funane et al., 2010; Funane et al., 2011a).

The purpose of this chapter is to show the effectiveness of a noncontact NIRS

scanning system for measuring deep biological tissue with multiple layers. In particular, a one-dimensional optical scanning system with a galvano scanner was developed, and the system was validated by measuring a tissue-simulating phantom.

3.2. System description

An optical scanning system, with a fixed detection focal point and a one dimensionally scanned irradiation focal point, was developed. The optical setup of the near-infrared scanning system is shown in Fig. 37. Overview of scanning system and phantom is shown in Fig. 38.

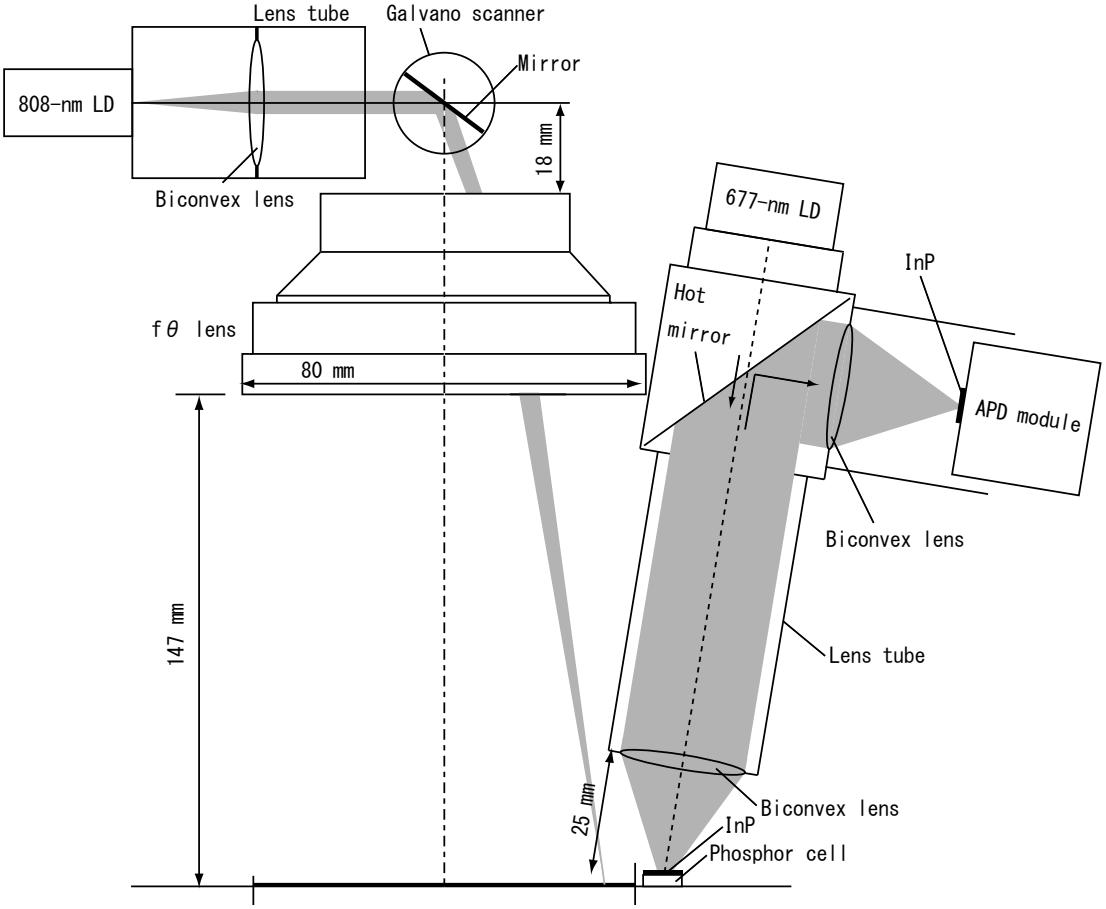

Fig. 37 Optical setup of scanning system.

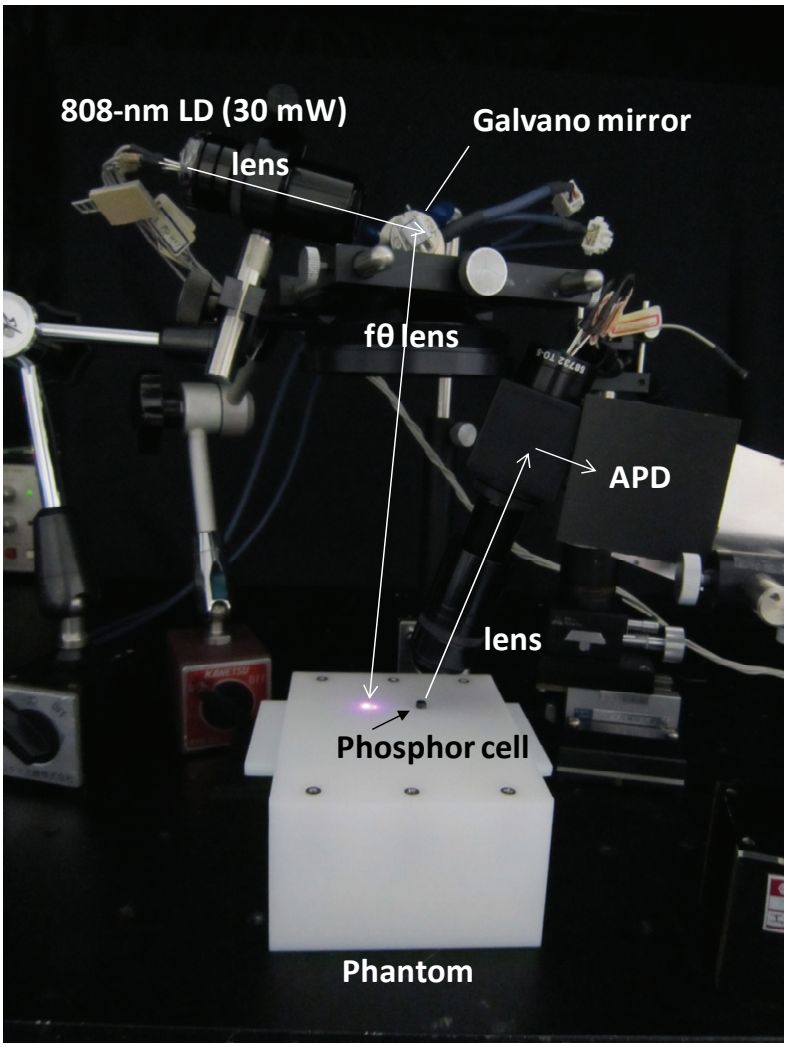

Fig. 38 Overview of scanning system and phantom.

Emitted light from an 808-nm laser diode (LD) (DL-8141-035, SANYO, Japan) fixed in the lens framework is collimated with a biconvex lens (diameter: 25 mm/focal length: 25 mm), reflected at a galvano scanner with a 19 × 19-mm aluminum mirror, and enters an fθ lens (S4LFT0101/094, Sill Optics, Germany), which focuses the incident light on the surface of the object. The distance between the irradiation focal point and the center axis of the lens is proportional to the incident light angle. The full-width-of-half maximum of incident-light power on the tissue surface was set to 1.05 mm.

To make it possible to measure the absorption change of tissue with a noncontact light emitter and detector, the wavelength of the tissue-propagated light is converted by a near-infrared phosphor on the surface of tissue, and excitation light is cut by

optical filters. As a result, only fluorescence is detected and discriminated with lock-in detection, whereas backscattered stray light is suppressed (Funane et al., 2010; Funane et al., 2011a). The phosphor used was $Li(Nd_{0.9}Yb_{0.1})P_4O_{12}$, which is excited at light wavelengths of 735 and 805 nm and emits 980-nm-wavelength light. It was placed on a fixed detection focal point. The fluorescence from the phosphor is collimated by a biconvex lens (diameter: 25 mm/focal length: 25 mm) and reflects on a hot mirror (T > 85% (425–675 nm)/R > 90% (750–1125 nm)). It is then focused by a biconvex lens (diameter: 25 mm/focal length: 25 mm) and enters an avalanche photodiode (APD) module (C5460-8375, Hamamatsu Photonics K.K., Japan) through an indium phosphide (InP) wafer used as an optical filter. The phosphor [$Li(Nd_{0.9}Yb_{0.1})P_4O_{12}$] was enclosed and bonded in a cell that consists of an aluminum ring (outer diameter: 4 mm/inner diameter: 3 mm/thickness: 1 mm) and an InP wafer attached on the top of the aluminum ring.

To reproducibly place the phosphor cell on the detection point on the phantom surface after the phantom setting is changed, a 677-nm LD (HL6720G, Hitachi, Ltd., Japan) (which transmits light through the hot mirror and focuses on the detection focal point) was placed on the light axis of the detection light. The 677-nm LD was driven before the multi-distance absorption measurement was performed. The axis of the detection light tilts 19 degrees from vertical owing to the constraint on the placement of the lens tube and hot mirror.

A block diagram of the scanning system is shown in Fig. 39. The laser diode was driven by a laser driver (ALP-7033CB, Asahi Data Systems Co., Ltd., Japan) that receives the analog output of a function generator (model 1930A, NF Corporation, Japan). The frequency of intensity modulation was set to 3.3 kHz. The function generator was controlled via a GPIB controller (GPIB-USB-HS, National Instruments Corporation, U.S.A.) by a personal computer (PC), called PC-2 here, so that the irradiation power of the light source can be adjusted according to S-D distance. A galvano scanner (controller: GC-201; motor: GM-1010; Canon Inc., Japan) was controlled via RS232C by PC-2. As a controller software, a MATLAB Version R2010b (The MathWorks Inc., U.S.A.) was used.

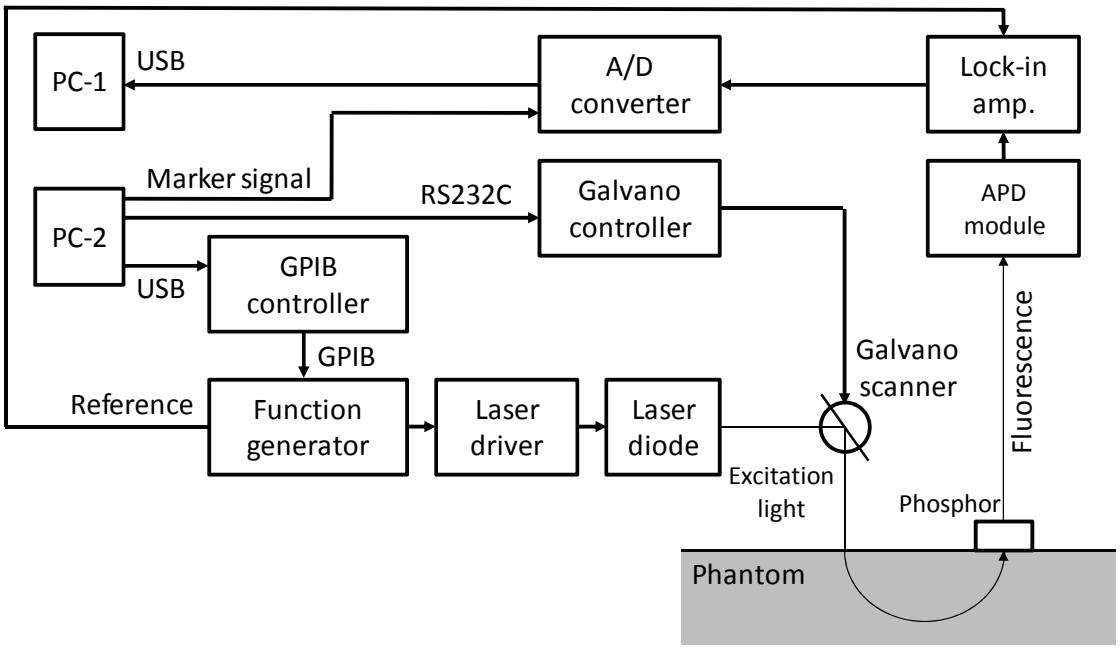

Fig. 39 Block diagram of scanning system.

The fluorescence emitted from the phosphor and caught by the APD is amplified by a trans-impedance amplifier in an APD module. After that, the amplified fluorescence signal is detected by a lock-in amplifier (model 5207, EG&G, U.S.A.), the output of which is converted to digital signal by an analog-digital converter (NR-2000, Keyence Corporation, Japan) and saved in PC-1 via a USB. The sensitivity and time constant of the lock-in amplifier were set to 10 mV and 10 ms (12 dB/oct), respectively. The sampling rate of the analog-digital converter was 1 kHz. To record the start time of the measurement, an analog marker signal was input into the analog-digital converter from PC-2. Twenty measurement points in total, where the S-D distance was changed from 7 to 45 mm at 2-mm intervals, were scanned by the system. The irradiation power was adjusted according to S-D distance in four steps. The galvano mirror was rotated by 0.5 degrees after each measurement point. (Corresponding optical angle was 1 degree.) Each measurement point was measured for three seconds so that the signal-to-noise ratio was improved. Dark current was measured when there was no excitation light. To calculate relative detected powers on all channels, at the three measurement points where the irradiation power was switched, the detected power was measured at both (i.e., pre- and post-switching)

irradiation powers. The irradiation power was determined in advance so that all detected signals were within the range of the analog-digital converter. The irradiation power at the phantom surface for each S-D distance is listed in Table 4.

The diameter of irradiation spot on the phantom surface was measured by the knife-edge method. On the midpoint of scanning-source trajectory at phantom surface, which is just under the mirror of galvano scanner (where S-D distance is 26 mm), the irradiation power was measured with an optical power meter (ADCE 8230E, sensor: 82311, ADC Corporation, Japan) with intervals of 0.1 mm. We fitted an integral

Table 4 Irradiation power at phantom surface for various S-D distances.

Measurement order	S-D distance (mm)	Irradiation power (mW)	Notes
1	7	0	Dark-current measurement
2	7	0.9	ch 1
3	9	0.9	Power-ratio measurement
4	9	2.4	ch 2
5	11	2.4	ch 3
6	13	2.4	ch 4
7	15	2.4	ch 5
8	17	2.4	Power-ratio measurement
9	17	14.6	ch 6
10	19	14.6	ch 7
11	21	14.6	ch 8
12	23	14.6	Power-ratio measurement
13	23	41.0	ch 9
14	25	41.0	ch 10
15	27	41.0	ch 11
16	29	41.0	ch 12
17	31	41.0	ch 13
18	33	41.0	ch 14
19	35	41.0	ch 15
20	37	41.0	ch 16
21	39	41.0	ch 17
22	41	41.0	ch 18
23	43	41.0	ch 19
24	45	41.0	ch 20

function of the Gaussian function to measured data and obtained parameters of Gaussian function such as mean value and standard deviation (σ). Figure 40 shows measured optical power, fitting line of optical power, and estimated distribution of optical power at each position of irradiation focal spot by knife-edge method. The full width at half maximum (FWHM) of optical power distribution that was calculated by $2\sqrt{2\ln 2}\cdot\sigma$ was 1.05 mm ($\sigma = 0.447$ mm).

3.3. Static phantom with one-layer absorber

To validate the scanning system, it was used to measure a tissue-simulating phantom. The phantom has a one-layer absorber (the absorption coefficient of which is variable) embedded in a base material with low-absorption and high-scattering characteristics. The base material is a white polyoxymethylene (POM). The reduced scattering coefficient and absorption coefficient of POM at 800 nm are 0.9 and 0.002 mm^{-1} (natural logarithm based), respectively. Three materials for absorbers, with absorption coefficients of 0.01, 0.02, and 0.03 mm^{-1}, were prepared.

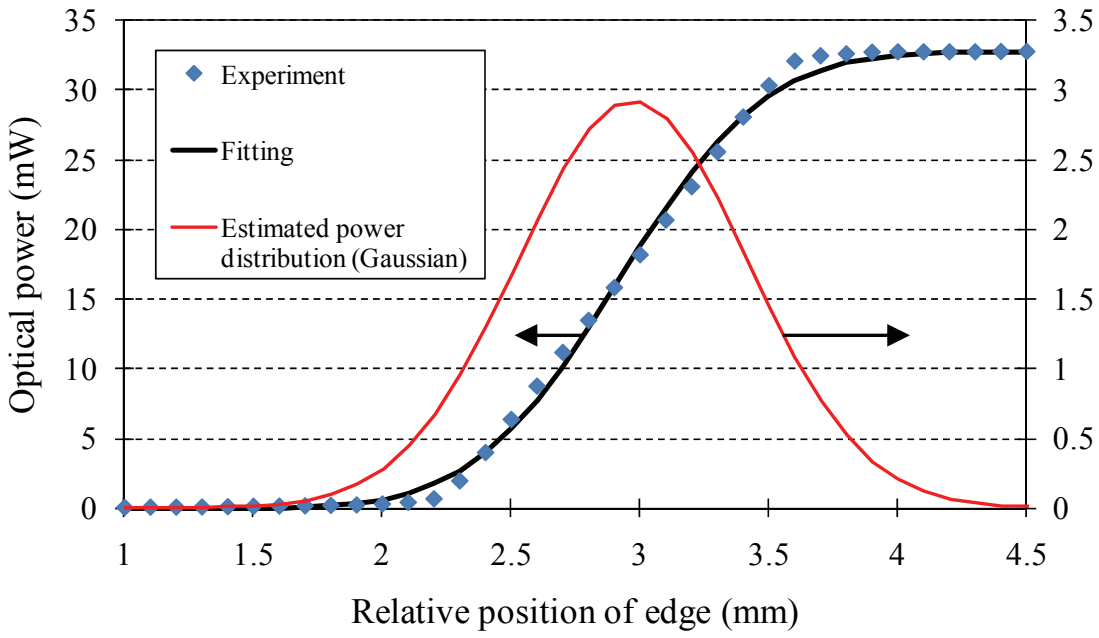

Fig. 40 Measured optical power, fitting line of optical power, and estimated distribution of optical power at each position of irradiation focal spot by knife-edge method.

The absorbers are made by mixing epoxy resin (MY753, Aeropia Chemical Supplies, Crawley, UK) and hardener (XD716, Aeropia Chemical Supplies, Crawley, UK) (Firbank et al., 1993; Firbank et al., 1995). To control the absorption coefficient of the absorbers, an infrared dye, Projet 830 (Avecia, Manchester, UK), is mixed in the absorber materials. The reduced scattering coefficient of the absorbers is 0.9 mm^{-1} to match that of POM. To control the reduced scattering coefficient of the absorbers, titanium dioxide (SuperWhite, Alec Tiranti Ltd., UK) is mixed into the absorbers. The scattering coefficients of six different concentrations of titanium dioxide were measured (Fig. 41) in advance and a linear calibration curve was obtained (Fig. 42). The optical properties of the absorbers and base material adjusted for the phantom are listed in Table 5.

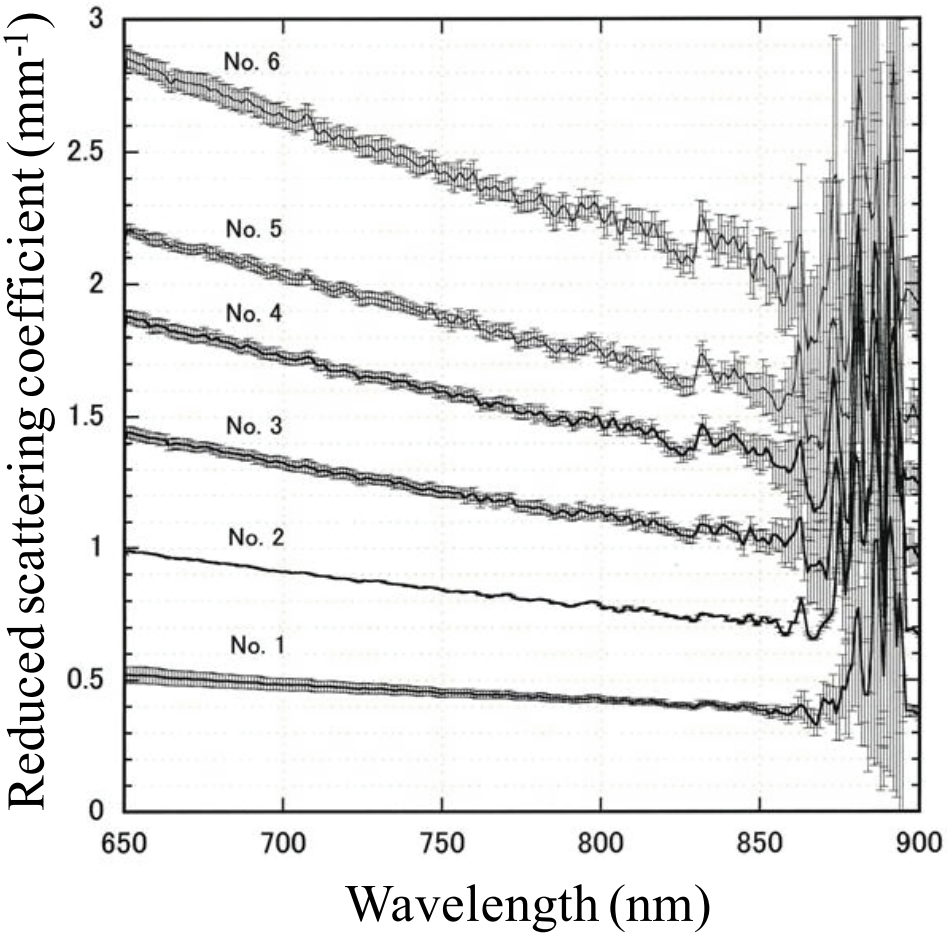

Fig. 41 Reduced scattering coefficient of epoxy resins that have six different concentrations of titanium dioxide.

The phantom is shaped as a cuboid with a size of 100 × 120 (horizontal) × 60 (Vertical) mm. A cuboidal cavity with a size of 100 × 60 × 5 mm is made at a certain depth. The materials for absorber and a scattering material (made of white POM) are inserted into the cavity to locally change the absorption of light. The phantom has a multi-sheet structure. And refractive-index matching liquid is not inserted between the sheets of materials because the air gaps between sheets of materials are very thin and the effect of refractive index mismatch is considered negligible.

The absorption spectrum of the infrared dye (Projet 830) used in our phantom is shown in Fig. 43. A spectrometer (USB4000, Ocean Optics, U.S.A.) was used for measuring it. The wavelength at which the absorption is highest is 810 nm.

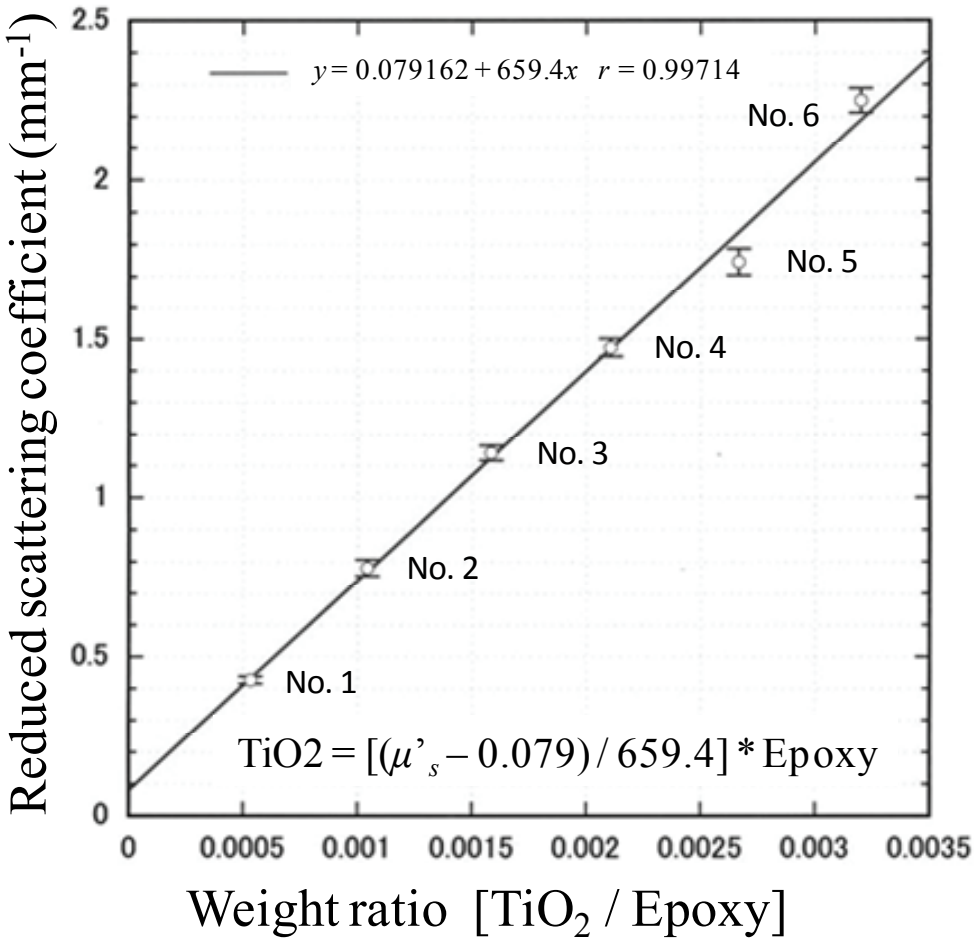

Fig. 42 Calibration curve for epoxy resin with titanium dioxide as scatterer.

Table 5 Optical properties of phantom material.

Phantom types	Materials	Reduced scattering coefficient μ'_s (mm^{-1}) at 800 nm	Absorption coefficient μ_a (mm^{-1}) at 800 nm
Background scatterer	White polyoxymethylene (POM)	0.9	0.002
Absorber no. 1	Epoxy resin Infrared dye (Projet 830) Titanium dioxide (SuperWhite)	0.9	0.01
Absorber no. 2	Epoxy resin Infrared dye (Projet 830) Titanium dioxide (SuperWhite)	0.9	0.02
Absorber no. 3	Epoxy resin Infrared dye (Projet 830) Titanium dioxide (SuperWhite)	0.9	0.03

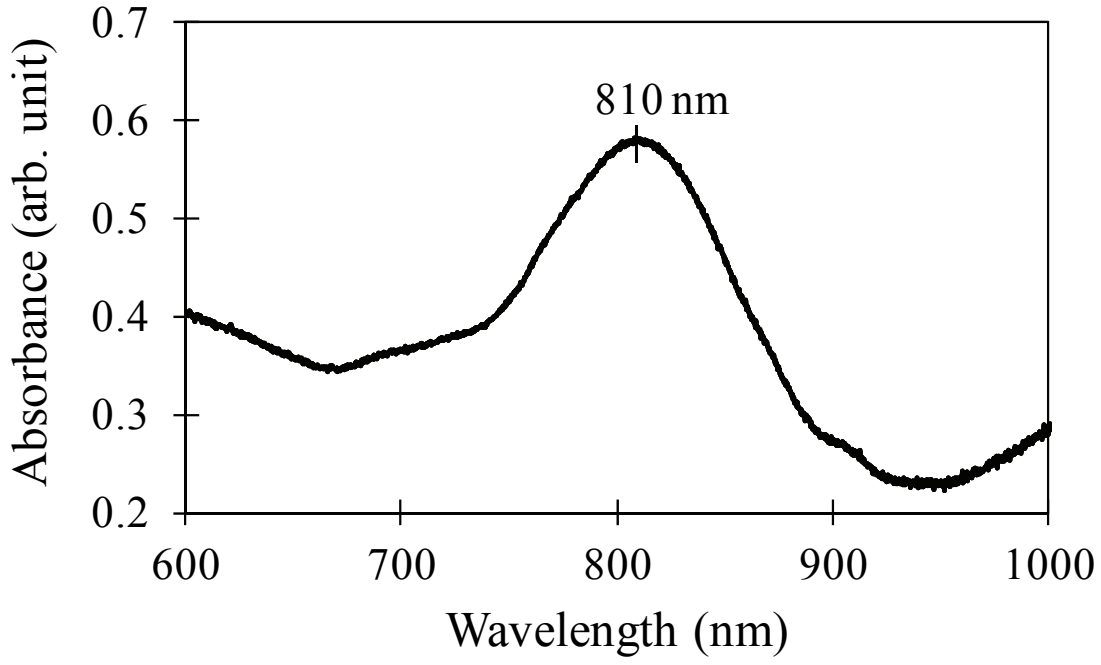

Fig. 43 Absorbance spectrum of infrared dye Projet 830.

3.4. Measurement of tissue-simulating phantom

In the experiment, changes in optical density (ΔOD) of the phantom were measured as the inserted absorber was changed from white POM to absorber number i (where i = 1, 2, or 3). ΔOD was calculated according to the following equation,

$$\Delta OD = -\ln\left[I_i / I_0\right] \qquad (i = 1,2,3), \tag{16}$$

where I_0 and I_i represent the intensity of detected light with white POM and that with absorber i, respectively.

3.4.1. S-D distance dependence of optical-density change

The changes in ΔOD of the phantom were measured when the surface-layer thickness was changed, namely, 1, 2, 4, 6, 8, 10, and 12 mm. The dependence of ΔOD on S-D distance for various surface-layer thicknesses was investigated. The height of the phantom was kept to 60 mm by adjusting the thickness of base material beneath the absorber even when the surface-layer thickness was changed.

Dependence of ΔOD on S-D distance for each surface-layer thickness is plotted in Fig. 44. Graphs (a) to (g) show the change of optical density (ΔOD) when the surface-layer thickness was 1, 2, 4, 6, 8, 10, and 12 mm. The circles, triangles, and squares represent absorber with μ_a of 0.01, 0.02, and 0.03 mm^{-1}, respectively, inserted into the phantom cavity after the white POM was inserted. The solid-, dashed-dotted-, and broken-lines represent the fitted curves of fifth-order polynomials. The order of polynomials was determined so that all the data were properly fitted without over fitting. The spatial profile of ΔOD depends on both surface-layer thickness and absorption change. Moreover, ΔOD increases with increasing S-D distance. According to the modified Beer-Lambert law (Delpy et al., 1988; Maki et al., 1995), ΔOD is approximately proportional to the mean optical-path length that a photon travels in the absorber. The mean optical path length of the absorber thus increases with increasing S-D distance, which is consistent with a study that reported the partial

path length of the inner absorber tissue (gray matter) in the human head (Fukui et al., 2003).

According to Fig. 44, however, Δ*OD* slightly decreases after reaching the maximum value. Since this decrease seemed specific to the noncontact NIRS system, the effect of stray light was examined by the Monte Carlo simulation as explained in the following section.

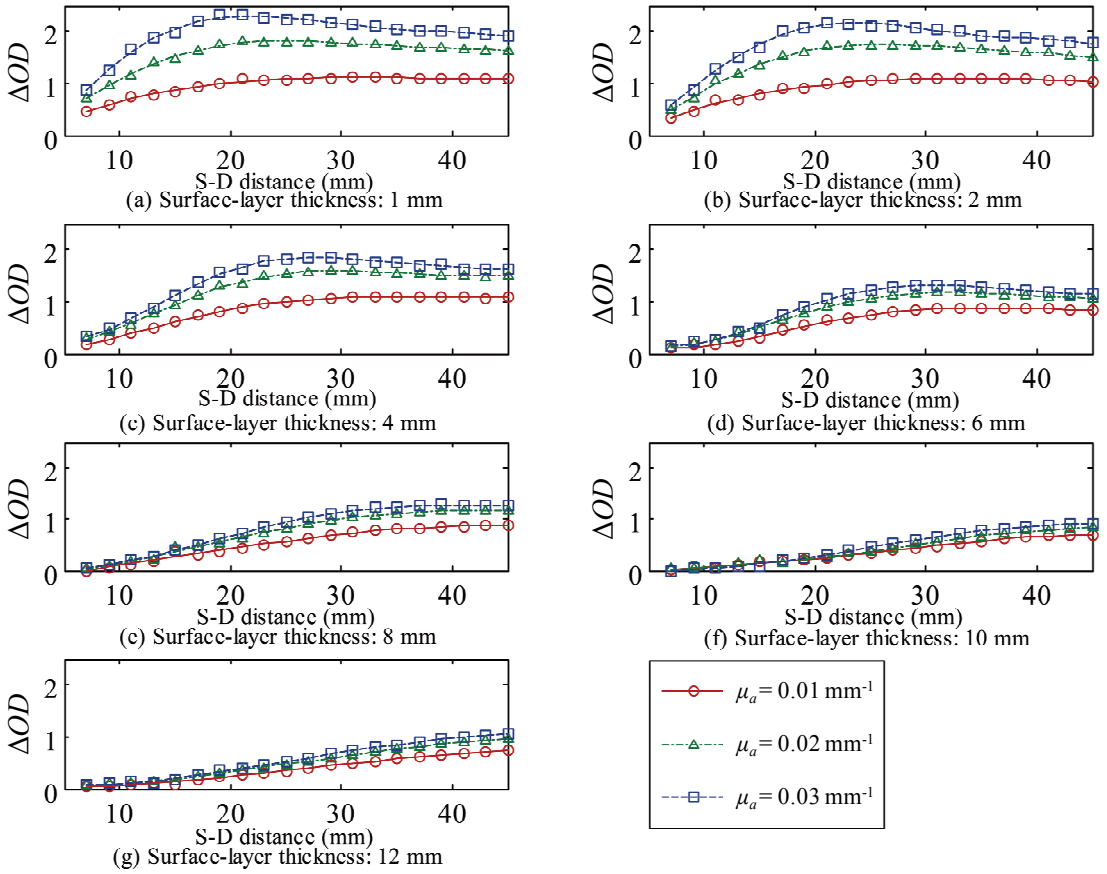

Fig. 44 S-D distance dependence of Δ*OD*.
Surface-layer thickness: (a) 1 mm, (b) 2 mm, (c) 4 mm, (d) 6 mm, (e) 8 mm, (f) 10 mm, and (g) 12 mm. The solid-, dashed-dotted-, and broken-lines represent fitted curves of fifth-order polynomials.

3.4.2. Effect of stray light

To validate the result of phantom measurements and investigate the effect of stray light, which is a potential problem specific to a noncontact optical system, the optical paths of photons propagated in the phantom were simulated by a Monte Carlo method (Okada et al., 1997). In the simulation, based on a variance-reduction technique (Hiraoka et al., 1993; van der Zee and Delpy, 1987), optical paths of the incident photons were determined from scattering coefficient only. Once the photon exited from the phantom surface, absorption was introduced by weighting each detected photon. The weight means the probability that a photon remains unabsorbed in the medium. The photons entered the phantom until the number of detected photons reached ten thousand. For each photon, the transmittance was calculated from the distribution of absorption coefficient. In the simulation, the values listed in Table 2 were used as the optical properties of the phantom. Change in optical density was calculated from the simulated intensity of detected light averaged over an appropriate number of incident photons.

Under the assumption that the stray light is constant even when the inner absorber is changed, the corrected optical density (ΔOD') (i.e., that corrected for the effect of stray light) is defined as

$$\Delta OD' = -\ln \frac{I + I_{stray}}{I_0 + I_{stray}}, \tag{17}$$

where I_{stray} represents the intensity of stray light. Since I_0, I, and I_{stray} all have positive values, the following inequality holds:

$$\left|\Delta OD\right| > \left|\Delta OD'\right|. \tag{18}$$

The detection of stray light, therefore, always causes the deterioration of sensitivity to absorbance change.

The result of Monte Carlo simulation of Δ*OD* for surface-layer thickness of 2 mm is presented in Fig. 45. Figure 45 (a) shows the result obtained under the condition that stray light was not taken into account. Figure 45 (b) shows the result obtained under the condition that stray light (the intensity ratio of stray light to incident light was 1.0×10^{-8}) was taken into account.

According to Fig. 45 (a), Δ*OD* increases to a plateau with increasing S-D distance, which is a different result to that obtained by the phantom measurement. On the other hand, Δ*OD* described in Fig. 45 (b) is similar to that obtained by phantom measurement. This result suggests that the decrease of Δ*OD* at longer S-D distance can be explained by the existence of stray light. That is, the effect of stray light becomes relatively large when the intensity of detected light is small. Therefore, when surface-layer thickness is smaller and absorption change is bigger, Δ*OD* decreases at a faster rate.

The effect of stray light can be alleviated by using more optical filters to cut out the surface-reflected excitation light. It should be noted, however, that adding optical filters inevitably lowers the signal-to-noise ratio of the detected fluorescence.

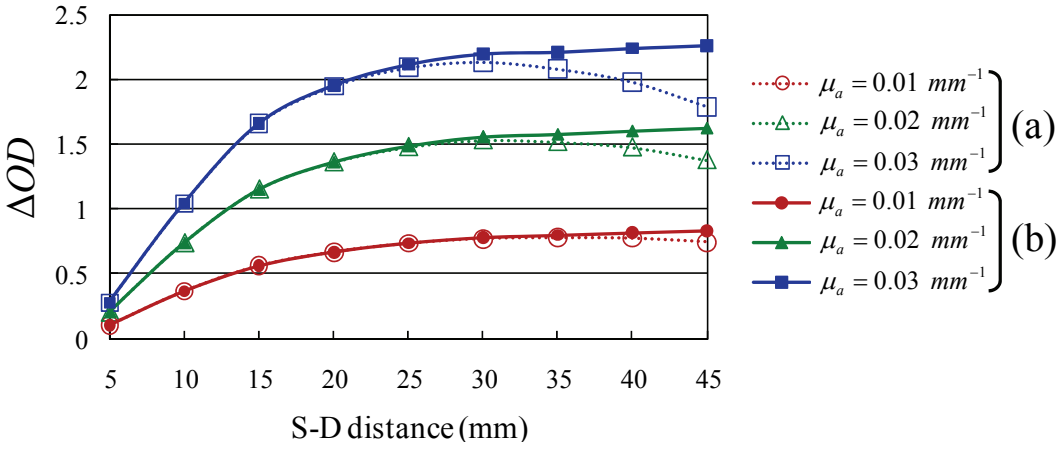

Fig. 45 Results of Monte Carlo simulation of Δ*OD* (surface-layer thickness: 2 mm). (a) Without stray-light contamination. (b) With contamination of stray light (1.0×10^{-8} times of incident light)

3.4.3. Estimation of surface-layer thickness

To investigate the dependence of S-D distance at which ΔOD becomes maximal on surface-layer thickness, the gradient of ΔOD against S-D distance ($\partial\Delta OD/\partial SD$, where SD indicates S-D distance) was calculated by differentiating the fitted curve of five-order polynomials plotted in Fig. 44 with respect to S-D distance. In the analysis, the S-D distance at which the gradients of ΔOD are equal for three absorber conditions, which is called the "isoslope point," was calculated. The isoslope point was determined as the S-D distance (set at intervals of 0.1 mm) at which the variance of $\partial\Delta OD/\partial SD$ for the three conditions was minimum under the condition of inequality, namely, $\partial^2\Delta OD/\partial SD^2 < 0$ (Note that the spatial distribution of ΔOD is convex upward.).

The gradient of ΔOD against S-D distance for surface-layer thicknesses is plotted in Fig. 46. The dotted line in each graph indicates the isoslope point, which increases as surface-layer thickness increases.

The physical meaning of the isoslope point is as follows: the slope (gradient) of ΔOD is given when ΔOD is partially differentiated with respect to SD:

$$\frac{\partial \Delta OD}{\partial SD} = \frac{\partial(\Delta \mu_a L)}{\partial SD}. \tag{19}$$

Furthermore, at the isoslope point, the partial differential of the slope with respect to $\Delta\mu_a$ should be zero because the slopes are equal under several $\Delta\mu_a$ conditions. We thus obtain

$$\frac{\partial L}{\partial SD} = 0. \tag{20}$$

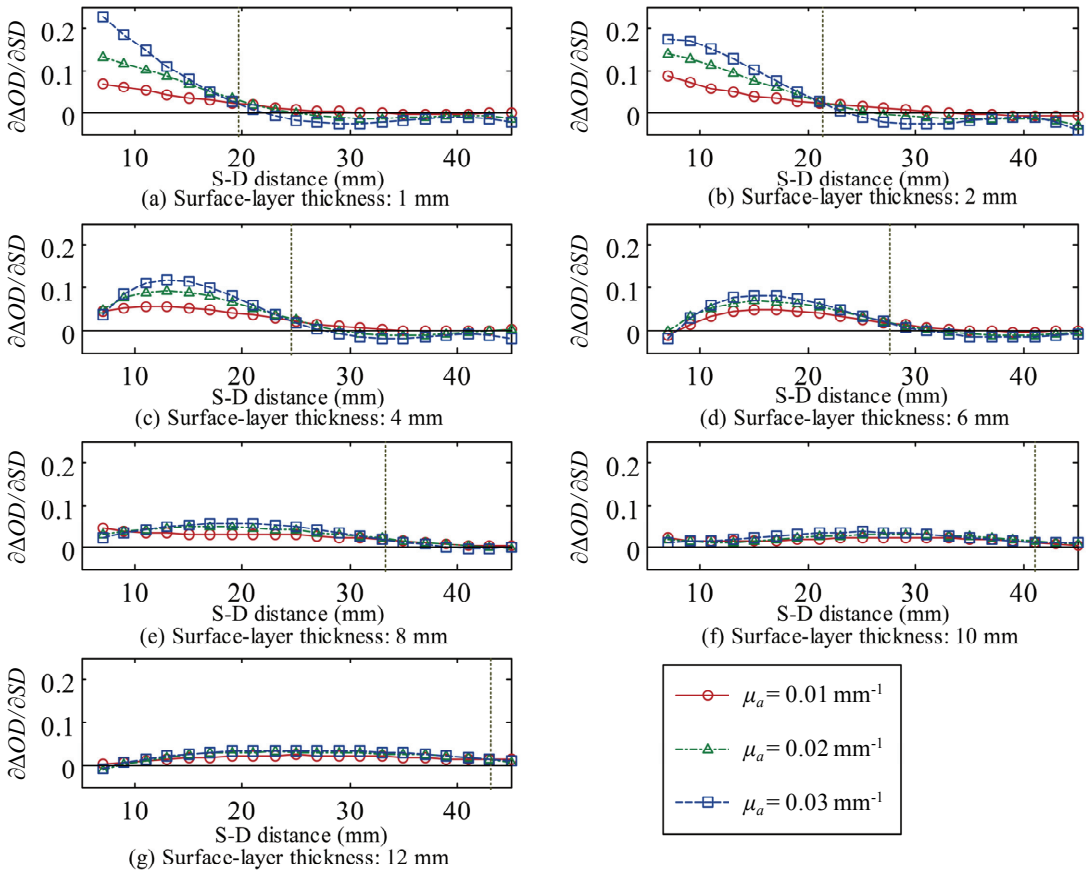

Fig. 46 Gradient of Δ*OD* against S-D distance.
Surface-layer thickness: (a) 1 mm, (b) 2 mm, (c) 4 mm, (d) 6 mm, (e) 8 mm, (f) 10 mm, and (g) 12 mm. The dotted line in each graph indicates the S-D distance at which the slope of Δ*OD* is equal for all three absorption conditions.

The isoslope point is the S-D distance where the dependency of partial optical path length in the absorber on S-D distance vanishes. This means when the S-D distance is increased, the partial optical path length in absorber converges on a certain value depending on the partial optical path length just below the focal points of irradiation and detection. There is an additional isoslope point when the partial optical path length in absorber is zero, which is caused by too short S-D distance and thick superficial layer.

The relationship between surface-layer thicknesses and isoslope points is plotted in Fig. 47. The solid line is a linear fit. According to the figure, the surface-layer thickness can be inversely estimated from the isoslope point (obtained by the

measurements under several different absorption conditions). When human tissue is measured, since the absorption coefficient of muscle tissue can be changed using an inflatable cuff, which externally halts and restarts blood flow, the isoslope point could be obtained. Furthermore, if ΔOD spatial profile calculated by a Monte Carlo simulation were available under various surface-layer thicknesses and absorption conditions, the absorption change could be more precisely estimated from both surface-layer thickness and the Monte Carlo simulation results.

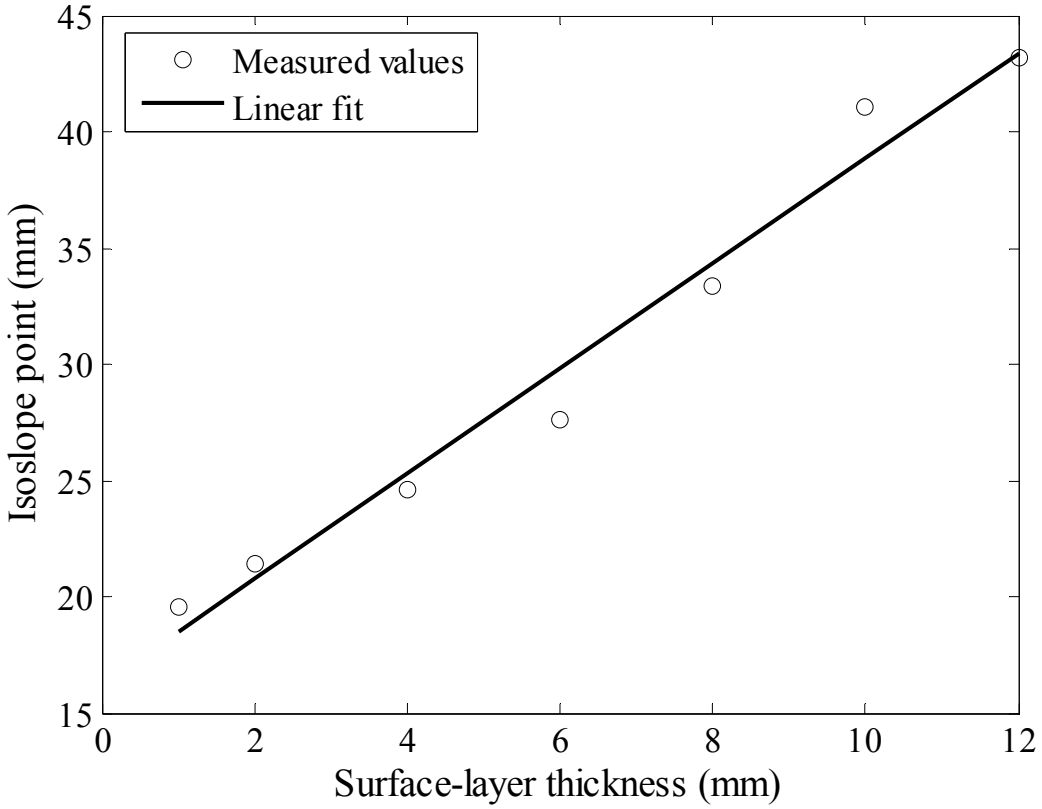

Fig. 47 Relationship between surface-layer thicknesses and isoslope points.

Chapter 4

Evaluation of surface layer effect discrimination method

4.1. Introduction

In the NIRS technique for brain-function monitoring, the scalp is irradiated with near-infrared light and the light that is propagated in and scattered from the tissue is detected at another position. Therefore, the light attenuation is influenced by the blood volume in superficial tissue. The NIR light propagates in superficial tissue even when a deep region of the tissue is of interest, and accordingly, if they are not negligible, the effects of superficial tissue on the NIRS signal should be taken into account (Germon et al., 1998; Kohri et al., 2002; Smielewski et al., 1997; Takahashi et al., 2011). Previous studies have shown that in brain measurements, the thickness of the scalp and the skull have an interference effect on the NIRS signal (Hoshi et al., 2005; Okada and Delpy, 2003). Several methods have been proposed to eliminate the effect of scalp-blood flow, systemic signal, and biological fluctuation, including using principal component analysis (PCA) (Virtanen et al., 2009; Zhang et al., 2005), independent component analysis (ICA) (Katura et al., 2008; Kohno et al., 2007), and

an inter-channel subtraction method with multiple-distance optodes (Gagnon et al., 2011; Saager and Berger, 2008; Saager et al., 2011; Tong et al., 2011; Toronov et al., 2001; Umeyama and Yamada, 2009; Yamada et al., 2009; Zhang et al., 2007a; Zhang et al., 2009; Zhang et al., 2011). The final method is often used in conjunction with static linear-regression (Saager and Berger, 2008; Saager et al., 2011; Toronov et al., 2001), adaptive filtering (Zhang et al., 2007a; Zhang et al., 2009; Zhang et al., 2011), and Kalman filtering (Gagnon et al., 2011).

ICA and PCA are the analytical methods that use continuous waveform or time-course data (patterns), and therefore it is difficult to evaluate them with a static or two-state (on or off) dynamic phantom. Instead, such signal discrimination methods are usually evaluated with simulations (Umeyama and Yamada, 2009; Yamada et al., 2009; Zhang et al., 2007a; Zhang et al., 2011). In terms of application to human measurements, the validity has been evaluated by other biological signals measured with laser Doppler flowmetry (Kohno et al., 2007), or by synchronization with task timing (Katura et al., 2008), and/or simulated hemodynamic response (Gagnon et al., 2011; Saager et al., 2011) because the correct signal from the cerebral tissue cannot be known during the actual measuring.

With a tissue-mimicking phantom (Pogue and Patterson, 2006), the correct absorption change is known because the optical properties and shape of the phantom material can be reproducibly realized (Firbank and Delpy, 1993) and can be validated with a Monte Carlo simulation based on the same model as the phantom. Clearly, using the phantom is effective for evaluating methods that eliminate and discriminate the effect of superficial tissue from that of deep tissue in NIRS signals. To evaluate such methods directly and quantitatively, a dynamic phantom with a high reproducibility and ability to make any waveform (e.g., designed time course data) of absorption is necessary. Waveforms have several properties, including frequency characteristics and correlation with other waveforms. If we use a waveform that has been created by a phantom, we can investigate the influence of waveform properties on the performance of the discriminating methods.

Some dynamic phantoms with liquid perfusion have previously been reported

(Kim and Liu, 2008; Kurth et al., 1995; Lohwasser and Soelkner, 1999). The response time of these phantoms is relatively slow, which makes it difficult to force the waveform of absorption to change in a practical period of time. Therefore, the reproducibility of the fast absorption change is hard to guarantee. The use of a dynamic phantom with an embedded liquid crystal has been proposed (Koh et al., 2009), in which the absorption at each pixel is electrically controlled. However, each pixel can be only on- or off-state (in other words, two-state control), meaning that a small absorption change in a superficial layer of the phantom cannot be achieved with this phantom.

The aim of the present study is to develop a methodology that can directly evaluate analytical methods for discriminating surface-layer effect. A tissue-simulating dynamic phantom with two absorption layers (“upper” and “lower”) was developed (Funane et al., 2012). This type of phantom only creates macroscopic absorption changes in tissue and cannot mimic the microscopic spatial variability and mechanism of hemodynamics due to vasculature. It is important to understand the limitation of the applicability of the phantom and that the experimental results of the phantom cannot be easily generalized. However, the phantom is very useful and indeed essential for industrial applications such as the performance testing of NIRS instruments. Its key feature is that the effective absorption coefficient can be adjusted by changing the position of the absorber. The waveform of absorption change can be reproducibly simulated by two one-axis stage-driven absorbers within a very short period of time. Table 6 shows a comparison of NIRS dynamic phantom.

Using a multi-distance NIRS system (Funane et al., 2011c), we measured the optical density change of the phantom at multiple source-detector (S-D) distances and investigated the performance of a subtraction method with a short-distance regressor. In addition, when the absorption coefficients of two layers were changed, we extracted the signal of each layer by independent component analysis and investigated the dependence of the weight of each component on the S-D distance.

4.2. Design of dynamic phantom

4.2.1. Material and structure of phantom

We used reports by Fukui et al. (2003) and Wang et al. (2010) to set the absorption coefficient (μ_a) and reduced scattering coefficient (μ'_s) values of the scalp and skull and the gray matter of a human adult head to the range of 0.012–0.036 and 0.73–2.3 mm^{-1}, respectively. In this study, the μ_a and μ'_s values of the two layers of absorber were chosen from around this range. A white polyoxymethylene (POM) was used as the base material of the phantom because it has a comparable μ'_s value (0.9 mm^{-1}) to biological tissue and is commercially available and easily worked, although it does not absorb light very much (μ_a = 0.002 mm^{-1}). Three absorber materials with μ_a values of 0.01, 0.02, and 0.03 mm^{-1} were thus prepared. The μ'_s value of the absorbers was 0.9 mm^{-1} to match that of the POM. The absorbers were made by mixing an epoxy resin (MY753, Aeropia Chemical Supplies) and a hardener (XD716, Aeropia Chemical Supplies) at a 3:1 weight ratio (Firbank et al., 1995). An infrared dye, Projet 830 (Avecia Ltd.), and titanium dioxide (SuperWhite, Alec Tiranti Ltd.) were mixed into the absorber materials to control the absorption coefficient and the reduced scattering coefficient of the absorbers, respectively.

Using these materials, a phantom with two absorber layers (upper and lower) in low-absorption and high-scattering base material was developed. The phantom size was 100 × 120 (horizontal) × 60 (vertical) mm. The absorbers (75×60×5 mm) were held by absorber-holing frames (made of white POM) and were inserted into two cavities (100 × 70 × 5 mm) at depths of 2–7 mm and 12–17 mm. The hexagon socket set screw was used to attach the absorber to the absorber-holding frames. These frames, along with an overall view of the developed dynamic phantom, are shown in Fig. 48. One absorber-holding frame was attached to each automatic stage with an aluminum spacer between the aluminum frame and the stage.

Table 6　Comparison of NIRS dynamic phantom.

References	Our study	Lohwasser and Soelkner, 1999	Koh et al., 2009	Kurth et al., 1995	Kim and Liu, 2008
Main objective	Evaluation of discrimination method between superficial and deep layer signals	Laser Doppler flowmetry of capillary blood flow	Evaluation of NIRS instrument	Evaluation of NIRS instrument	Oxygenation dynamics in tumor blood vessel
Method	Absorber plate is driven by automatic stages.	Diluted milk is perfused in narrow ducts in epoxy resin.	Size and shape of attenuator region is changed by LCD.	Blood is perfused in phantom brain mixed with O_2, N_2, and CO_2.	Ink is injected to helical tube by syringe pumps.
Response time	○	×	○	×	×
Reproducibility	○	△	○	△	△
Advantage	Fast response, high reproducibility, and ability to generate any waveform.	Capillary simulation.	Fast response, high reproducibility, and ability to generate any spatial distribution.	Fluid, realistic blood oxygenation simulation.	Ability to generate ink flow in separate two regions.
Disadvantage	Disability to generate localized absorption change.	Only flow velocity can be controlled.	Two state control.	Slow response and low reproducibility.	Slow response.

○: good, △: moderate, ×: bad

In our phantom model, to uphold the assumption that an absorber's position change in a layer region is equivalent to a homogeneous μ_a change in the corresponding layer region, the thickness of each absorber (and absorber-holding frame) should be sufficiently larger than photon-transport length scales (approx. $1/\mu'_s$). The depth (12 mm) and thickness (5 mm) of the lower layer was chosen from around the values of reported scalp-cortex distance (12–18 mm) and thickness of gray matter (4 mm) (Haeussinger et al., 2011; Okada and Delpy, 2003a). The thickness of the upper layer (5 mm) was also chosen from the reported value of scalp thickness

(3.0–7.1 mm) (Haeussinger et al., 2011; Okada and Delpy, 2003a). The upper layer simulating scalp should be as shallow as possible, but we put a 2-mm-thick superficial layer (scatterer) over the upper layer to strengthen the structure of the phantom. In this way, we determined the depth and thickness of each layer not simply based on anatomical considerations but also on the design of a phantom for industrial purposes.

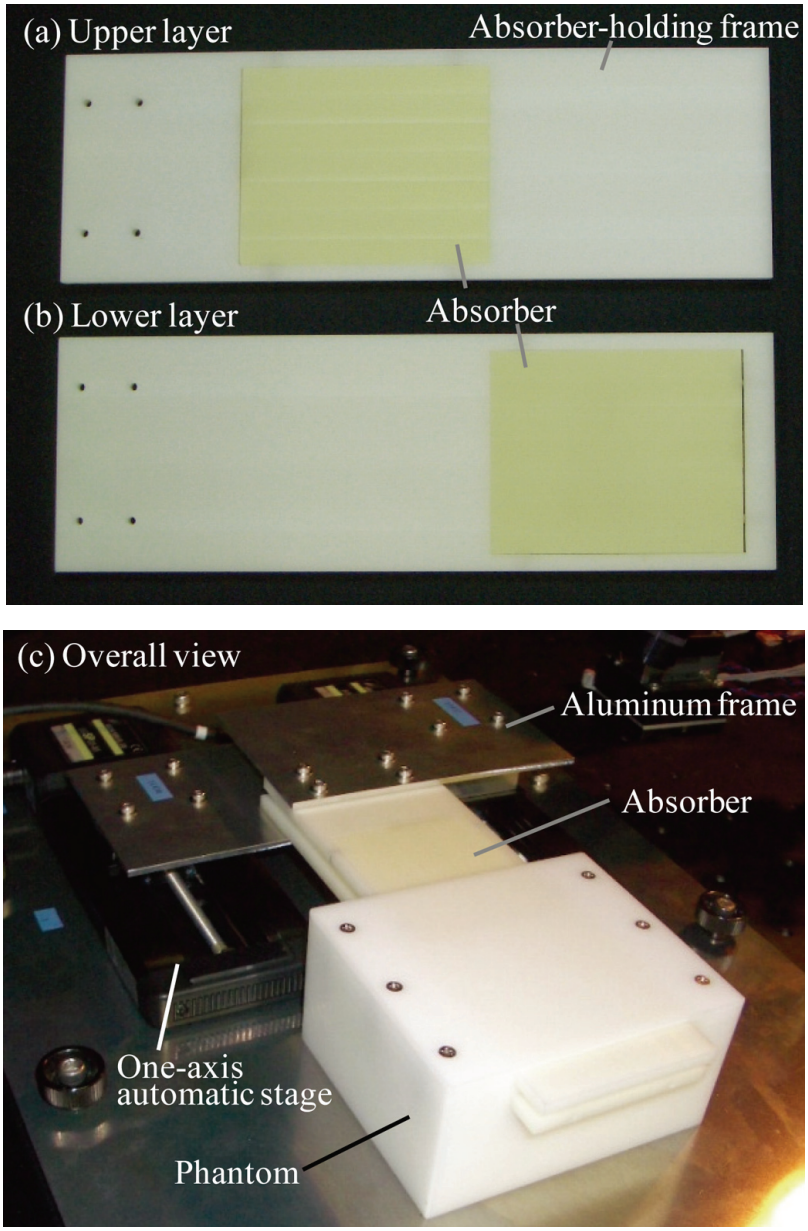

Fig. 48 Photographs of the developed phantom. (a) Upper layer and (b) lower layer of absorber-holding frame. (c) Overall view of dynamic phantom.

4.2.2. Driving mechanism of absorbers

To dynamically change the position of absorbers in the phantom, two layers of absorbers were held in place by absorber-holding frames using two one-axis automatic stages (SGSP20-85, Sigma Koki Co., Ltd.). The stage and absorber-holding frame was connected to an aluminum frame. The two stages were controlled by a PC that transmitted commands to the stage controller via RS232C. Each absorber-holding frame was thus independently controlled by a corresponding one-axis automatic stage.

The automatic stages and the phantom were attached to an aluminum bottom plate. The structure of the phantom and the driving mechanism is shown in Fig. 49. Figure 49 (a) shows a top view of the phantom showing one source point, the phosphor detector point, an outline of the "banana" width of the photon spatial distribution, and one of the absorber slabs (superimposed). Figure 49 (b) shows a front view of the phantom. Each absorber-holding frame is independently controlled by a corresponding one-axis automatic stage.

Two absorbers were placed on the opposite side from the center line (scanning line) so that sensitivity to the absorption change of each layer would not be much influenced by the absorption change of another layer. The opposite-side placement minimizes the number of photons that propagates in both absorbers, whereas same-side placement maximizes it. Therefore, the opposite-side placement of absorbers minimizes any interaction effects between two absorbers that could lead to non-linearity between the position and the ΔOD.

The target position was converted to the stroke in stage coordinate value and sent as a command from the PC to the stage controller. The origin and positive or negative direction of the position coordinate axes were set so that the partial optical path length in the absorber was increased (i.e., the optical density was increased) when the stage position was positive in the defined coordinate axis (hereafter, "x" used for the place coordinates for both layers). Therefore, the directions of the position coordinates for the upper and lower layers were set to be opposite. Optical density change (i.e., effective $\Delta\mu_a$) was controlled by the partial effective path length in absorbers that was

determined by the stage-position change (Δx), not by the $\Delta\mu_a$ of the absorber.

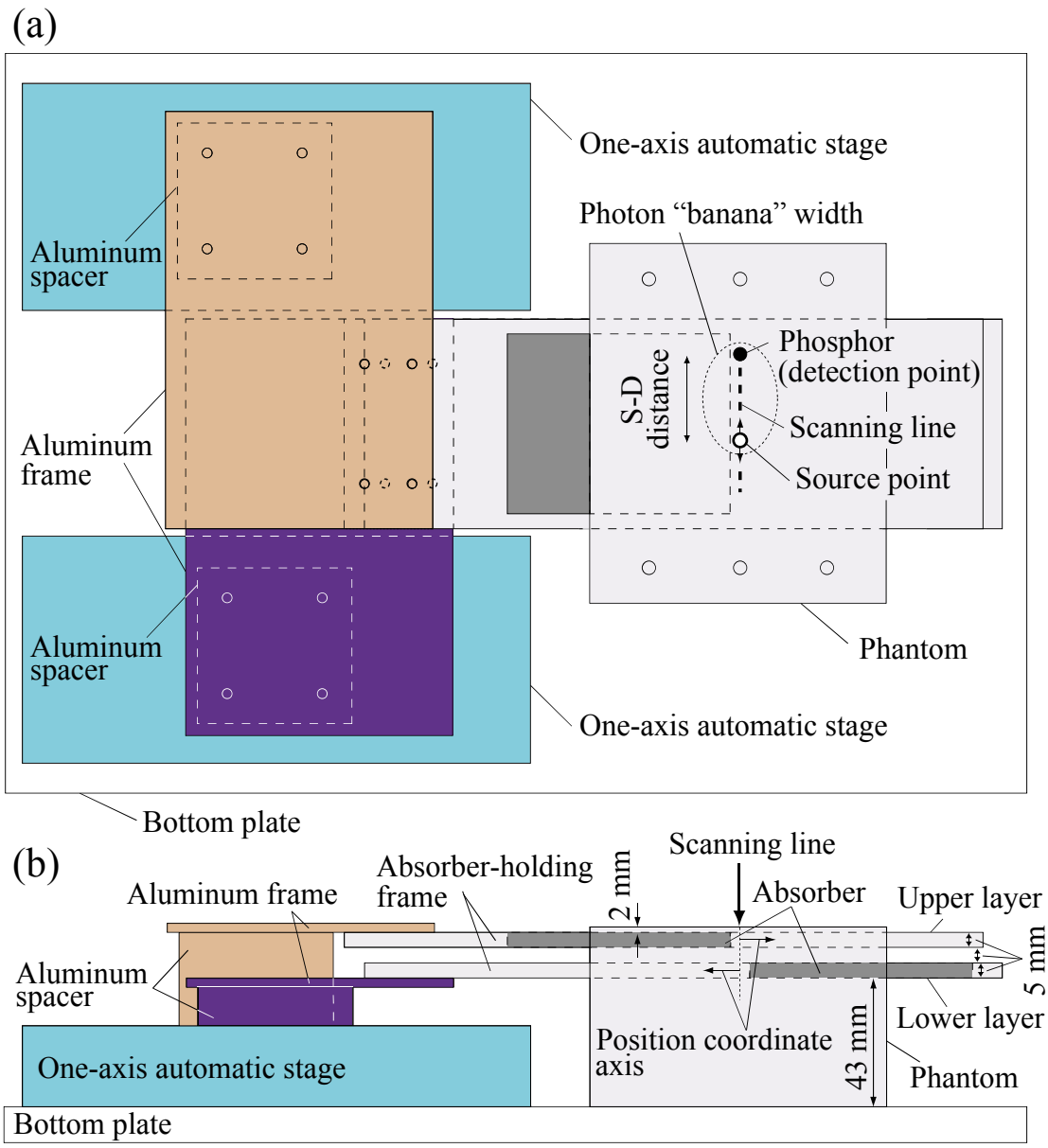

Fig. 49 Structure of phantom and driving mechanism of absorbers. (a) Top view. (b) Front view. Each absorber-holding frame is independently controlled by a corresponding one-axis automatic stage.

4.3. Measurement system

To test the dynamic phantom developed in this study, we used a multi-distance NIRS system with a noncontact light source (an 808-nm laser diode) and detector that effectively measures the optical density of the biological tissue at multiple S-D separations (Funane et al., 2011c). To make it possible to measure the absorption change of tissue with a noncontact light emitter and detector, the wavelength of the tissue-propagated light was converted by a near-infrared phosphor on the surface of tissue and the excitation light was cut by optical filters; consequently, only fluorescence was detected and discriminated with lock-in detection, whereas any backscattered stray light was suppressed (Funane et al., 2010; Funane et al., 2011c). Phosphor [$Li(Nd_{0.9}Yb_{0.1})P_4O_{12}$], which was enclosed and bonded in a cell consisting of an aluminum ring and an InP wafer, was placed on a fixed detection focal point.

A photograph of the dynamic phantom and optical scanning system is shown in Fig. 50. A block diagram of the multi-distance NIRS system and stage controller for the phantom is shown in Fig. 51. The laser diode was driven by a laser driver (ALP-7033CB, Asahi Data Systems, Japan) that receives the analog signal of a function generator (model 1930A, NF, Japan). The frequency of intensity modulation was set to 3.3 kHz. The function generator was controlled via a GPIB controller (GPIB-USB-HS, National Instruments, U.S.A.) with a desktop PC, which meant we could adjust the irradiation power of the laser diode in accordance with the S-D distance. A galvano scanner (controller: GC-201; motor: GM-1010; Canon, Japan) was controlled via RS232C with the desktop PC.

The fluorescence emitted from the phosphor and caught by the APD is amplified by a trans-impedance amplifier in an APD module, and after that the amplified fluorescence signal is detected by a lock-in amplifier (model 5207, EG&G, U.S.A.), the output of which is converted to a digital signal by an analog-digital converter (NR-2000, Keyence, Japan) and saved in a laptop PC via USB. An analog marker signal was input into the analog-digital converter from the laptop PC.

The galvano scanner was set to irradiate ten points on the phantom surface, where

S-D distances were set to 5.5–41.5 mm with a 4-mm interval for each. The duration of the measurement of each point was 1 s including switching time of the measurement point and irradiation power.

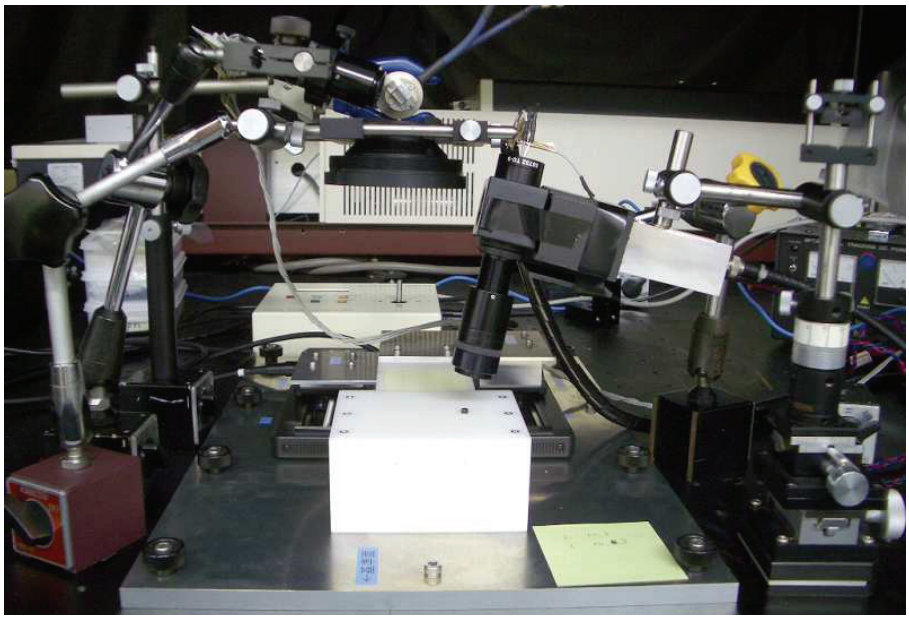

Fig. 50 Dynamic phantom and optical scanning system.

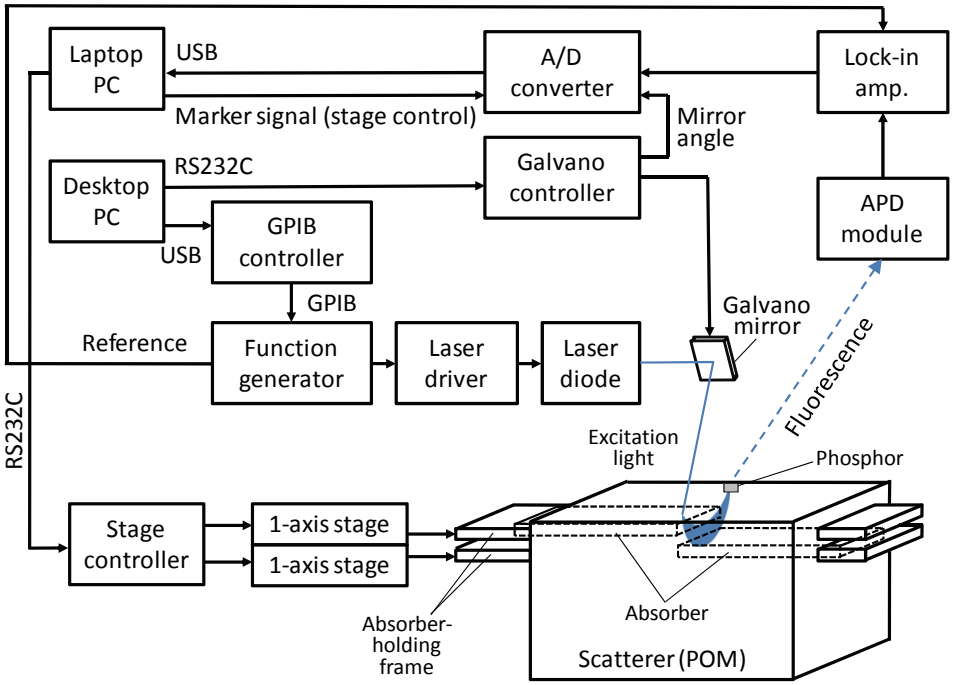

Fig. 51 Block diagram of multi-distance NIRS system and stage controller for phantom. Two one-axis stages are independently driven by a stage controller that is commanded by a laptop PC through RS232C.

4.4. Calibration of dynamic phantom

4.4.1. Calibration method

A calibration curve of the relationship between the stage position and changes in optical density (ΔOD) is necessary in order to use the phantom for NIRS measurement. To calibrate the phantom, its ΔOD was measured as the inserted absorber at either of the upper or lower layers driven by a one-axis automatic stage. The layer that is not driven is replaced by base material (white POM) by setting the stage positions to x = –37 and –43 mm for the upper and lower layers, respectively. ΔOD was calculated by

$$\Delta OD = -\ln \frac{I}{I_0}, \tag{21}$$

where I_0 denotes the baseline intensity of detected light that is obtained when the stage position is x = –30 mm. I denotes the intensity of detected light at each stage position. The absorption coefficients of the upper and lower layers are 0.01 and 0.03 mm^{-1}, respectively.

4.4.2. Relationship between stage position and ΔOD

To ensure a linear relationship between the stage-position change (Δx) and ΔOD for both layers and to minimize the interaction effect between two absorber layers, the absorption coefficient of the upper layer should be smaller. Furthermore, in terms of phantom design, to make the ΔOD values at a typical S-D distance (for example, 29.5 mm) caused by the movements of two absorber layers as equal as possible, the absorption coefficient of the lower layer should be higher than that of the upper layer. Among all combinations of μ_a values, we selected 0.01 and 0.03 mm^{-1} for the upper and lower layers, respectively.

The relationship between stage position (the coordinates of which are defined in section 4.2.2) and ΔOD for ten different S-D distances is shown in Fig. 52. Figure 52

describes Δ*OD* when only upper absorber ((a) μ_a : 0.01 mm^{-1}; (b) μ_a : 0.02 mm^{-1}; (c) μ_a : 0.03 mm^{-1}) or only lower absorber ((d) μ_a : 0.01 mm^{-1}; (e) μ_a : 0.02 mm^{-1}; (f) μ_a : 0.03 mm^{-1}) was driven. Baselines of Δ*OD* that was measured when the both layers were switched to white POM were shifted to zero in the figures. In Fig. 52 (a), the inflection point of Δ*OD* is deviated to the minus side because the photon distribution is changed due to the movement of the upper-layer absorber. In contrast, the deviation from the center line of the inflection point of Δ*OD* for the lower layer is relatively smaller than that for the upper layer because the ratio of partial effective path length in the lower absorber to total path length is smaller than that in the upper absorber, and the influence of stage position on the photon distribution in the phantom is relatively small.

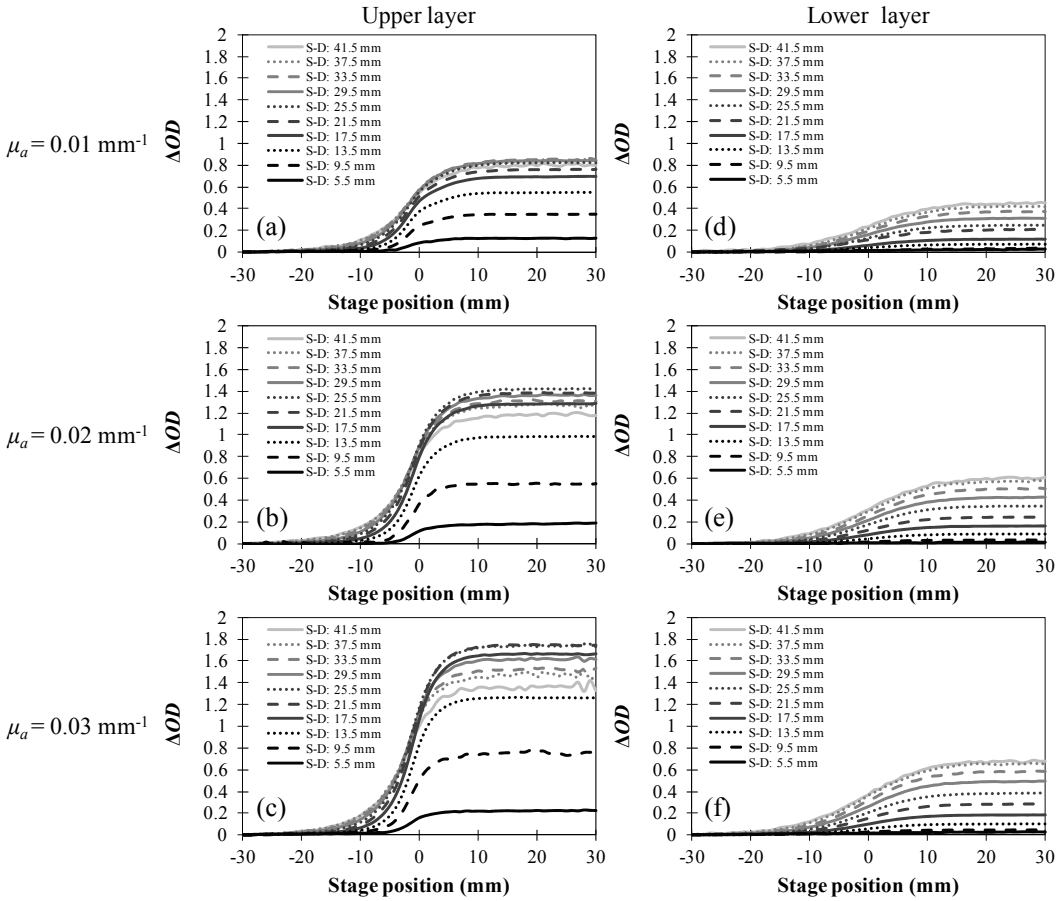

Fig. 52 Calibration results.
Relationship between stage position and Δ*OD* for ten conditions of S-D distance when only upper absorber ((a) μ_a : 0.01 mm^{-1}; (b) μ_a : 0.02 mm^{-1}; (c) μ_a : 0.03 mm^{-1}) or only lower absorber ((d) μ_a : 0.01 mm^{-1}; (e) μ_a : 0.02 mm^{-1}; (f) μ_a : 0.03 mm^{-1}) was driven. Baselines of Δ*OD* that was measured when the both layers were switched to white POM were shifted to zero in the figures.

Moreover, in all conditions (a)–(f), the initial rise of Δ*OD* while increasing the stage position from x = –30 mm is earlier for the longer S-D distance because the spatial distribution of photons in the phantom is larger for the longer S-D distance probe and the probe is sensitive to the absorber that is further from the center line (x = 0 in the position coordinate).

To quantify the deviation of the inflection point of Δ*OD* from the center point, we calculated the gradient of Δ*OD*. The relationship between the stage position and the stage-axial spatial gradient of the Δ*OD* [$\partial(\Delta OD)/\partial x$] at each S-D distance is shown in Fig. 53.

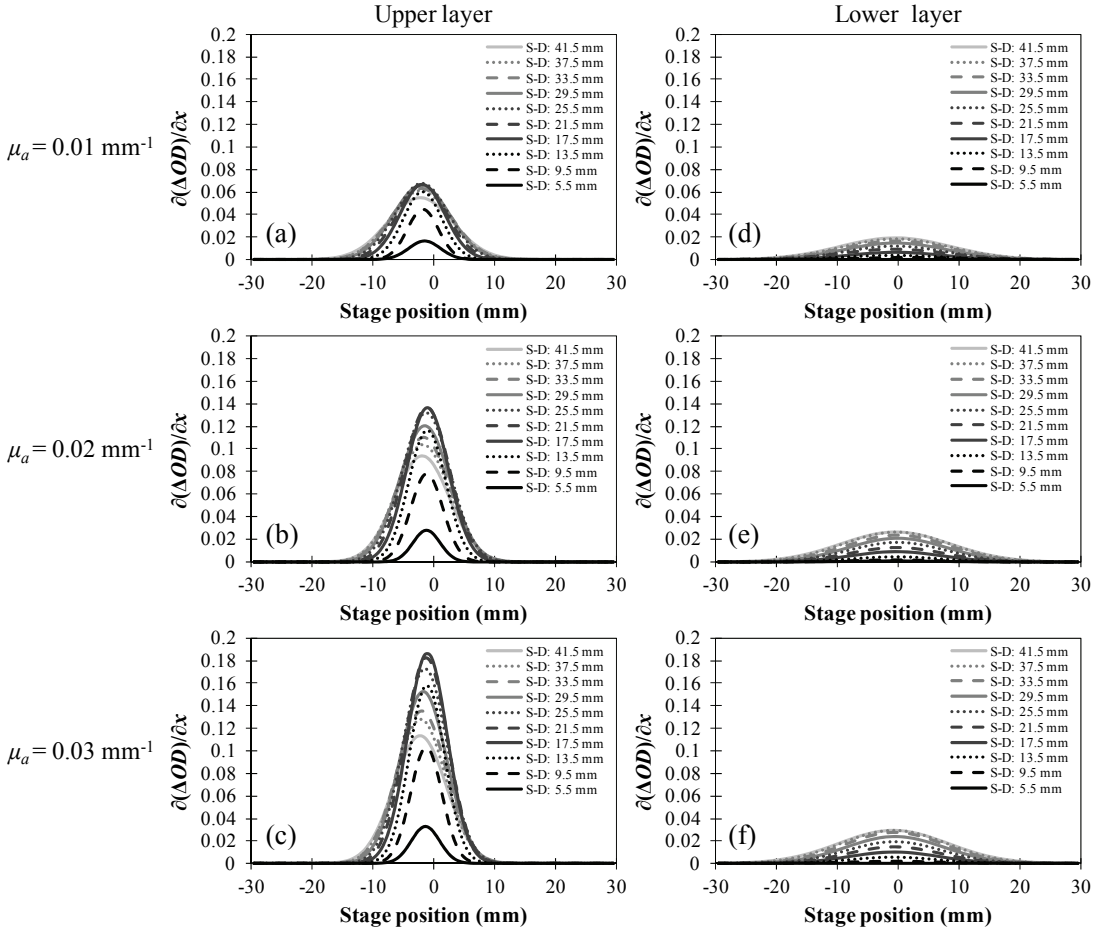

Fig. 53 Calibration results.
Relationship between stage position and gradient of Δ*OD* for ten conditions of S-D distance when only upper absorber ((a) μ_a : 0.01 mm^{-1}; (b) μ_a : 0.02 mm^{-1}; (c) μ_a : 0.03 mm^{-1}) or only lower absorber ((d) μ_a : 0.01 mm^{-1}; (e) μ_a : 0.02 mm^{-1}; (f) μ_a : 0.03 mm^{-1}) was driven. The Gaussian curves fitted to the Δ*OD* gradient of the measurement data are shown.

Figure 53 describes $\partial(\Delta OD)/\partial x$ changes when only upper absorber ((a) μ_a : 0.01 mm^{-1}; (b) μ_a : 0.02 mm^{-1}; (c) μ_a : 0.03 mm^{-1}) or only lower absorber ((d) μ_a : 0.01 mm^{-1}; (e) μ_a : 0.02 mm^{-1}; (f) μ_a : 0.03 mm^{-1}) was driven. The Gaussian curves fitted to the ΔOD gradient of the measurement data are shown in the figures.

The following analysis was done assuming that μ_a of upper and lower layers were 0.01 and 0.03 mm^{-1}, respectively. The mean stage positions at the maximal ΔOD gradient were x = –1.9 mm (upper layer) and x = –0.7 mm (lower layer). The mean values and standard deviations of full width at half maximum (FWHM) of the ΔOD gradient were 9.4 ± 2.3 mm (upper layer) and 19 ± 1.5 mm (lower layer). The minimum FWHM values were 6.0 mm at 9.5-mm S-D distance and 16.8 mm at 13.5-mm S-D distance for the upper and lower layers, respectively. The ΔOD gradient at the 5.5-mm S-D distance was not used to calculate the mean position or FWHM for the lower layer because the ΔOD gradient was almost equal to zero.

To proportionally change the ΔOD by the change of the stage position, the stage should be driven within the range where the spatial slope of ΔOD is constant. When an approximate-linearity of the relationship between changes in stage position and ΔOD was defined as the stage positions where the change in ΔOD gradient is within 10% from the maximum (at the inflection point), the calculated ranges were x = –1.9 ± 1.8 and x = –0.7 ± 3.6 mm for the upper and lower layers, respectively. The ranges were calculated by using the mean FWHM values of the ΔOD gradient as representative values. The waveform of ΔOD was approximately the same as that of the stage position when the stages were driven within the range; therefore, the ΔOD change profile can be easily designed. The waveforms of the driving stages used for the following experiments were designed so that the stage positions were all within the above range.

4.4.3. Comparison with results by Monte Carlo simulation

To investigate the consistency between the developed phantom and a simulation model where the same μ_a and μ_s' were assumed, ΔOD measured while each layer

region was switched from uniform POM to uniform absorber (ΔOD_{sw}) was compared with the linear-fitted partial effective path length (L_{eff}) of photons calculated by a three-dimensional Monte Carlo simulation (Hiraoka et al., 1993; Okada et al., 1997; van der Zee and Delpy, 1987) in the following way.

From experiments, ΔOD_{sw} was obtained by the ΔOD measured at the 30-mm position where each layer region underneath the measurement optodes was switched from uniform POM to uniform absorber , while another layer was uniform POM. Monte Carlo simulation was used to calculate the L_{eff}^{upper} and L_{eff}^{lower} values by using absorption coefficients (μ_a^{upper} , μ_a^{lower}) = (0.01, 0.002) and (0.002, 0.03) (mm^{-1}), respectively. When the change in the product of absorption coefficient and partial effective path length is assumed to be equal to ΔOD (Hiraoka et al., 1993), ΔOD is expressed as

$$\Delta OD = \Delta(\mu_a^{upper} \times L_{eff}^{upper}) + \Delta(\mu_a^{lower} \times L_{eff}^{lower}), \tag{22}$$

where L_{eff}^{upper} and L_{eff}^{lower} represent partial effective path lengths for the upper and lower layers, respectively. The L_{eff} values at 5-, 10-, 15-, 20-, 25-, 30-, 35-, 40-, and 45-mm S-D distances calculated by Monte Carlo simulation were interpolated to values at 5.5-, 9.5-, 13.5-, 17.5-, 21.5-, 25.5-, 29.5-, 33.5-, 37.5-, and 41.5-mm S-D distances by a spline function. Next, the spline function was fitted to the measured ΔOD_{sw} by a least-square method and a single scaling factor that provided the best overall fit (which we call "computed ΔOD") to the experimental ΔOD_{sw} for each layer was obtained. Furthermore, to quantitate the performance of a regression method, we defined and calculated the "ratio of ΔOD ($R_{\Delta OD}$)" between the upper and lower layers, expressed as

$$R_{\Delta OD} = \frac{\Delta OD^{upper}}{\Delta OD^{lower}}, \tag{23}$$

where computed ΔOD values were used.

The data obtained at the longest S-D distance (41.5 mm) was not used for the fitting because of a low signal-to-noise ratio. The obtained scaling factors were 0.010 and 0.023 mm^{-1} for upper- and lower-layer L_{eff}, respectively. The experimental ΔOD_{sw}, the computed ΔOD (linear fit of the simulated L_{eff}) of each layer, and the ratio of ΔOD at each S-D distance are plotted in Fig. 54 (a). The goodness of fit between the experimental and computed ΔOD was tested using the chi-square test. Results showed that the validity of the model (spline function from computed L_{eff}), including S-D distance dependency of ΔOD for each layer, was warranted (reduced chi-square: χ^2 = 0.0003 (upper), 0.017 (lower) < 1). According to Eq. (22), when L_{eff} values are constant and the $\Delta\mu_a$ of either the upper or lower layer is equal to zero, the obtained scaling factor should be comparable to $\Delta\mu_a$. The scaling factors for the upper and lower layers are therefore expected to be 0.008 (0.010 – 0.002) and 0.028 (0.030 – 0.002) mm^{-1}, respectively, which are the values of the assumed absorption-coefficient changes. The differences between the scaling factor and acual experimental $\Delta\mu_a$ were 20 and 22%.

The L_{eff} values computed by Monte Carlo simulation and the experimental L_{eff} values (= ΔOD_{sw} / $\Delta\mu_a$) are shown in Fig. 54 (b). Experimental L_{eff} values were calculated using expected $\Delta\mu_a$ values. The differences between the L_{eff} values from the measurement and the simulation were, on average, 19.0 and 9.4% (L_{eff} at a S-D distance of 5.5 mm for the lower layer was not used because the L_{eff} from the simulation was almost equal to zero, so the error was 240%). The difference of the values between experiment and simulation could have been caused by 1) an inaccurate measurement of the absorber's optical properties, 2) the difference between the photon distributions (and subsequent L_{eff} change) under the condition when the lower layer was filled with absorber and the condition when it was not, or 3) measurement noise during the experiments.

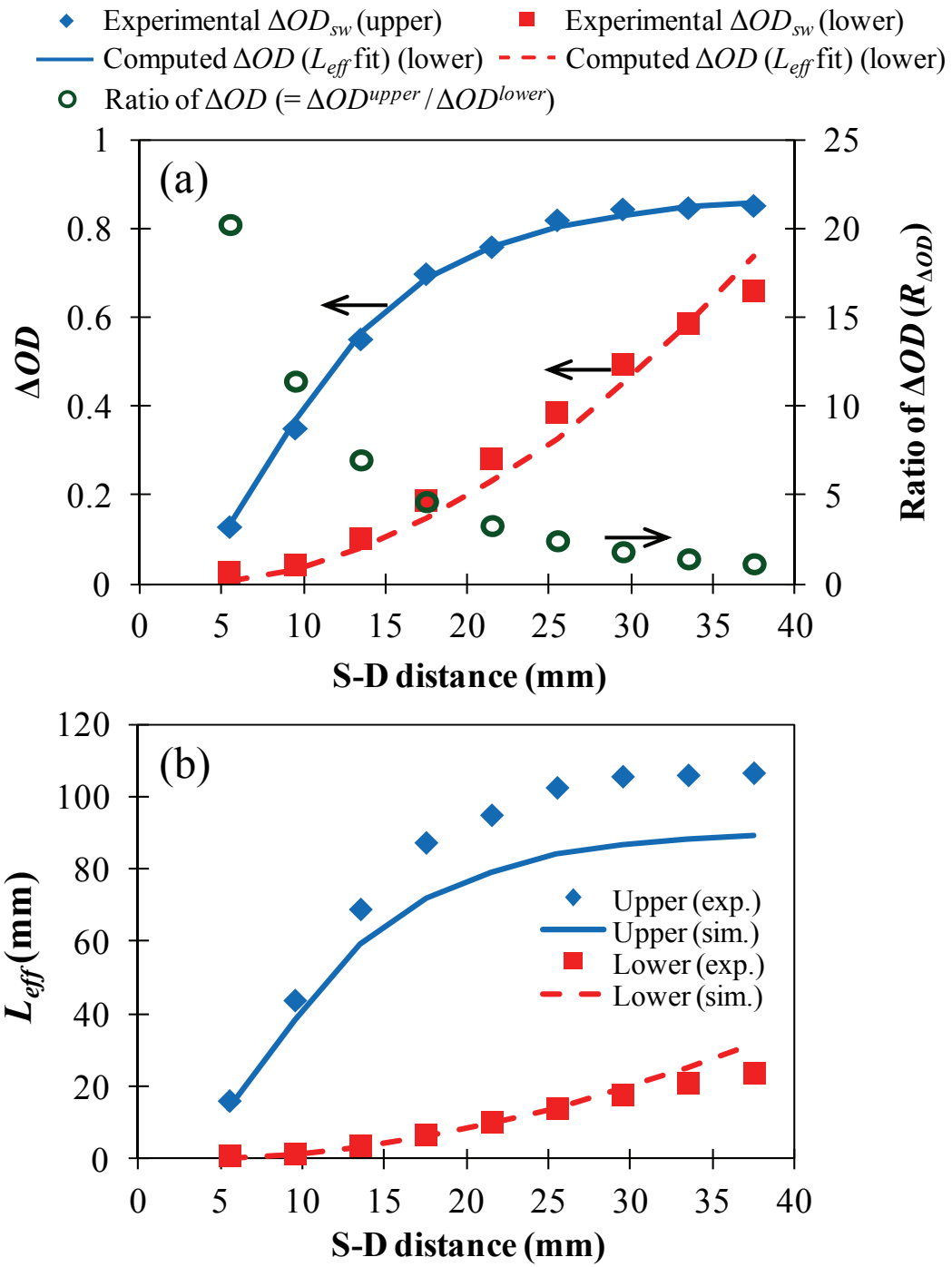

Fig. 54 (a) Experimental ΔOD_{sw}, the computed ΔOD (linear fit of the simulated L_{eff}) of each layer, and the ratio of ΔOD ($R_{\Delta OD}$) at each S-D distance. (b) Experimental (exp.) and simulated (sim.) L_{eff} of upper and lower layers.

Experimental L_{eff} was calculated using ΔOD_{sw} and $\Delta\mu_a$. When ΔOD_{sw} was measured, absorption coefficients of upper and lower layers were changed from 0.002 to 0.01 mm^{-1} and from 0.002 to 0.03 mm^{-1}, respectively. In the Monte Carlo simulation, absorption coefficients of the upper and lower layers were set to 0.01 and 0.03 mm^{-1}, respectively.

4.5. Evaluation of multi-distance analytical methods by dynamic phantom

4.5.1. Synthesis of waveforms

We used the phantom to evaluate the multi-distance analytical methods for discriminating the effects of superficial tissue in the following way. The waveform of the absorption change at each layer can be easily reproduced by controlling the 1-axis stage with digital-base commands. While the upper and lower layers were driven under the following two conditions, ΔOD was measured by the multi-distance NIRS system described in section 4.3. Measurements were also conducted while only one layer was driven under the two conditions.

Under condition 1, the stage position of the upper layer was driven so as to simulate white noise while the stage position of the lower layer was driven so as to simulate a change in cerebral blood volume (CBV) (Buxton et al., 2004) evoked by neural activation. Under condition 2, the stage position of the upper layer was driven so as to simulate a biological fluctuation (Fox et al., 2007; Toronov et al., 2000) while the stage position of the lower layer was driven so as to simulate a change in CBV response. All three simulated waveforms could be obtained with the *in vivo* NIRS measurement.

Three types of time course data, along with the power spectral densities of the stage-position changes, are shown in Fig. 55: (a) white noise, (b) biological fluctuation, and (c) CBV response. The time course data were normalized to zero-mean and unit-variance data when the power spectrum densities were calculated. Power spectral densities were calculated on the assumption that one point of time course data is equivalent to one second. At frequencies lower than 0.1 Hz, the waveforms in (b) and (c) commonly contain larger power compared to that at higher frequencies. These two waveforms cannot thus be discriminated with frequency selective filtering. The correlation coefficients between the waveforms in (a) and (c) and those in (b) and (c) were 0.015 and –0.190, respectively.

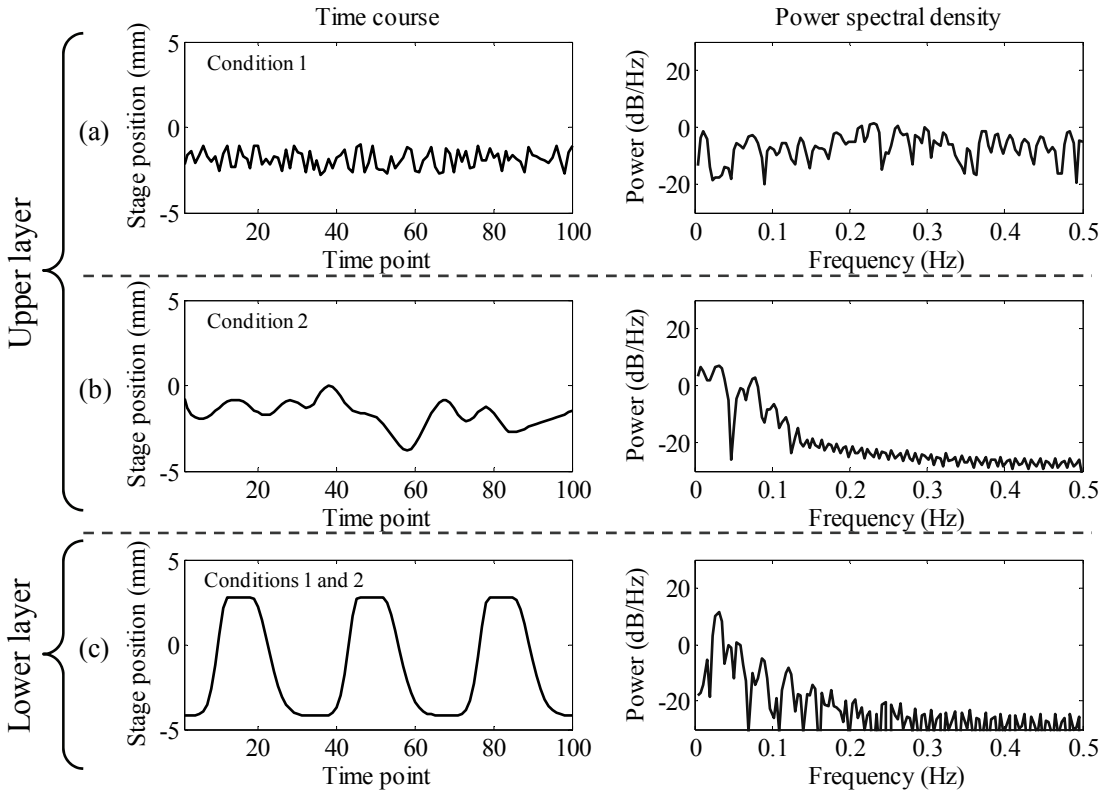

Fig. 55 Time course and power spectrum density (PSD) of stage-position change simulating NIRS signal when one point of time course data was equivalent to one second: (a) white noise, (b) biological fluctuation, and (c) cerebral blood volume (CBV) response evoked by neuronal activation.

4.5.2. Extraction of deep-layer signal with subtraction method

Using our dynamic phantom, the performance of a subtraction method with short-separation regression (Saager and Berger, 2008; Saager et al., 2011; Toronov et al., 2001), which extracts the deep absorption change from a signal that is contaminated by the absorption change of the surface layer, was investigated while both absorbers of the upper and lower layers were independently driven. In the subtraction method, the signal from a short S-D distance channel (ex. ΔOD_{short}) was linearly fitted to that from a long-distance channel (ex. ΔOD_{long}). The fitting calculation is conducted by minimizing the square sum of differences between ΔOD_{long} and scaled ΔOD_{short} time series. The signal originated from deep region (ex. ΔOD_{deep}) is obtained by calculating Eq.(24).

$$\Delta OD_{deep} = \Delta OD_{long} - (k_1 \Delta OD_{short} + k_2), \tag{24}$$

where k_1 and k_2 denote fitting parameters (scaling factors).

In the present study, we compare the result from the method with the correct waveform that was obtained while only the lower layer was driven. Performance was defined as the amplitude ratio of the subtraction result to actual lower layer change (target).

When the subtraction method is used, lower-layer signal amplitude at a longer S-D distance (ΔOD_{SD1}^{lower}) is also subtracted by a lower-layer signal that is included in the shorter S-D distance signal (regressor channel) (ΔOD_{SD2}^{lower}), where the scaling factor (k_1 in Eq. (24)) here is the ratio of the upper-layer ΔOD of longer S-D distance to shorter S-D distance ($\Delta OD_{SD1}^{upper} / \Delta OD_{SD2}^{upper}$) because subtraction is performed so as to eliminate the upper-layer signal (k_2 in Eq. (24) is theoretically equal to zero). If the performance of the subtraction method is defined as the amplitude ratio (AR) of the subtraction result to only the lower-layer change (target), AR can be expressed as

$$AR = \left(\Delta OD_{SD1}^{lower} - \frac{\Delta OD_{SD1}^{upper}}{\Delta OD_{SD2}^{upper}} \times \Delta OD_{SD2}^{lower} \right) / \Delta OD_{SD1}^{lower} = 1 - \frac{\Delta OD_{SD1}^{upper}}{\Delta OD_{SD1}^{lower}} \times \frac{\Delta OD_{SD2}^{lower}}{\Delta OD_{SD2}^{upper}} \tag{25}$$

$$= 1 - \frac{R_{\Delta OD}^{SD1}}{R_{\Delta OD}^{SD2}}, \tag{26}$$

where each ΔOD value is a representative value under each condition and $SD1$ and $SD2$ are the longer and shorter S-D distances, respectively. Thus, the subtraction performance depends not only on the regressor (or shorter) channel but also on the longer channel. Experimental results were used to compare experimental AR and computed AR. The experimental AR values were calculated using the ratio of the mean value of experimental ΔOD over time points where the lower-layer change

(target) has a max value (time points: 13–18, 46–51, 79–85). Computed *AR* were calculated using $R_{\Delta OD}$, which was obtained by computed Δ*OD*.

4.5.3. Performance evaluation of subtraction method

The Δ*OD* measured at each S-D distance when the upper and lower layers were driven in white-noise and a CBV waveform, respectively (condition 1), is shown in Fig. 56. Extracted from data of Fig. 56, the Δ*OD* data obtained at 5.5-, 13.5-, 25.5-, and 37.5-mm S-D distances are shown in Fig. 57. Amplitudes of obtained signals depend on S-D distance. The Δ*OD* signal obtained at 5.5-mm S-D distance was exactly similar to stage driving signal shown in (a) of Fig. 55. Mixed signals of white-noise and CBV waveforms were obtained, but almost the same shape of CBV signal can be observed in Δ*OD* signals at longer S-D distances.

A subtraction method was applied to Δ*OD* data measured at multiple S-D distances. The subtraction results with the short-distance regression of Δ*OD* measured while both layers were driven under condition 1 are shown in Fig. 58. For the Δ*OD* data obtained at 5.5-, 13.5-, 25.5-, and 37.5-mm S-D distances, the subtraction results along with Δ*OD* that was measured at a long distance while only the lower layer was singly driven (target), are shown in Fig. 59. The noise that is commonly present in Δ*OD* signals at all S-D distances was eliminated, and a CBV signal of the lower layer was clearly obtained when the shortest S-D distance (5.5 mm) channel was used.

The results of Δ*OD* signals and subtraction method under condition 2 are shown in Figs. 60–63. As seen in Fig. 60, even if the tendency of the CBV response was not clearly visible from the raw Δ*OD* signal, the CBV signal at the lower layer was obtained when the shortest S-D distance channel was used. The subtraction method was effective even under the condition that the two waveforms had power in the same frequency range (Fig. 55).

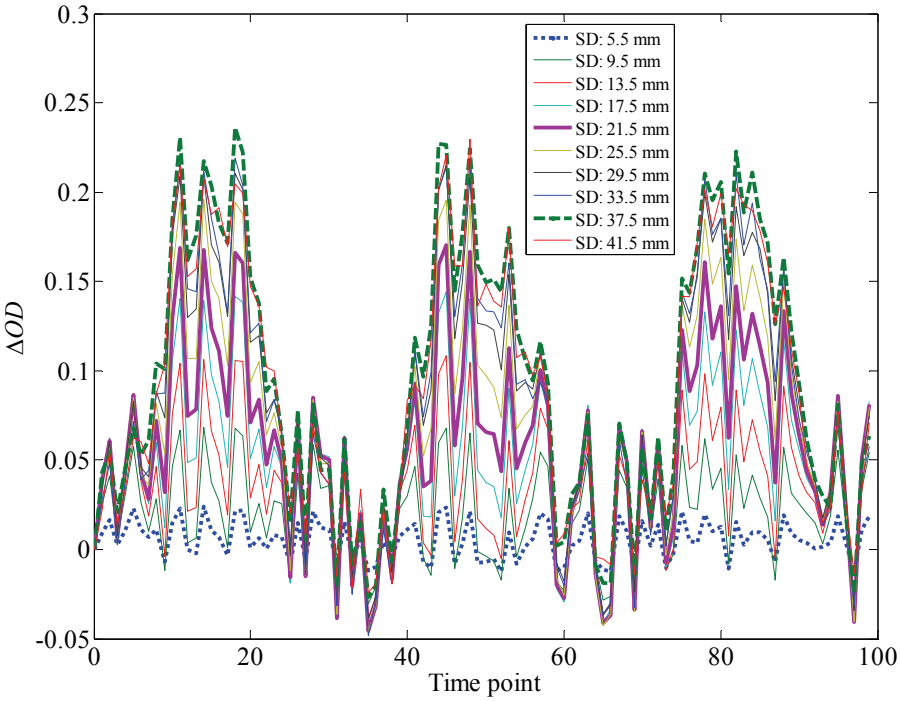

Fig. 56 Δ*OD* measured at each S-D distance as upper and lower layers driven in white-noise and CBV waveform, respectively (condition 1).

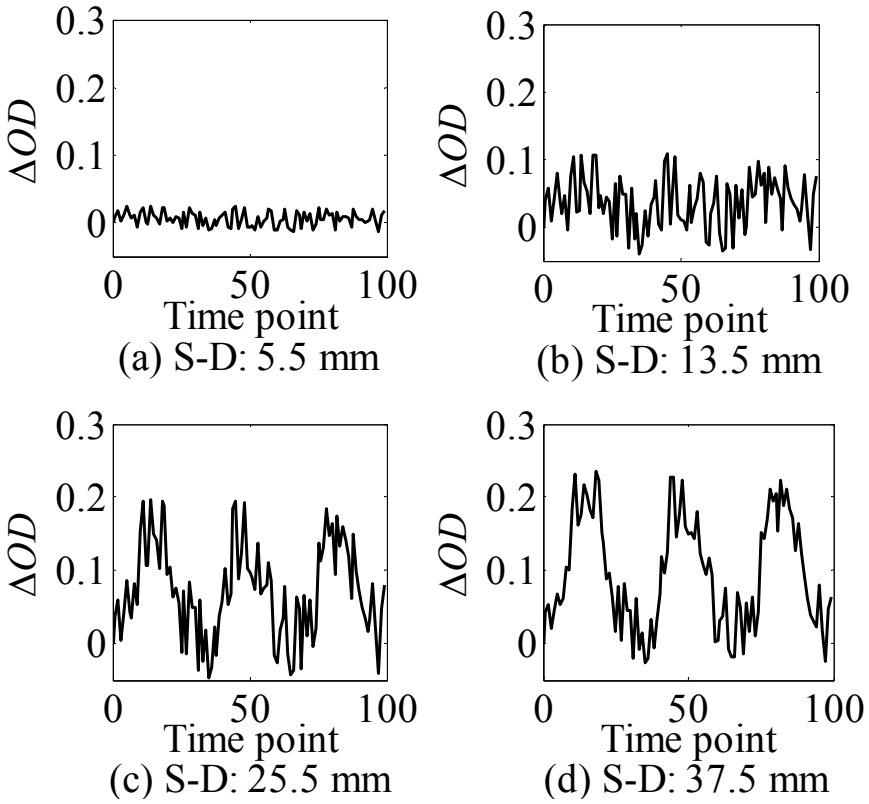

Fig. 57 Δ*OD* measured at each S-D distance as upper and lower layers driven in white-noise and CBV waveform, respectively (condition 1). S-D distances: (a) 5.5 mm, (b) 13.5 mm, (c) 25.5 mm, and (d) 37.5 mm.

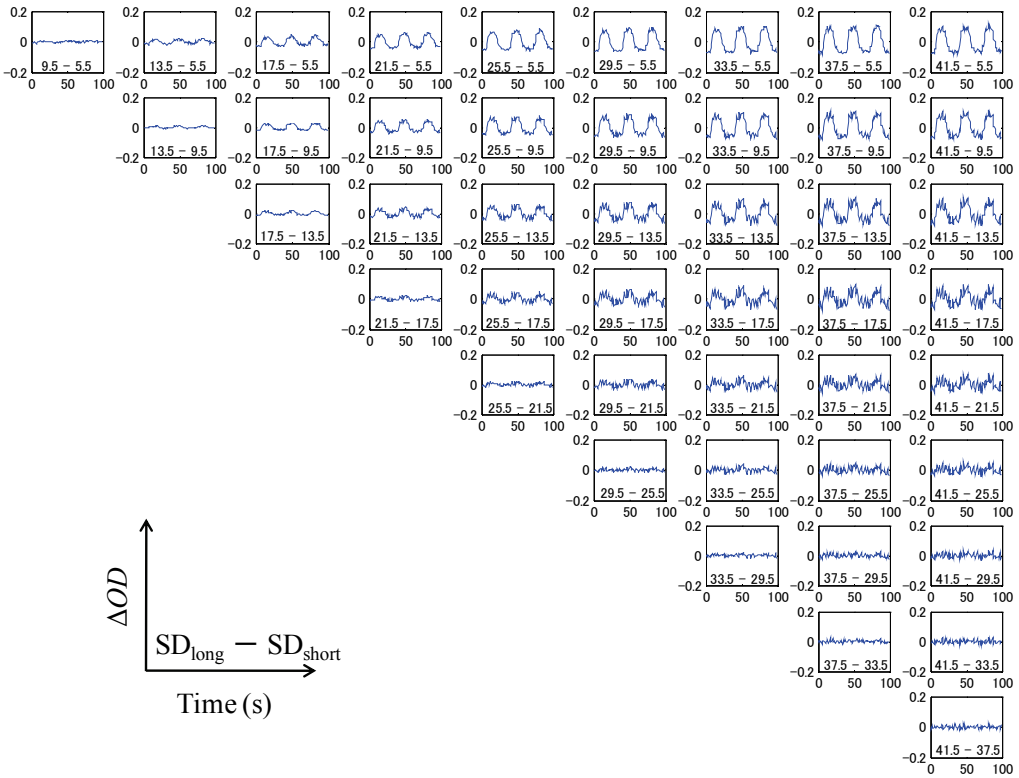

Fig. 58 Subtraction result with short-distance regression of Δ*OD* measured while both layers are driven in condition 1.

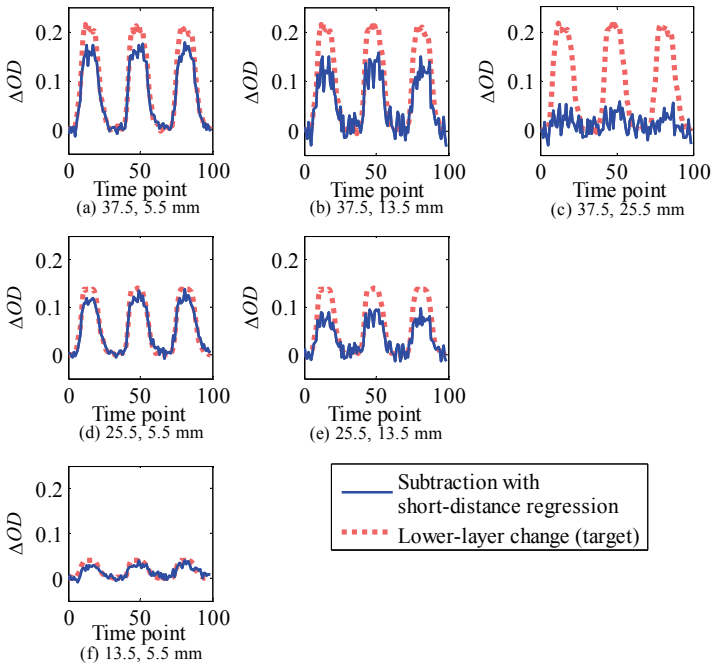

Fig. 59 Subtraction result with short-distance regression of Δ*OD* measured while both layers are driven in condition 1, and Δ*OD* measured at a long distance while only lower layer (target) is driven. Combination of S-D distances: (a) 37.5 and 5.5 mm, (b) 37.5 and 13.5 mm, (c) 37.5 and 25.5 mm, (d) 25.5 and 5.5 mm, (e) 25.5 and 13.5 mm, and (f) 13.5 and 5.5 mm.

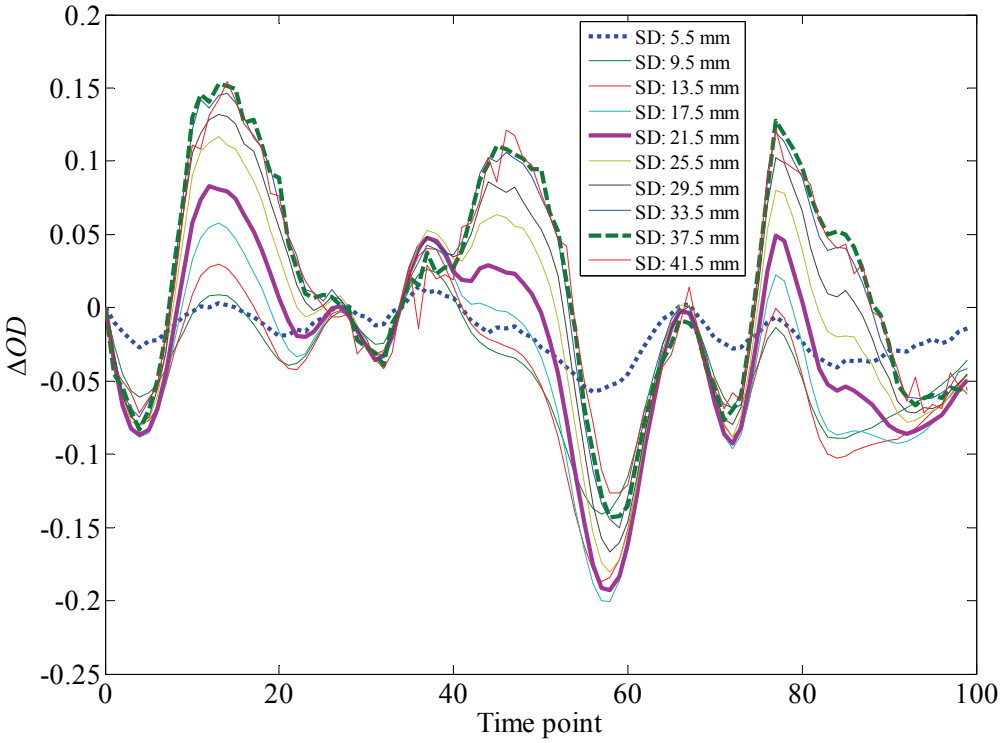

Fig. 60 Δ*OD* measured at each S-D distance as upper and lower layers were driven in waveform of biological fluctuation and CBV, respectively (condition 2).

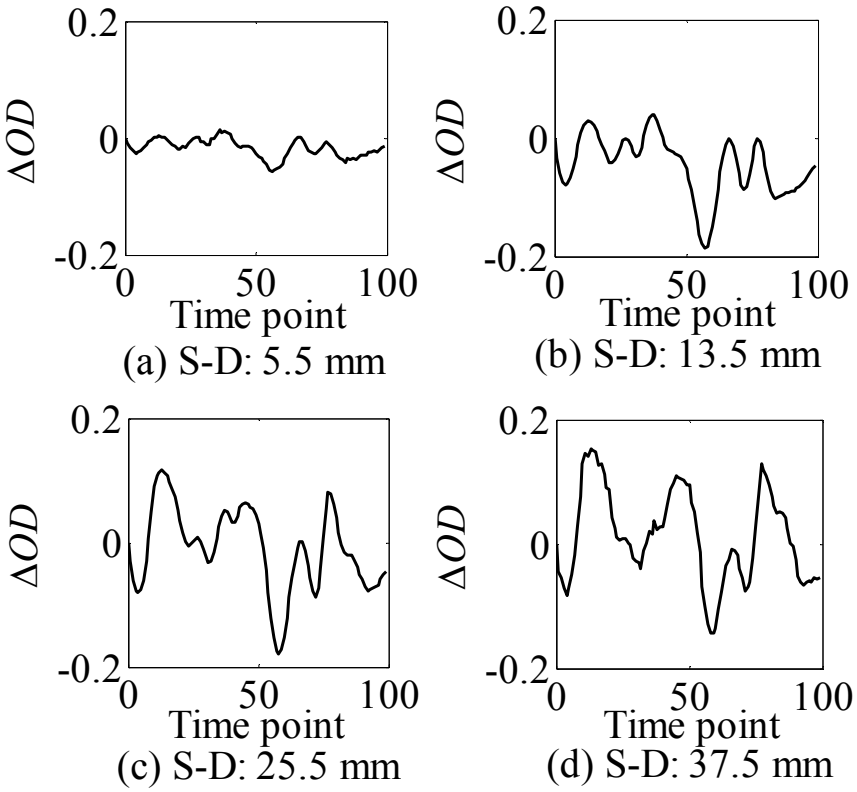

Fig. 61 Δ*OD* measured at each S-D distance as upper and lower layers were driven in waveform of biological fluctuation and CBV, respectively (condition 2). S-D distances: (a) 5.5 mm, (b) 13.5 mm, (c) 25.5 mm, and (d) 37.5 mm.

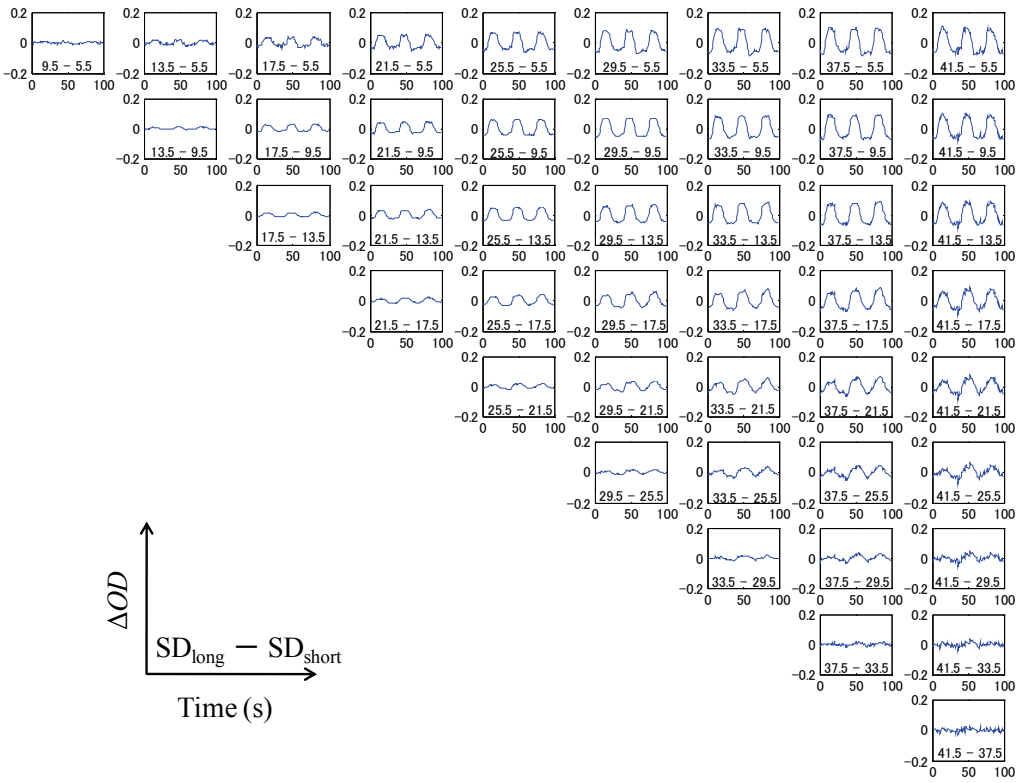

Fig. 62 Subtraction result with short-distance regression of Δ*OD* measured while both layers are driven in condition 2.

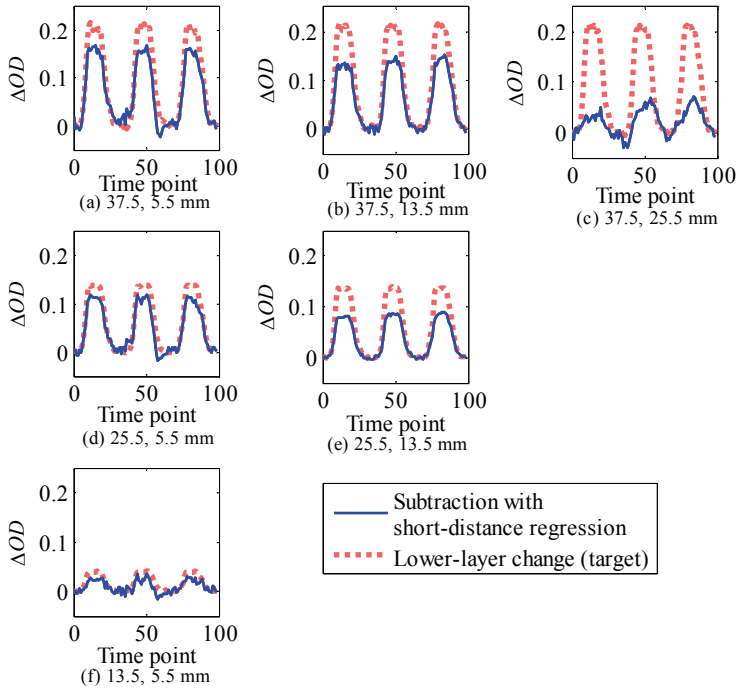

Fig. 63 Subtraction result with short-distance regression of Δ*OD* measured while both layers were driven in condition 2, and Δ*OD* measured at a long distance while only lower layer (target) was driven. Combination of S-D distances: (a) 37.5 and 5.5 mm, (b) 37.5 and 13.5 mm, (c) 37.5 and 25.5 mm, (d) 25.5 and 5.5 mm, (e) 25.5 and 13.5 mm, and (f) 13.5 and 5.5 mm.

Table 7 (a), (b), and (c) show the performance of the subtraction method defined as the amplitude ratios (*AR*s) of the subtraction result to only the lower-layer change (target) under three conditions: (a) *AR* calculated by computed Δ*OD* (based on calibration measurement), (b) experimental *AR* calculated under condition 1, and (c) experimental *AR* calculated under condition 2.

Table 7 Performance of subtraction method. Amplitude ratio (*AR*) of subtraction result to only lower-layer change (target) under three conditions: (a) *AR* from computed Δ*OD*, (b) experimental *AR* under condition 1, and (c) experimental *AR* under condition 2.

(a) *AR* from computed Δ*OD*

		Shorter S-D distance		
		5.5 mm	13.5 mm	25.5 mm
Longer S-D distance	37.5 mm	0.94	0.83	0.53
	25.5 mm	0.88	0.65	
	13.5 mm	0.65		

(b) Experimental *AR* under condition 1

		Shorter S-D distance		
		5.5 mm	13.5 mm	25.5 mm
Longer S-D distance	37.5 mm	0.77	0.59	0.13
	25.5 mm	0.86	0.56	
	13.5 mm	0.75		

(c) Experimental *AR* under condition 2

		Shorter S-D distance		
		5.5 mm	13.5 mm	25.5 mm
Longer S-D distance	37.5 mm	0.77	0.66	0.21
	25.5 mm	0.81	0.61	
	13.5 mm	0.62		

The mean error and its standard deviation of the experimental *AR* from the computed *AR* was 23 ± 22%, but under the four conditions of S-D distance combinations, the errors were less than 10%. For example, when 25.5- and 5.5-mm S-D distances were used under condition 1, the error was only 2.5%. These errors might have been caused by several factors, such as waveform combination (which differentiates correlation between two waveforms) or method of calculating *AR* (mean amplitude at certain period of time is used here). We demonstrated that the approximate performance of the subtraction method can be estimated by the computed *AR* and quantitatively showed that a shorter S-D distance is better for a regressor.

As shown in Fig. 59 and Fig. 63, a CBV response with good reproducibility was obtained three successive times. When a 25.5-mm channel was used as a regressor, the lower signal was not accurately obtained (*AR* values were 0.13 and 0.21 under conditions 1 and 2, respectively) because this channel contained a considerable amount of the lower signal ($R_{\Delta OD}$ = 2.5, Fig. 54). In the phantom measurement, up to now, it has been difficult to change the absorption coefficient (or subsequent optical density) with complete reproducibility because conventional dynamic phantoms are based on a two-state control. Our dynamic phantom, in contrast, can be applied to a variety of signal discrimination methods.

4.5.4. Signal discrimination with ICA

Independent component analysis (ICA) is a signal discrimination method that extracts independent components from mixed signals without knowledge of the obtained signal by utilizing the statistical independence of the source components (Cardoso, 1998). This method is effective for analyzing signals that have multiple signal sources and need to be measured at multiple points (Katura et al., 2008; Kohno et al., 2007).

ICA can be used to extract multiple independent components and mixing weights at each measurement position. Original observed signal can be reconstructed by totaling the products of independent components and mixing weights.

The mixing model assumed here is expressed as follows:

$$\begin{bmatrix} y_1(1) & \cdots & y_1(m) \\ \vdots & & \vdots \\ y_n(1) & \cdots & y_n(m) \end{bmatrix} = \begin{bmatrix} w_{11} & \cdots & w_{1n'} \\ \vdots & & \vdots \\ w_{n1} & \cdots & w_{nn'} \end{bmatrix} \begin{bmatrix} s_1(1) & \cdots & s_1(m) \\ \vdots & & \vdots \\ s_{n'}(1) & \cdots & s_{n'}(m) \end{bmatrix}, \quad (27)$$

where $y_i(j)$ denotes observed signal at channel i ($1 \le i \le n$) and at time j ($1 \le j \le m$), w_{ik} denotes mixing weight of independent component k ($1 \le k \le n' \le n$) on channel-i signal, and $s_k(j)$ denotes the signal of independent component k at time j.

In this study, we used the time delayed decorrelation (TDD)-ICA algorithm, which assumes that the time-delayed cross-correlation between independent components can vanish at any time (Hirosaka et al., 2004; Katura et al., 2008; Molgedey and Schuster, 1994; Ziehe and Müller, 1998). Mixed signals used in this analysis are, in this case, the time series of ΔOD ($y(1) \cdots y(m)$) recorded at multiple S-D distances (channel i ($1 \le i \le n$)).

We tested whether or not we could discriminate between absorption changes of the upper and lower layers from the obtained ΔOD time sequence data with ICA when the absorption of both layers of the phantom were simultaneously changed (condition 2, stated above). The obtained components were compared with the ΔOD time course data obtained when the absorption of only one layer was driven (actual signals). Performance was quantitatively evaluated on the basis of the correlation coefficient between the obtained component and the actual signal.

4.5.5. Performance evaluation of ICA method

Using the data obtained under condition 2 (both layers driven; upper layer: biological fluctuation, lower layer: CBV), ICA was used to extract independent components and their weights at each S-D distance. The ICA result is shown in Fig. 64 ((a) plots the time sequence of independent components extracted with ICA and (b) plots weights of each component at each S-D distance). The top-two largest components in the contributing ratio were extracted. Components 1 and 2 correspond to the absorption

change of the lower and upper layers, respectively. The correlation coefficients between the independent components (extracted when both layers were driven) and the ΔOD time course (obtained at a 25.5-mm S-D distance in advance while only each layer was driven) were 0.988 (upper layer) and 0.996 (lower layer). (The channel of the 41.5-mm S-D distance was not used because of a low signal-to-noise ratio.)

The dependence of a component's weight on S-D distance was similar to that of ΔOD and L_{eff} (see Fig. 54). The reasons for the slight difference between these dependences are 1) the interference of one layer absorption change to the sensitivity to that of other layer's absorption change, 2) the correlation between two-layer waveforms, and 3) the measurement noise.

According to Eq. (22), ΔOD is the product of the change in absorption coefficient and partial effective path length, and therefore the weights at each S-D distance in Fig. 64 (b) reflect the changes in partial effective path length depending on the S-D distance shown in Fig. 54. This result shows that the phantom simulates the absorption change in the entire layer by sliding the position of the absorber (the coefficient of which is fixed).

The effectiveness of ICA for discriminating between surface- and deep-layer effects was experimentally demonstrated under a condition in which the time-course changes in the absorption of the upper and lower layers were different (preferably, statistically independent). Such validation is difficult to ensure with human measurement because the exact amount of absorption change cannot be precisely known.

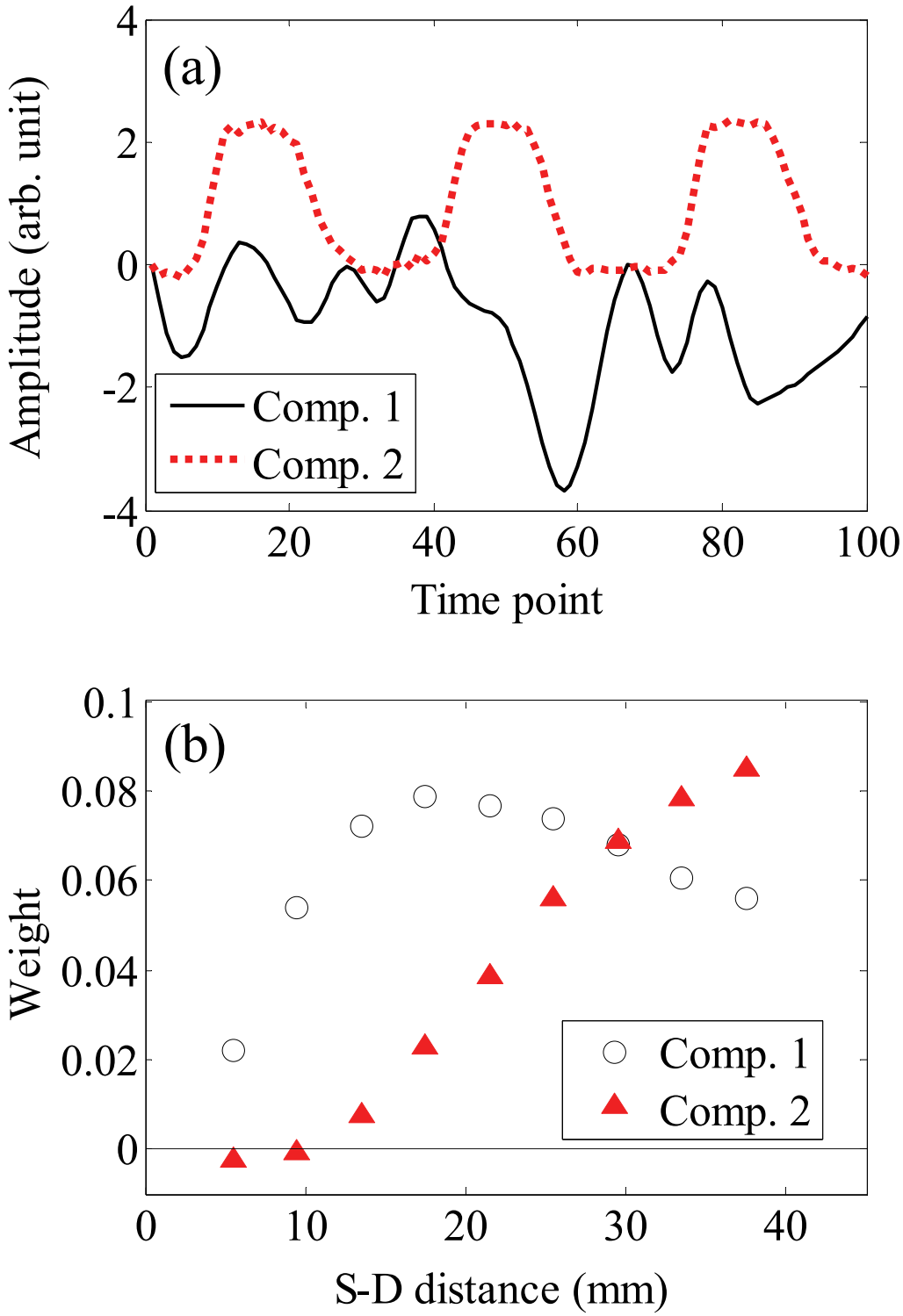

Fig. 64 ICA results. (a) Independent components extracted with ICA, (b) weights for each component at each S-D distance.

4.6. Summary

We developed a dynamic phantom for simulating tissue with two absorption layers that are independently driven with two one-axis automatic stages that can cause the absorption change of any waveform. When several simulated NIRS signals—such as white noise, physiological fluctuation, and CBV response—were created by the driving stages, the time course data of ΔOD were obtained with a good reproducibility and linear relationship to stage-position changes. These results show that ΔOD (i.e., $\Delta\mu_a$) is caused by the stage-position change (Δx).

We used this phantom to evaluate the performance of a subtraction method with a short-distance regressor. When a short S-D distance channel that is not sensitive to lower-layer absorption change is used as a regressor, the signal that resulted from subtraction was in better agreement with the actual lower signal. Furthermore, to demonstrate the advantage of simulating absorption coefficient waveforms with our phantom, we applied an ICA method to the signals obtained while two layers were concurrently driven with different time courses. When the extracted components were compared to the signal obtained when the absorber of each layer was singly driven, the correlation coefficients were over 0.98 for both layers.

These results demonstrate that our dynamic phantom can be used to evaluate methods for discriminating between the effects of scalp and cerebral blood flow in NIRS signals.

Chapter 5

Application of noncontact optical scanning system to human tissue measurement

5.1. Human muscle measurement

5.1.1. Participant

One male adult (30 years old) participated as a volunteer subject in this study. The subject provided written informed consent after being provided a complete explanation of the study.

5.1.2. Experimental setup

A human forearm was measured using a noncontact optical scanning system. S-D distances where ΔOD was measured were 10, 13.8, 17.5, 21.3, and 25 mm.

An upper-arm ischemia test was performed on the male subject. The blood flow in the upper arm was manually occluded with an inelastic band by another person for less than 60 s until the band was released. The change in optical density was measured

during the period of constriction and for 60 s after the relief.

5.1.3. Results and discussion

The change of blood volume was modeled a by single exponential function. The following function was fitted to the measured ΔOD to obtain the fitting parameters (A, B, C, τ_1, and τ_2).

$$\Delta OD_{\text{fit}}(t) = A\left[1-\exp\left(-(t-t_0)/\tau_1\right)\right]+B\exp\left(-(t-t_0)/\tau_2\right)+C\,, \tag{28}$$

where t_0 indicates the end time of occlusion (t_0 = 10 s). The measured ΔOD and the fitting lines for the data at each S-D distance are shown in Fig. 65. The upper-arm occlusion was released at t = 10 s in Fig. 65.

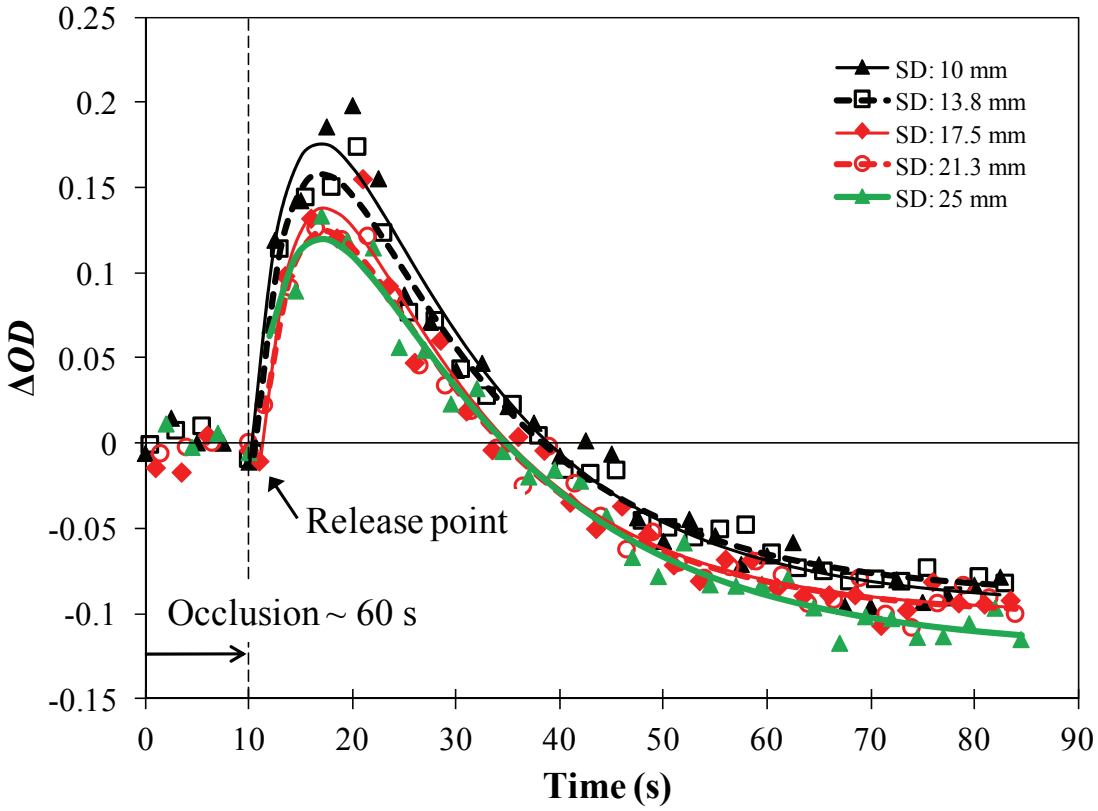

Fig. 65 ΔOD measured on forearm at S-D 10–25 mm before and after occlusion (t = 10 s) of upper arm.

The obtained ΔOD, which is proportional to the total hemoglobin (total-Hb) change calculated using the molar extinction coefficient of hemoglobin at an isosbestic point of around 800 nm, is consistent with the result of Niwayama et al. (2006). From the error distribution of the measured data, we tested the validity of residual errors between the fitting line estimated by the least-squares method and measured ΔOD data.

We did a chi-square test, setting the significance level to 5% (α = 0.05). If no significant difference is found, the model is valid under the significance level. If not, the model should be reviewed because either the data or the premise of the least-squares method is invalid. When the vector of residual error ($\boldsymbol{\varepsilon}$) between the vector of estimated ΔOD value ($\mathbf{\Delta OD_{fit}}$) and measured ΔOD data ($\mathbf{\Delta OD}$) is defined as $\boldsymbol{\varepsilon} \equiv \mathbf{\Delta OD_{fit}} - \mathbf{\Delta OD}$, and residual error's standard deviation is denoted as σ, the chi-square (χ^2) is expressed as:

$$\chi^2 \equiv \boldsymbol{\varepsilon}^t \boldsymbol{\varepsilon} / \sigma^2 . \tag{29}$$

The expected value of χ^2 is equal to the degree of freedom of the fitting line (d = 25) that is calculated by number of data points (30) minus number of parameters (5), and the experimental χ^2 has a chi-square distribution. The reduced chi-square $\tilde{\chi}^2$, expressed as

$$\tilde{\chi}^2 = \frac{\chi^2}{d} \tag{30}$$

is the chi-square divided by the degrees of freedom. When the probability that the expected reduced chi-square $\tilde{\chi}_E^2$ is larger than the measured reduced chi-square ($\tilde{\chi}^2$) is expressed as $P(\tilde{\chi}_E^2 \geq \tilde{\chi}^2)$, then

$$\alpha < P(\tilde{\chi}_E^2 \geq \tilde{\chi}^2) \tag{31}$$

is a requirement for the validity of the model. Under the condition of this measurement, the measured reduced chi-square ($\tilde{\chi}^2$) was 1.16 (degree of freedom: 25) at all S-D distances. Since $\alpha = 0.05$ and $P(\tilde{\chi}_E^2 \geq \tilde{\chi}^2) > 0.22$ ($\tilde{\chi}^2 = 1.2$, degree of freedom: 26) $> \alpha$, the model (Eq. (28)) was validated.

5.2. Human brain-activity measurement

5.2.1. Participant

One male adult (30 years old) participated as a volunteer subject in this study. The subject provided written informed consent after being provided a complete explanation of the study.

5.2.2. Experimental setup

To apply the subtraction method to human brain-activity measurement data, our optical scanning system was used to measure a human forehead. A block diagram for measuring a human forehead using the optical scanning system and a photograph of the system are shown in Fig. 66 and Fig. 67, respectively. The optical scanning system that consisting of a galvano mirror, an 808-nm LD, and an APD module was installed over subject's head. The LD was driven by a laser driver connected to a function generator. The function generator sends a 3.3 kHz amplitude-modulated signal to both the laser driver and the lock-in amplifier as reference signals. The intensity of irradiation power was changed according to S-D distance controlled by a PC. The PC sends an amplitude-control signal to a general purpose interface bus (GPIB) controller connected to the function generator, and also sends a galvano-control signal to a galvano controller connected to the galvano mirror. The

output of the APD module was lock-in detected by a lock-in amplifier and sent to an analog-to-digital (A/D) converter. The mirror-angle signal from the galvano controller and laser Doppler signals and marker signal from the stimulation presentation PC were also sent to the A/D converter. The output of the A/D converter was recorded by the PC.

A total of 5 points were scanned at S-D distances of 7, 12.5, 18, 23.5, and 29 mm. The phosphor and an optical filter (InP) were placed on the forehead above left eyebrow near Fp1 according to the International 10–20 electrode placement method (Jasper, 1958). Two laser-Doppler probes were placed near the detection point (position of phosphor and InP), and microvascular blood flow in the forehead skin was measured by a laser Doppler flowmeter (LDF, MicroFlo DSP, Oxford Optronix, UK).

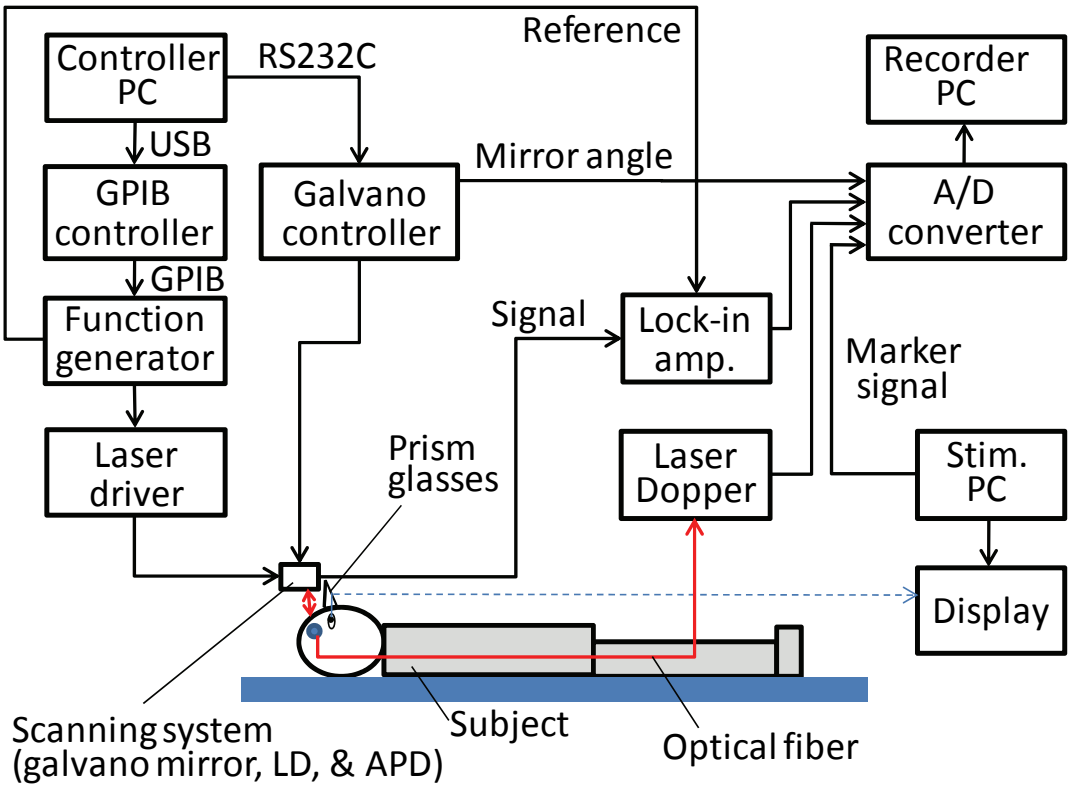

Fig. 66 Block diagram for measuring a human forehead using the optical scanning system. Stim. PC: stimulation-presentation PC, A/D converter: analog-to-digital converter, Lock-in amp.: lock-in amplifier, LD: laser diode, and APD: avalanche photo diode.

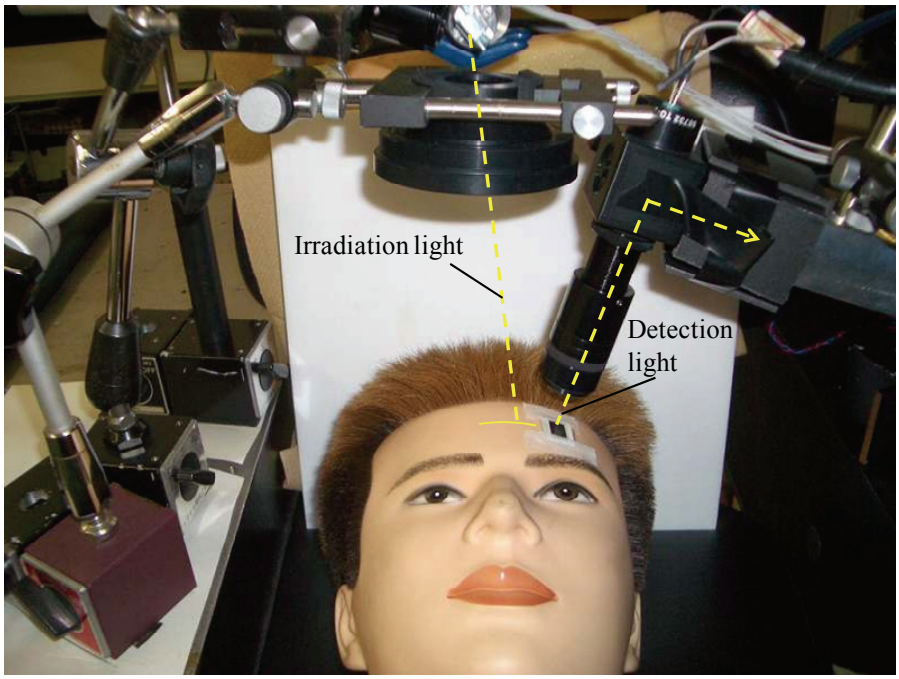

Fig. 67 Experimental setup of optical scanning system for measuring a human forehead. In the actual measurement, the subject wore prism glasses over his eyes so he could see the PC display in the direction of his feet, and two laser-Doppler probes were put on his forehead.

As a cognitive task for inducing brain activation, a verbal working-memory task (Aoki et al., 2011; Sato et al., 2011) was used because it has been reported that the activation region during performance of a verbal working memory task is larger than that during a spatial working memory task (Sato et al., 2011), and the amplitude of NIRS signal is also larger for a verbal working memory task (Aoki et al., 2011; Sato et al., 2011). The sequence of the verbal working memory task is shown in Fig. 68. In the task, the subject was requested to look at the center of a screen. Each trial starts with a 1.5-s presentation of the target screen, which is followed by a 7-s delay. A probe screen is then presented for 2 s. In the target screen, 4 Japanese characters categorized as “Hiragana” are presented. In the probe screen, only a single Japanese character categorized as “Katakana” is presented. After the probe stimulus is presented, the subject judges whether the character presented in the probe screen has a same sound as any of the 4 characters presented in the target screen. The trial was repeated 16 times. The task was presented through the Platform of Stimuli and Tasks software that was developed by Hitachi, Ltd. The display for presentation of the task

was located in the direction of subject's feet. The subject saw the display through prism glasses placed over his eyes.

The experiment was repeated three times. The S-D distances at five points changed slightly (within several millimeters) at each setup. Three data sets obtained during the same task were used, but only the figures from one experiment are shown in the following results. For calculation of correlation coefficient data between Hb signals and LDF signals, all three data sets were used.

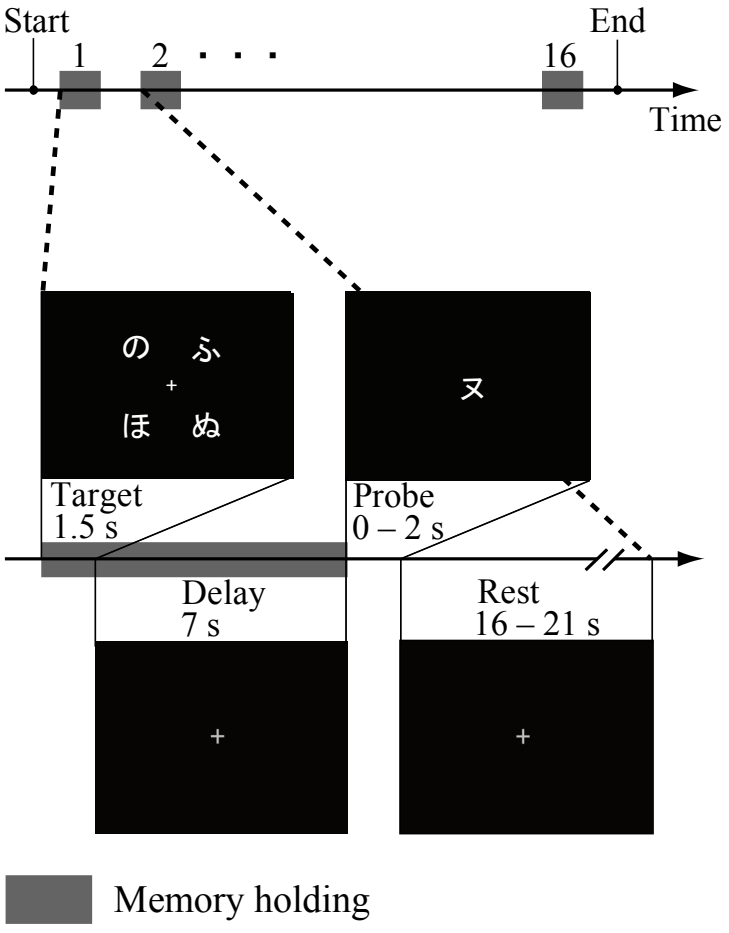

Fig. 68 Sequence of a verbal working memory task used for measuring brain activation. The subject is requested to look at the center of the screen during the experiment and memorize the positions of 4 Japanese characters categorized as "Hiragana" in a target screen and judge whether a Japanese character categorized as "Katakana" in a probe screen has a same sound as any of the characters in the target screen. The subject has to memorize the 4 characters for 8.5 s during the display of the target screen and delay screen in each trial.

5.2.3. Results and discussion

Because only one wavelength (808 nm) of light was used in the experiment, the change in the total-Hb was calculated assuming that the wavelength is approximately at an isosbestic point of the absorption coefficient of oxy- and deoxy-Hb. When the wavelength is at an isosbestic point, the change in total-Hb can be calculated using the molar extinction coefficient and the change in optical density:

$$\Delta\left(C_{total} \times L\right) = \frac{\Delta OD}{\varepsilon_{Hb}^{natural}}, \tag{32}$$

where,

$$\varepsilon_{Hb}^{natural} = \varepsilon_{Hb}^{common} \times \ln(10) = 0.196 \quad (\mathrm{mM}^{-1} \cdot \mathrm{mm}^{-1}), \tag{33}$$

$\varepsilon_{Hb}^{natural}$ and $\varepsilon_{Hb}^{common}$ denote molar extinction coefficients based on natural logarithm and common logarithm, respectively. Change in optical density (ΔOD) was calculated by Eq. (21).

Continuous total-Hb signals measured at S-D distances of 7, 12.5, 18, 23.5, and 29 mm are shown in Fig. 69. Block-averaged total-Hb data measured at S-D distances of 12.5, 18, 23.5, and 29 mm are shown in Fig. 70. The task-related change in total-Hb was obtained at an S-D distance of 29 mm. Data obtained at an S-D distance of 7 mm were not used, because the excitation of the light at a 7-mm S-D distance was very close to that of the phosphor-holding heavy paper, and a slight body movement can affect the quality of the data at the shortest S-D distance. For analysis of the other 2 experiments, the data at the shortest S-D distance were used for the subtraction method to be mentioned later.

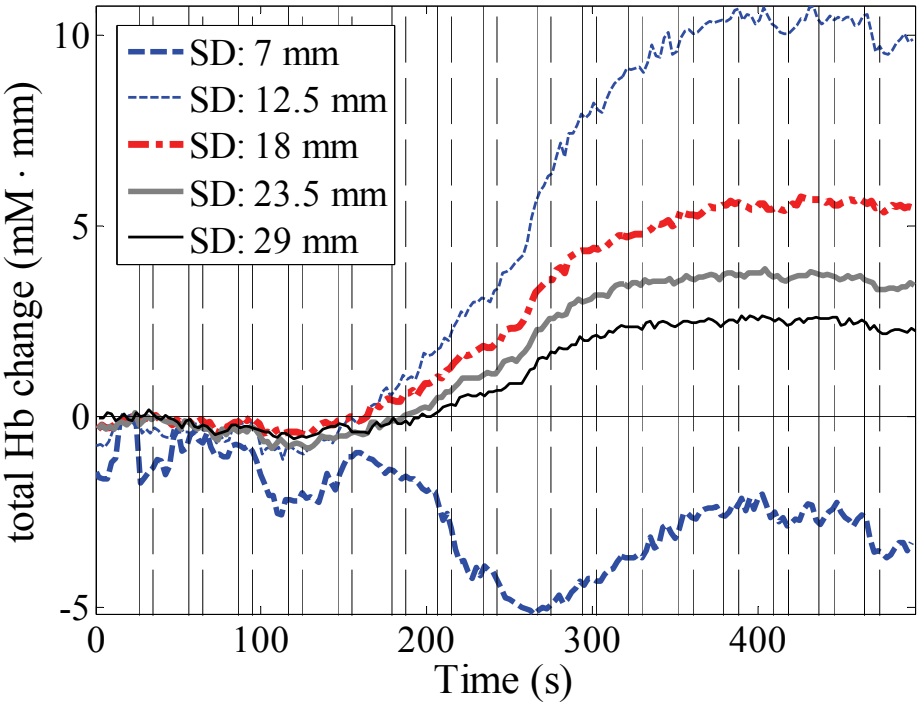

Fig. 69 Continuous total-Hb signals measured at S-D distances of 7, 12.5, 18, 23.5, and 29 mm. Solid and broken vertical lines represent start and end times of the memory holding trials (16 trials in total).

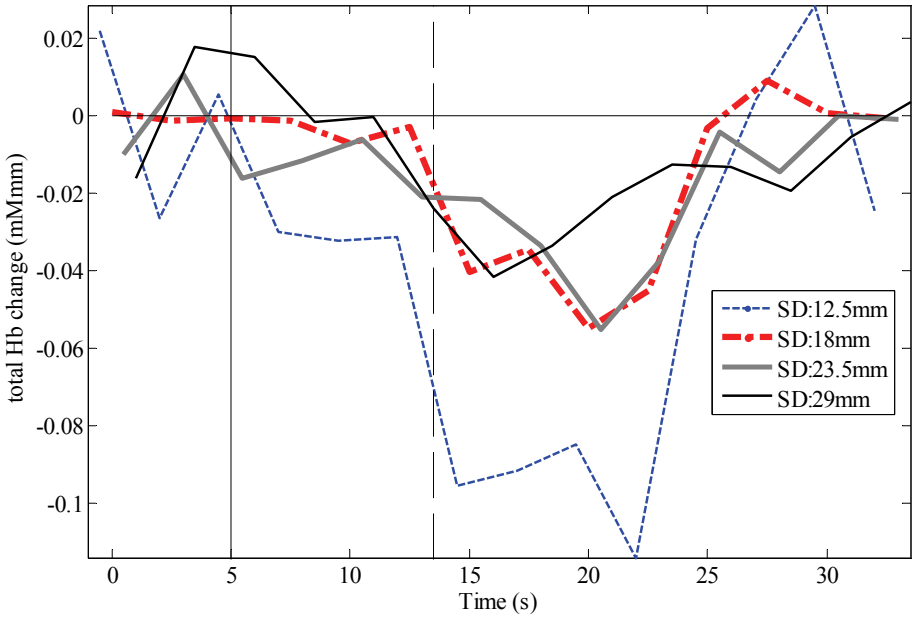

Fig. 70 Block-averaged total-Hb data measured at S-D distances of 12.5, 18, 23.5, and 29 mm. Solid and broken vertical lines represent start and end times of the memory holding trials. The subtraction method was performed using total-Hb changes obtained at S-D distances of 29 and 12.5 mm.

The estimated deep signal was obtained using the subtraction method with a shorter S-D distance channel. The deep signal (subtracted data from the total Hb signal) at an S-D distance of 29 mm, the shallow signal (scaled data for an Hb signal at an S-D distance of 12.5 mm), and the raw total Hb signal at 29 mm for implementation of the subtraction method are shown in Fig. 71 (a). An LDF signal for performance evaluation of the subtraction method is shown in Fig. 71 (b).

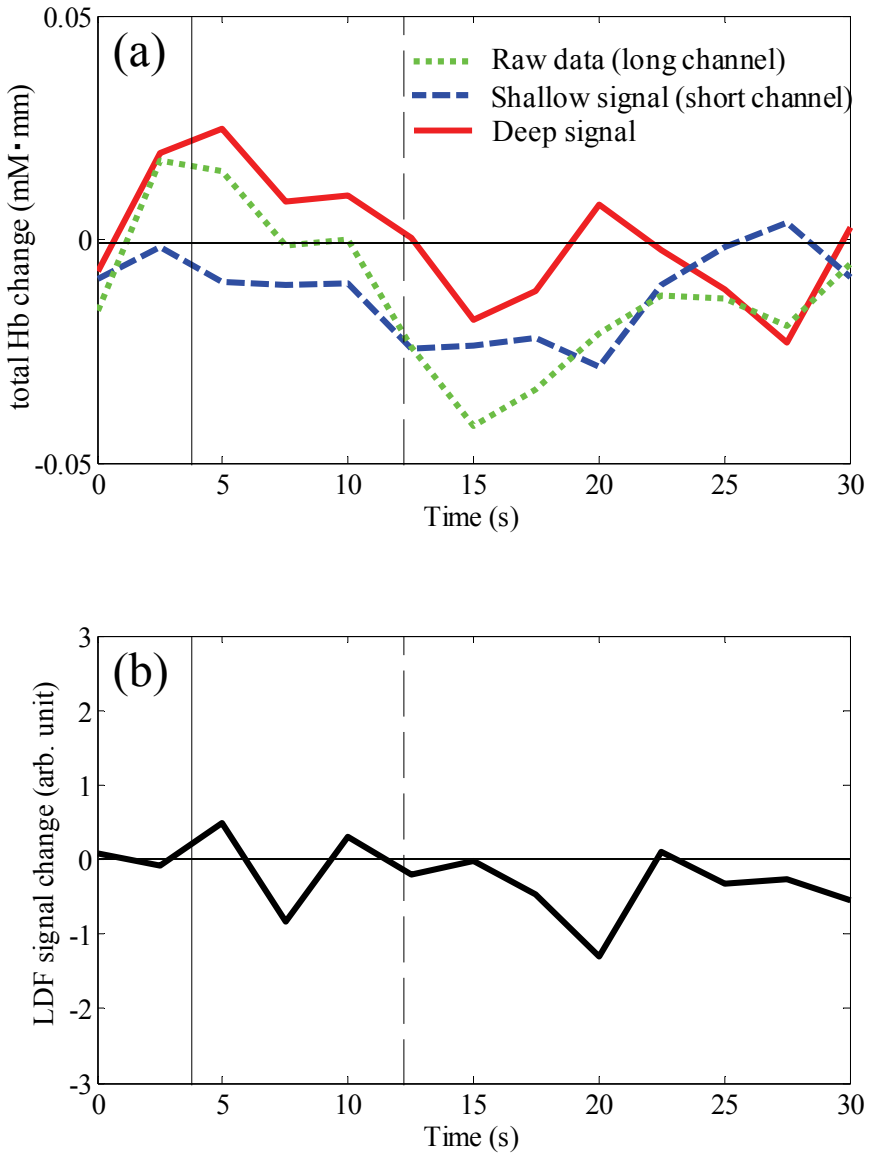

Fig. 71 (a) Deep signal (subtracted data from the total Hb signal) at an S-D distance of 29 mm, shallow signal (scaled data of S-D 12.5-mm Hb signal), and raw total Hb signal at 29 mm for implementation of the subtraction method; (b) LDF signal for performance evaluation of the subtraction method. Solid and broken vertical lines represent start and end times of the memory holding trial.

The correlation coefficients between the LDF signal and the Hb signals (raw, shallow, and deep signals) calculated using the data from 3 repeated experiments are shown in Fig. 72. The correlation coefficients between the LDF signal and raw data, shallow signal, and deep signal were 0.17 ±0.24, 0.45 ±0.12, and –0.04 ±0.26, respectively. The correlation coefficients were calculated using averaged block data (13 data points).

The result demonstrated that the subtraction method is effective for extracting a task-related deep signal that is less correlated with the LDF signal than the original signal, and that our optical scanning system can be used as a multi-distance NIRS system for measuring a human forehead.

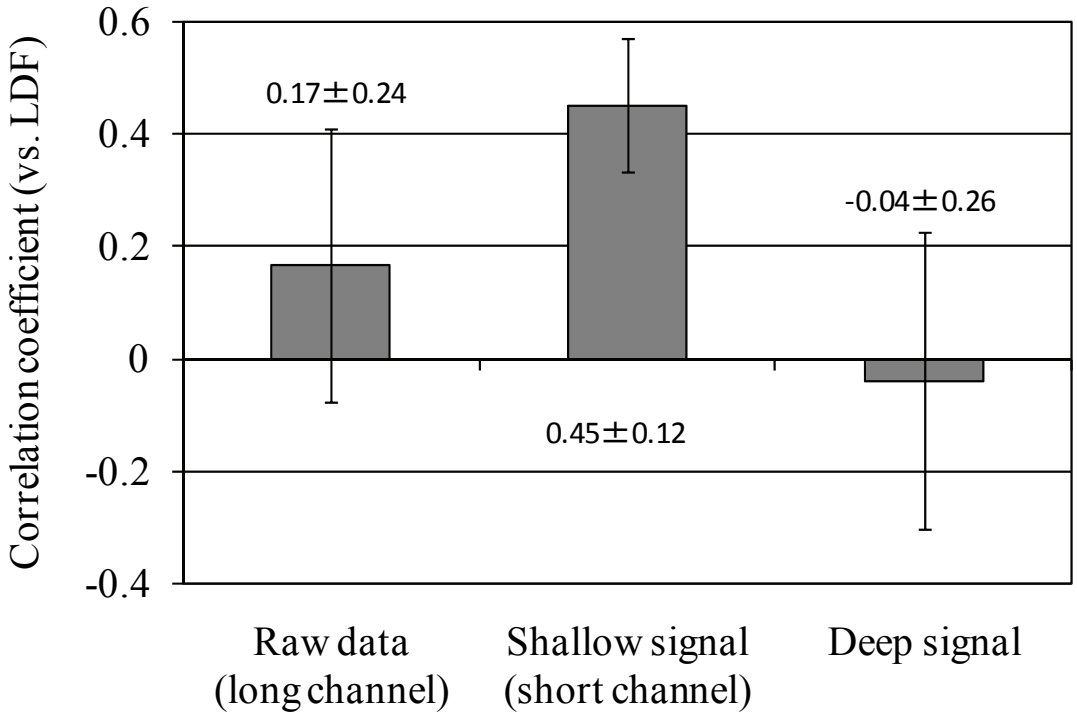

Fig. 72 Correlation coefficients (mean ± standard deviation) between the LDF signal and the raw data at a long channel, shallow signal (short channel), and deep signal. Error bars indicate the standard deviations among three repeated measurements (16 blocks for each) for a single participant.

5.3. Summary

Human muscle measurement during upper-arm occlusion and relief was described. The optical density change depending on S-D distance was obtained, which demonstrated the possibility that the optimal S-D distance for oxygenation monitoring on the human forearm can be determined by the scanning system.

Furthermore, our optical scanning system was used for measuring human brain activity at the forehead. The subtraction method for extracting deeper-layer signals that was evaluated by our dynamic phantom was applied to actual human brain-tissue measurement data. Based on the correlation with the laser-Doppler signal, a deep-layer signal with lower correlation than the original signal was successfully extracted using short (12.5 mm) and long (29 mm) S-D distance channels, which demonstrated that the subtraction method is effective and that our optical scanning system can be used as a multi-distance NIRS system for measuring the human forehead.

Chapter 6

Conclusion

6.1. Summary of results and their relationships

This thesis described the principle of a noncontact optical brain-activity monitoring technology and demonstrated its application to human brain-activity measurement. The principle involves a phosphor layer placed on the skin and optical filters for eliminating excitation light and stray light. Thus both the emitter and detector probes of the NIRS system are not in contact with the skin. Simultaneous measurements using both a conventional contact OT system and our noncontact system were conducted, and the waveforms obtained from both systems were verified to be almost equivalent.

By applying the principle of noncontact optical measurement of deep tissue, an optical scanning system was developed that changes the irradiation focal point over time and measures the tissue at multiple S-D distances. The change in light absorption by deep tissue is measured while the detection focal point is fixed and irradiation focal point is changed over time with a galvano mirror. The S-D distance can be adjusted flexibly, so small measurement intervals (~ 2 mm) between nearest-neighbor irradiation focal points are realized.

This thesis proposed a method for estimating adipose thickness based on the

gradient of optical-density change (ΔOD) with respect to S-D distance, and demonstrated the method in an experiment using a phantom whose superficial thickness was varied from 1 to 12 mm.

To investigate the effectiveness of our noncontact optical biological measurement system and of analytical methods for discriminating between the effects of superficial and deep tissues, a dynamic phantom was developed that has two absorber layers, each of which is independently driven by a one-axis automatic stage. High reproducibility of ΔOD-waveform generation with this dynamic phantom was demonstrated. Furthermore, by applying a subtraction method using a short S-D-distance channel to multi-distance measurement data, the performance of S-D distance combination for discriminating between the effects of surface and deep layers was quantitatively evaluated. Doing so has been difficult for *in vivo* measurements in humans because the actual change in surface- and deep-layer absorption cannot be determined.

The noncontact NIRS scanning system was used to measure human tissue. A noncontact measurement of human forearm muscle was performed with the optical scanning system, and the dependence of ΔOD caused by upper-arm occlusion and release on S-D distance was found. The results demonstrated the effectiveness of multi-S-D distance measurement using our optical scanning system for human forearm measurement. Furthermore, the surface-layer discrimination method with short-channel regressor was applied to multi-distance measurement data acquired at a human forehead with our optical scanning system. As a result, scalp- and deep-layer absorption changes were successfully extracted, as shown by experiments using the dynamic phantom.

In this way, this study proposed and demonstrated the noncontact optical biological measurement technique, conducted preliminary experiments for application to forearm muscle and head tissue measurements, and discussed the effectiveness of the system.

6.2. Perspective for the future

A promising application of the NIRS scanning system in biological measurement is the measurement of human muscle-tissue oxygenation. The S-D distance that produces a maximum signal amplitude has been reported to depend on adipose-tissue thickness (Feng et al., 2001), but the adipose-tissue thickness should be measured beforehand by, for example, ultrasonography (Niwayama et al., 2000; Niwayama et al., 2006). A method to optically measure adipose-tissue thickness by using the spectral peak of fat at 930 nm has been reported (Geraskin et al., 2009); however, this method cannot be used to measure muscle-tissue oxygenation.

With the scanning system developed in the present study, relative muscle-tissue oxygenation can be measured and, at the same time, human adipose-tissue thickness can be estimated from the ΔOD spatial profile calculated from ΔOD measured under various adipose-tissue thicknesses or by Monte Carlo simulation. In human-forearm measurement, the same method for estimating superficial-tissue thickness can be applied by changing muscle oxygenation by means of an inflatable cuff. Moreover, the optimal S-D distance that produces the maximal signal amplitude can be experimentally determined. Though the accuracy of adipose-tissue thickness obtained from this scanning system is lower than that obtained from ultrasonography, the scanning system has the advantage that both deep-layer absorption and surface-layer thickness can be estimated by a single all-optical measurement. Utilizing multiple detectors or an infrared imaging system with a high signal-to-noise ratio would improve the efficiency of data acquisition and spatial resolution.

Further research on the measurement of a more complicated structure will lead to better prospects for such biological-tissue measurement in humans.

Systemic fluctuations related to blood pressure or heart rate—in particular, because of dynamic cerebral autoregulation (Panerai et al., 2005; Zhang et al., 1998) or veins on the brain surface (Kirilina et al., 2012; Tong et al., 2011)—can influence the NIRS signal (Tachtsidis et al., 2008; Tachtsidis et al., 2009). In these cases, to extract the signal of cerebral blood including the systemic signal, we need to use a

signal discrimination method that considers the dependence of signal amplitude on S-D distance instead of only the waveform characteristics of the signal.

The dynamic phantom that we developed in the present study should contribute to the direct validation of other methods for extracting desired signals (e.g., a CBV signal) from mixed signals. It should be noted that, however, the results from this phantom cannot be easily generalized because its structure and optical properties are not the same as those of the human body. If this phantom model is extended to more realistic geometries with less spatial homogeneity, results from the phantom would be more reliable and would contribute to signal discrimination.

In particular, the effects of correlation or covariance, frequency characteristics, and waveforms on signal-processing methods can be directly and quantitatively investigated.

If the detector of our noncontact system is replaced with a high sensitivity CCD camera, the degree of freedom at the interface between instruments and human subjects will increase and the application range of this technique will be broadened. For example, the lack of pressure on the skin can be utilized in long-term brain activity monitoring during sleep, cognitive-state monitoring during automobile driving, and psychological- and physiological-state monitoring during office work. Moreover, this technique may be also used for noncontact monitoring of infants. In the future, this noncontact technology is expected to be applied to more practical uses in the real world.

The sensitivity of the system can be improved if more-effective phosphors are found, if high-sensitivity optical detectors or image sensors are developed, and if progress is made toward new optical filters that have a high suppression ratio. The thickness of the phosphor layer attached to the tissue surface should be optimized in order to maximize efficiency. Our technology can be applied to nondestructive, noncontact monitoring and testing technologies for materials other than biological tissues.

The NIRS imaging method—which is safe, requires small equipment, and is subject to few constraints—has great advantages in research on the neurological

development of infants and children, and in clinical research on psychiatric disease. In particular, the NIRS instrument can be used even in cases where large fMRI and PET apparatuses are difficult to use. Meanwhile, the effect of scalp blood flow on NIRS signals has been reported (Germon et al., 1998; Smielewski et al., 1997; Takahashi et al., 2011) in several papers and cannot be ignored in NIRS measurements. A method needs to be developed for discriminating between scalp and cerebral blood. A noncontact system that requires no skin compression can be used for quantitative evaluation of scalp blood flow. In the future, more sophisticated phantoms that are more specific to each tissue will improve the performance of this technique and will lead to a more practical method for extracting scalp blood flow effects.

Furthermore, since the NIRS method alleviates the physical and mental burdens on participants, measurements can be conducted under more natural conditions, which has not previously been possible. The accumulation of measurement data obtained in such an environment will lead to new insight into neuroscience, to advances in research on various diseases, and, ultimately, to improvement of our quality of life.

References

Amiot, C., Xu, S., Liang, S., Pan, L., Zhao, J., 2008. Near-Infrared Fluorescent Materials for Sensing of Biological Targets. Sensors 8, 3082-3105.

Aoki, R., Sato, H., Katura, T., Utsugi, K., Koizumi, H., Matsuda, R., Maki, A., 2011. Relationship of negative mood with prefrontal cortex activity during working memory tasks: An optical topography study. Neuroscience Research 70, 189-196.

Aqil, M., Hong, K.-S., Jeong, M.-Y., Ge, S.S., 2012. Cortical Brain Imaging by Adaptive Filtering of NIRS Signals. Neuroscience Letters 514, 35-41.

Aslin, R.N., Mehler, J., 2005. Near-infrared spectroscopy for functional studies of brain activity in human infants: promise, prospects, and challenges. Journal of Biomedical Optics 10, 11009.

Atsumori, H., Kiguchi, M., Obata, A., Sato, H., Katura, T., Utsugi, K., Funane, T., Maki, A., 2007. Development of a Multi-channel, Portable Optical Topography System. Proceedings of the 29th Annual International Conference of the IEEE, Engineering in Medicine and Biology Society, 2007, 3362-3364.

Atsumori, H., Kiguchi, M., Katura, T., Funane, T., Obata, A., Sato, H., Manaka, T., Iwamoto, M., Maki, A., Koizumi, H., Kubota, K., 2010. Noninvasive imaging of prefrontal activation during attention-demanding tasks performed while

walking using a wearable optical topography system. Journal of Biomedical Optics 15, 046002.

Atsumori, H., Kiguchi, M., Obata, A., Sato, H., Katura, T., Funane, T., Maki, A., 2009. Development of wearable optical topography system for mapping the prefrontal cortex activation. Review of Scientific Instruments 80, 043704.

Boas, D.A., Dale, A.M., Franceschini, M.A., 2004. Diffuse optical imaging of brain activation: approaches to optimizing image sensitivity, resolution, and accuracy. Neuroimage 23 Supplement 1, S275-288.

Boushel, R., Piantadosi, C.A., 2000. Near-infrared spectroscopy for monitoring muscle oxygenation. Acta Physiologica Scandinavica 168, 615-622.

Brazy, J.E., Lewis, D.V., Mitnick, M.H., vander Vliet, F.F.J., 1985. Noninvasive Monitoring of Cerebral Oxygenation in Preterm Infants: Preliminary Observations. Pediatrics 75, 217.

Buxton, R.B., Uludag, K., Dubowitz, D.J., Liu, T.T., 2004. Modeling the hemodynamic response to brain activation. Neuroimage 23, S220-S233.

Cardoso, J.F., 1998. Blind signal separation: statistical principles. Proceedings of the IEEE 86, 2009-2025.

Chance, B., Zhuang, Z., UnAh, C., Alter, C., Lipton, L., 1993. Cognition-activated low-frequency modulation of light absorption in human brain. Proceedings of the National Academy of Sciences of the United States of America 90, 3770-3774.

Cui, X., Bryant, D.M., Reiss, A.L., 2012. NIRS-based hyperscanning reveals increased interpersonal coherence in superior frontal cortex during cooperation. Neuroimage 59, 2430–2437.

Delpy, D.T., Cope, M., van der Zee, P., Arridge, S., Wray, S., Wyatt, J., 1988. Estimation of optical pathlength through tissue from direct time of flight measurement. Physics in Medicine and Biology 33, 1433-1442.

Fabbri, F., Sassaroli, A., Henry, M.E., Fantini, S., 2004. Optical measurements of absorption changes in two-layered diffusive media. Physics in Medicine and Biology 49, 1183-1201.

Farrell, T.J., Patterson, M.S., Wilson, B., 1992. A diffusion theory model of spatially resolved, steady-state diffuse reflectance for the noninvasive determination of tissue optical properties in vivo. Medical Physics 19, 879-888.

Feng, W., Haishu, D., Fenghua, T., Jun, Z., Qing, X., Xianwu, T., 2001. Influence of overlying tissue and probe geometry on the sensitivity of a near-infrared tissue oximeter. Physiological Measurement 22, 201-208.

Ferrari, M., Binzoni, T., Quaresima, V., 1997. Oxidative metabolism in muscle. Philosophical Transactions of the Royal Society B 352, 677-683.

Firbank, M., Delpy, D.T., 1993. A design for a stable and reproducible phantom for use in near infra-red imaging and spectroscopy. Physics in Medicine and Biology 38, 847.

Firbank, M., Oda, M., Delpy, D.T., 1995. An improved design for a stable and reproducible phantom material for use in near-infrared spectroscopy and imaging. Physics in Medicine and Biology 40, 955-961.

Fox, M.D., Snyder, A.Z., Vincent, J.L., Raichle, M.E., 2007. Intrinsic fluctuations within cortical systems account for intertrial variability in human behavior. Neuron 56, 171-184.

Fuchi, S., Sakano, A., Mizutani, R., Takeda, Y., 2009. High Power and High Resolution Near-Infrared Light Source for Optical Coherence Tomography Using Glass Phosphor and Light Emitting Diode. Applied Physics Express 2, 032102.

Fuchino, Y., Sato, H., Maki, A., Yamamoto, Y., Katura, T., Obata, A., Koizumi, H., Yoro, T., 2006. Effect of fMRI acoustic noise on sensorimotor activation examined using optical topography. Neuroimage 32, 771-777.

Fukui, Y., Ajichi, Y., Okada, E., 2003. Monte Carlo prediction of near-infrared light propagation in realistic adult and neonatal head models. Applied Optics 42, 2881-2887.

Funane, T., Atsumori, H., Sato, H., Kiguchi, M., Maki, A., 2009a. Multi-wavelength measurement of cytochrome oxidase and water in biomedical tissues using optical topography system. Optical Tomography and Spectroscopy of Tissue

VIII. SPIE, San Jose, CA, USA, pp. 71740A.

Funane, T., Atsumori, H., Sato, H., Kiguchi, M., Maki, A., 2009b. Relationship between wavelength combination and signal-to-noise ratio in measuring hemoglobin concentrations using visible or near-infrared light. Optical Review 16, 442-448.

Funane, T., Atsumori, H., Suzuki, A., Kiguchi, M., 2010. Noncontact brain activity measurement system based on near-infrared spectroscopy. Applied Physics Letters 96, 123701.

Funane, T., Atsumori, H., Suzuki, A., Kiguchi, M., 2011a. Noncontact optical brain activity measurement system using phosphor placed on skin. Japanese Journal of Applied Physics 50, 077001.

Funane, T., Kiguchi, M., Atsumori, H., Sato, H., Kubota, K., Koizumi, H., 2011b. Synchronous activity of two people's prefrontal cortices during a cooperative task measured by simultaneous near-infrared spectroscopy. Journal of Biomedical Optics 16, 077011.

Funane, T., Atsumori, H., Kiguchi, M., Tanikawa, Y., Okada, E., 2011c. Optical scanning system for light-absorption measurement of deep biological tissue. Review of Scientific Instruments 82, 093101.

Funane, T., Obata, A., Atsumori, H., Sato, H., Katura, T., Kiguchi, M., 2011d. Discrimination of skin blood flow using multi-distance probe and independent component analysis in optical Brain function monitoring. The papers of technical meeting, IEE Japan, OQD-11, 17-22.

Funane, T., Atsumori, H., Kiguchi, M., Tanikawa, Y., Okada, E., 2012. Dynamic phantom with two stage-driven absorbers for mimicking hemoglobin changes in superficial and deep tissues. Journal of Biomedical Optics 17, 047001.

Fuster, J.M., 1997. The Prefrontal Cortex: Anatomy, Physiology, and Neuropsychology of the Frontal Lobe 3rd ed. Lippincott-Raven Philadelphia, Chapter 6.

Gagnon, L., Perdue, K., Greve, D.N., Goldenholz, D., Kaskhedikar, G., Boas, D.A., 2011. Improved recovery of the hemodynamic response in diffuse optical

imaging using short optode separations and state-space modeling. Neuroimage 56, 1362-1371.

Geraskin, D., Boeth, H., Kohl-Bareis, M., 2009. Optical measurement of adipose tissue thickness and comparison with ultrasound, magnetic resonance imging, and callipers. Journal of Biomedical Optics 14, 044017.

Germon, T.J., Evans, P.D., Manara, A.R., Barnett, N.J., Wall, P., Nelson, R.J., 1998. Sensitivity of near infrared spectroscopy to cerebral and extra-cerebral oxygenation changes is determined by emitter-detector separation. Journal of Clinical Monitoring and Computing 14, 353-360.

Godavarty, A., Sevick-Muraca, E.M., Eppstein, M.J., 2005. Three-dimensional fluorescence lifetime tomography. Medical Physics 32, 992-1000.

Haeussinger, F.B., Heinzel, S., Hahn, T., Schecklmann, M., Ehlis, A.C., Fallgatter, A.J., 2011. Simulation of near-infrared light absorption considering individual head and prefrontal cortex anatomy: implications for optical neuroimaging. PLoS One 6, e26377.

Harada, H., Nashihara, H., Morozumi, K., Ota, H., Hatakeyama, E., 2007. A comparison of cerebral activity in the prefrontal region between young adults and the elderly while driving. Journal of Physiological Anthropology 26, 409-414.

Hiraoka, M., Firbank, M., Essenpreis, M., Cope, M., Arridge, S.R., van der Zee, P., Delpy, D.T., 1993. A Monte Carlo investigation of optical pathlength in inhomogeneous tissue and its application to near-infrared spectroscopy. Physics in Medicine and Biology 38, 1859-1876.

Hirosaka, R., Katura, T., Kawaguchi, H., Tanaka, N., Iwamoto, M., 2004. Noisy time-delayed decorrelation and its application to extraction of neural activity from single optical recordings in guinea pigs. Physica D: Nonlinear Phenomena 194, 320-332.

Homae, F., Watanabe, H., Otobe, T., Nakano, T., Go, T., Konishi, Y., Taga, G., 2010. Development of global cortical networks in early infancy. The Journal of Neuroscience 30, 4877-4882.

Holper, L., Scholkmann, F., Wolf, M., 2012. Between-brain connectivity during imitation measured by fNIRS. NeuroImage 63, 212-222.

Hoshi, Y., Tamura, M., 1993. Detection of dynamic changes in cerebral oxygenation coupled to neuronal function during mental work in man. Neuroscience Letters 150, 5-8.

Hoshi, Y., Kobayashi, N., Tamura, M., 2001. Interpretation of near-infrared spectroscopy signals: a study with a newly developed perfused rat brain model. Journal of Applied Physiology 90, 1657-1662.

Hoshi, Y., Shimada, M., Sato, C., Iguchi, Y., 2005. Reevaluation of near-infrared light propagation in the adult human head: implications for functional near-infrared spectroscopy. Journal of Biomedical Optics 10, 064032.

Hoshi, Y., 2007. Functional near-infrared spectroscopy: current status and future prospects. Journal of Biomedical Optics 12, 062106.

Hoshi, Y., 2011. Towards the next generation of near-infrared spectroscopy. Philosophical Transactions of the Royal Society A 369, 4425-4439.

Ito, Y., Kennan, R.P., Watanabe, E., Koizumi, H., 2000. Assessment of heating effects in skin during continuous wave near infrared spectroscopy. Journal of Biomedical Optics 5, 383-390.

Jasper, H.H., 1958. The ten twenty electrode system of the International Federation. Electroencephalography and Clinical Neurophysiology 10, 371-375.

Jöbsis, F.F., 1977. Noninvasive, infrared monitoring of cerebral and myocardial oxygen sufficiency and circulatory parameters. Science 198, 1264-1267.

Kameyama, M., Fukuda, M., Yamagishi, Y., Sato, T., Uehara, T., Ito, M., Suto, T., Mikuni, M., 2006. Frontal lobe function in bipolar disorder: a multichannel near-infrared spectroscopy study. Neuroimage 29, 172-184.

Kato, T., Kamei, A., Takashima, S., Ozaki, T., 1993. Human visual cortical function during photic stimulation monitoring by means of near-infrared spectroscopy. Journal of Cerebral Blood Flow & Metabolism 13, 516-520.

Katura, T., Tanaka, N., Obata, A., Sato, H., Maki, A., 2006. Quantitative evaluation of

interrelations between spontaneous low-frequency oscillations in cerebral hemodynamics and systemic cardiovascular dynamics. Neuroimage 31, 1592-1600.

Katura, T., Sato, H., Fuchino, Y., Yoshida, T., Atsumori, H., Kiguchi, M., Maki, A., Abe, M., Tanaka, N., 2008. Extracting task-related activation components from optical topography measurement using independent components analysis. Journal of Biomedical Optics 13, 054008.

Kiguchi, M., Ichikawa, N., Atsumori, H., Kawaguchi, F., Sato, H., Maki, A., Koizumi, H., 2007. Comparison of light intensity on the brain surface due to laser exposure during optical topography and solar irradiation. Journal of Biomedical Optics 12, 062108.

Kiguchi, M., Atsumori, H., Fukasaku, I., Kumagai, Y., Funane, T., Maki, A., Kasai, Y., Ninomiya, A., 2012. Wearable NIRS imager for haired region," Review of Scientific Instruments 83, 056101.

Kim, J.G., Liu, H., 2008. Investigation of biphasic tumor oxygen dynamics induced by hyperoxic gas intervention: the dynamic phantom approach. Applied Optics 47, 242-252.

Kirilina, E., Jelzow, A., Heine, A., Niessing, M., Wabnitz, H., Bruhl, R., Ittermann, B., Jacobs, A.M., Tachtsidis, I., 2012. The physiological origin of task-evoked systemic artefacts in functional near infrared spectroscopy. Neuroimage 61, 70-81.

Koh, P.H., Elwell, C.E., Delpy, D.T., 2009. Development of a dynamic test phantom for optical topography. Advances in Experimental Medicine and Biology 645, 141-146.

Kohno, S., Miyai, I., Seiyama, A., Oda, I., Ishikawa, A., Tsuneishi, S., Amita, T., Shimizu, K., 2007. Removal of the skin blood flow artifact in functional near-infrared spectroscopic imaging data through independent component analysis. Journal of Biomedical Optics 12, 062111.

Kohri, S., Hoshi, Y., Tamura, M., Kato, C., Kuge, Y., Tamaki, N., 2002. Quantitative evaluation of the relative contribution ratio of cerebral tissue to near-infrared

signals in the adult human head: a preliminary study. Physiological Measurement 23, 301-312.

Koizumi, H., Yamashita, Y., Maki, A., Yamamoto, T., Ito, Y., Itagaki, H., Kennan, R.P., 1999. Higher-order brain function analysis by trans-cranial dynamic near-infrared spectroscopy imaging. Journal of Biomedical Optics 4, 403-413.

Koizumi, H., Yamamoto, T., Maki, A., Yamashita, Y., Sato, H., Kawaguchi, H., Ichikawa, N., 2003. Optical Topography: Practical Problems and New Applications. Applied Optics 42, 3054-3062.

Konecky, S.D., Panasyuk, G.Y., Lee, K., Markel, V., Yodh, A.G., Schotland, J.C., 2008. Imaging complex structures with diffuse light. Optics Express 16, 5048-5060.

Kou, L., Labrie, D., Chylek, P., 1993. Refractive indices of water and ice in the 0.65- to 2.5 -μm spectral range. Applied Optics 32, 3531-3540.

Krüger, A., Koch, S.P., Mehnert, J., Habermehl, C., Piper, S., Steinbrink, J., Obrig, H., Schmitz, C.H., 2012. Imaging of Motor Activity in Freely Moving Subjects Using a Wearable NIRS Imaging System. Biomedical Optics. Optical Society of America, p. BM4A.3.

Kurth, C.D., Liu, H., Thayer, W.S., Chance, B., 1995. A dynamic phantom brain model for near-infrared spectroscopy. Physics in Medicine and Biology 40, 2079-2092.

Lohwasser, R., Soelkner, G., 1999. Experimental and theoretical laser-Doppler frequency spectra of a tissuelike model of a human head with capillaries. Applied Optics 38, 2128-2137.

Maki, A., Yamashita, Y., Ito, Y., Watanabe, E., Mayanagi, Y., Koizumi, H., 1995. Spatial and temporal analysis of human motor activity using noninvasive NIR topography. Medical Physics 22, 1997-2005.

Matcher, S.J., Elwell, C.E., Cooper, C.E., Cope, M., Delpy, D.T., 1995a. Performance comparison of several published tissue near-infrared spectroscopy algorithms. Analytical Biochemistry 227, 54-68.

Matcher, S.J., Kirkpatrick, P.J., Nahid, K., Cope, M., Delpy, D.T., 1995b. Absolute

quantification methods in tissue near-infrared spectroscopy. Optical Tomography, Photon Migration, and Spectroscopy of Tissue and Model Media: Theory, Human Studies, and Instrumentation. SPIE, San Jose, CA, USA, pp. 486-495.

Mayer, R.H., Reynolds, J.S., Sevick-Muraca, E.M., 1999. Measurement of the Fluorescence Lifetime in Scattering Media by Frequency-Domain Photon Migration. Applied Optics 38, 4930-4938.

Mazurenka, M., Jelzow, A., Wabnitz, H., Contini, D., Spinelli, L., Pifferi, A., Cubeddu, R., Mora, A.D., Tosi, A., Zappa, F., Macdonald, R., 2012. Non-contact time-resolved diffuse reflectance imaging at null source-detector separation. Optics Express 20, 283-290.

Molgedey, L., Schuster, H.G., 1994. Separation of a mixture of independent signals using time delayed correlations. Physical Review Letters 72, 3634-3637.

Niwayama, M., Lin, L., Shao, J., Kudo, N., Yamamoto, K., 2000. Quantitative measurement of muscle hemoglobin oxygenation using near-infrared spectroscopy with correction for the influence of a subcutaneous fat layer. Review of Scientific Instruments 71, 4571-4575.

Niwayama, M., Murata, H., Shinohara, S., 2006. Noncontact tissue oxygenation measurement using near-infrared spectroscopy. Review of Scientific Instruments 77, 073102.

Niwayama, M., Murata, H., Sone, S., Shinohara, S., 2007. Noncontact measurement of deep tissue absorption coefficient using Spatially Resolved Near-Infrared Spectroscopy. IEEJ Transactions on Electrical and Electronic Engineering 2, 485-487.

Obata, A., Morimoto, K., Sato, H., Maki, A., Koizumi, H., 2003. Acute effects of alcohol on hemodynamic changes during visual stimulation assessed using 24-channel near-infrared spectroscopy. Psychiatry Research: Neuroimaging 123, 145-152.

Obata, A., Morimoto, K., Sato, H., Takeshita, T., Kawaguchi, H., Koizumi, H., Maki, A., 2005. Effects of alcohol on hemodynamic and cardiovascular reaction in

different genotypes. Psychiatry Research: Neuroimaging 139, 65-72.

Okada, E., Firbank, M., Schweiger, M., Arridge, S.R., Cope, M., Delpy, D.T., 1997. Theoretical and experimental investigation of near-infrared light propagation in a model of the adult head. Applied Optics 36, 21-31.

Okada, E., Delpy, D.T., 2003. Near-infrared light propagation in an adult head model. I. Modeling of low-level scattering in the cerebrospinal fluid layer. Applied Optics 42, 2906-2914.

Okada, E., Delpy, D.T., 2003. Near-Infrared Light Propagation in an Adult Head Model. II. Effect of Superficial Tissue Thickness on the Sensitivity of the Near-Infrared Spectroscopy Signal. Applied Optics 42, 2915-2922.

Panerai, R.B., Moody, M., Eames, P.J., Potter, J.F., 2005. Dynamic cerebral autoregulation during brain activation paradigms. American Journal of Physiology - Heart and Circulatory Physiology 289, H1202-1208.

Patterson, M.S., Chance, B., Wilson, B.C., 1989. Time resolved reflectance and transmittance for the noninvasive measurement of tissue optical properties. Applied Optics 28, 2331-2336.

Perrey, S., 2008. Non-invasive NIR spectroscopy of human brain function during exercise. Methods 45, 289-299.

Pfurtscheller, G., Bauernfeind, G., Wriessnegger, S.C., Neuper, C., 2010. Focal frontal (de)oxyhemoglobin responses during simple arithmetic. International Journal of Psychophysiology 76, 186-192.

Pogue, B.W., Patterson, M.S., 2006. Review of tissue simulating phantoms for optical spectroscopy, imaging and dosimetry. Journal of Biomedical Optics 11, 041102.

Quaresima, V., Lepanto, R., Ferrari, M., 2003. The use of near infrared spectroscopy in sports medicine. The Journal of Sports Medicine and Physical Fitness 43, 1-13.

Rea, P.A., Crowe, J., Wickramasinghe, Y., Rolfe, P., 1985. Non-invasive optical methods for the study of cerebral metabolism in the human newborn: a technique for the future? Journal of Medical Engineering & Technology 9, 160-166.

Roy, R., Thompson, A.B., Godavarty, A., Sevick-Muraca, E.M., 2005. Tomographic fluorescence imaging in tissue phantoms: a novel reconstruction algorithm and imaging geometry. IEEE Transactions on Medical Imaging 24, 137-154.

Saager, R.B., Berger, A.J., 2005. Direct characterization and removal of interfering absorption trends in two-layer turbid media. Journal of Optical society of America A 22, 1874-1882.

Saager, R., Berger, A., 2008. Measurement of layer-like hemodynamic trends in scalp and cortex: implications for physiological baseline suppression in functional near-infrared spectroscopy. Journal of Biomedical Optics 13, 034017.

Saager, R.B., Telleri, N.L., Berger, A.J., 2011. Two-detector Corrected Near Infrared Spectroscopy (C-NIRS) detects hemodynamic activation responses more robustly than single-detector NIRS. Neuroimage 55, 1679-1685.

Sase, I., Takatsuki, A., Seki, J., Yanagida, T., Seiyama, A., 2006. Noncontact backscatter-mode near-infrared time-resolved imaging system: Preliminary study for functional brain mapping. Journal of Biomedical Optics 11, 054006.

Sato, H., Takeuchi, T., Sakai, K.L., 1999. Temporal cortex activation during speech recognition: an optical topography study. Cognition 73, B55-66.

Sato, H., Kiguchi, M., Kawaguchi, F., Maki, A., 2004. Practicality of wavelength selection to improve signal-to-noise ratio in near-infrared spectroscopy. Neuroimage 21, 1554-1562.

Sato, H., Kiguchi, M., Maki, A., 2006. Wavelength dependence of effective pathlength factor in noninvasive optical measurements of human brain functions. Japanese Journal of Applied Physics 45, L361-363.

Sato, H., Aoki, R., Katura, T., Matsuda, R., Koizumi, H., 2011. Correlation of within-individual fluctuation of depressed mood with prefrontal cortex activity during verbal working memory task: optical topography study. Journal of Biomedical Optics 16, 126007.

Sawosz, P., Kacprzak, M., Zolek, N., Weigl, W., Wojtkiewicz, S., Maniewski, R., Liebert, A., 2010. Optical system based on time-gated, intensified charge-coupled device camera for brain imaging studies. Journal of Biomedical

Optics 15, 066025.

Schulz, R.B., Ripoll, J., Ntziachristos, V., 2003. Noncontact optical tomography of turbid media. Optics Letters 28, 1701-1703.

Sevick-Muraca, E.M., Lopez, G., Reynolds, J.S., Troy, T.L., Hutchinson, C.L., 1997. Fluorescence and absorption contrast mechanisms for biomedical optical imaging using frequency-domain techniques. Photochemistry and Photobiology 66, 55-64.

Shionoya, S., Yen, W.M., 1998. Phosphor Handbook. CRC Press, Boca Raton, FL.

Smielewski, P., Czosnyka, M., Pickard, J.D., Kirkpatrick, P., 1997. Clinical evaluation of near-infrared spectroscopy for testing cerebrovascular reactivity in patients with carotid artery disease. Stroke 28, 331-338.

Suda, M., Takei, Y., Aoyama, Y., Narita, K., Sato, T., Fukuda, M., Mikuni, M., 2010. Frontopolar activation during face-to-face conversation: An in situ study using near-infrared spectroscopy. Neuropsychologia 48, 441-447.

Suto, T., Fukuda, M., Ito, M., Uehara, T., Mikuni, M., 2004. Multichannel near-infrared spectroscopy in depression and schizophrenia: cognitive brain activation study. Biological Psychiatry 55, 501-511.

Suzuki, A., Jeser, J.-P., 1978. Fluorescent material. United States Patent No. 4107273.

Suzuki, A., Kashiwada, Y., Tanimizu, S., 1979. Concentration Quenching of ND^{3+}— Luminescence in $Li(Nd_{1-x}Yb_x)P_4O_{12}$. Journal of The Electrochemical Society 126, 131C-132C.

Suzuki, S., Takasaki, S., Ozaki, T., Kobayashi, Y., 1999. A Tissue Oxygenation Monitor using NIR Spatially Resolved Spectroscopy. Proceedings of SPIE 3597, 582-592.

Tachtsidis, I., Leung, T.S., Devoto, L., Delpy, D.T., Elwell, C.E., 2008. Measurement of frontal lobe functional activation and related systemic effects: a near-infrared spectroscopy investigation. Advances in Experimental Medicine and Biology 614, 397-403.

Tachtsidis, I., Leung, T.S., Chopra, A., Koh, P.H., Reid, C.B., Elwell, C.E., 2009. False positives in functional near-infrared topography. Advances in

Experimental Medicine and Biology 645, 307-314.

Taga, G., Konishi, Y., Maki, A., Tachibana, T., Fujiwara, M., Koizumi, H., 2000. Spontaneous oscillation of oxy- and deoxy- hemoglobin changes with a phase difference throughout the occipital cortex of newborn infants observed using non-invasive optical topography. Neuroscience Letters 282, 101-104.

Taga, G., Asakawa, K., Maki, A., Konishi, Y., Koizumi, H., 2003. Brain imaging in awake infants by near-infrared optical topography. Proceedings of the National Academy of Sciences of the United States of America 100, 10722-10727.

Takahashi, T., Takikawa, Y., Kawagoe, R., Shibuya, S., Iwano, T., Kitazawa, S., 2011. Influence of skin blood flow on near-infrared spectroscopy signals measured on the forehead during a verbal fluency task. Neuroimage 57, 991-1002.

Thompson, A.B., Hawrysz, D.J., Sevick-Muraca, E.M., 2003. Near-Infrared Fluorescence Contrast-Enhanced Imaging with Area Illumination and Area Detection: The Forward Imaging Problem. Applied Optics 42, 4125-4136.

Tomioka, H., Yamagata, B., Takahashi, T., Yano, M., Isomura, A.J., Kobayashi, H., Mimura, M., 2009. Detection of hypofrontality in drivers with Alzheimer's disease by near-infrared spectroscopy. Neuroscience Letters 451, 252-256.

Tong, Y., Hocke, L.M., Frederick, B.d., 2011. Isolating the sources of widespread physiological fluctuations in functional near-infrared spectroscopy signals. Journal of Biomedical Optics 16, 106005.

Toronov, V., Franceschini, M.A., Filiaci, M., Fantini, S., Wolf, M., Michalos, A., Gratton, E., 2000. Near-infrared study of fluctuations in cerebral hemodynamics during rest and motor stimulation: temporal analysis and spatial mapping. Medical Physics 27, 801-815.

Toronov, V., Webb, A., Choi, J.H., Wolf, M., Safonova, L., Wolf, U., Gratton, E., 2001. Study of local cerebral hemodynamics by frequency-domain near-infrared spectroscopy and correlation with simultaneously acquired functional magnetic resonance imaging. Optics Express 9, 417-427.

Tsujimoto, S., Yamamoto, T., Kawaguchi, H., Koizumi, H., Sawaguchi, T., 2004. Prefrontal cortical activation associated with working memory in adults and

preschool children: an event-related optical topography study. Cerebral Cortex 14, 703-712.

Turner, G.M., Zacharakis, G., Soubret, A., Ripoll, J., Ntziachristos, V., 2005. Complete-angle projection diffuse optical tomography by use of early photons. Optics Letters 30, 409-411.

Umeyama, S., Yamada, T., 2009. Monte Carlo study of global interference cancellation by multidistance measurement of near-infrared spectroscopy. Journal of Biomedical Optics 14, 064025.

Utsugi, K., Obata, A., Sato, H., Aoki, R., Maki, A., Koizumi, H., Sagara, K., Kawamichi, H., Atsumori, H., Katura., T., 2008. GO-STOP Control Using Optical Brain-Computer Interface during Calculation Task. IEICE transactions on communications 91, 2133-2141.

van Beekvelt, M.C., Borghuis, M.S., van Engelen, B.G., Wevers, R.A., Colier, W.N., 2001. Adipose tissue thickness affects *in vivo* quantitative near-IR spectroscopy in human skeletal muscle. Clinical Science 101, 21-28.

van der Zee, P., Delpy, D.T., 1987. Simulation of the point spread function for light in tissue by a Monte Carlo Method. Advances in Experimental Medicine and Biology 215, 179-191.

Villringer, A., Planck, J., Hock, C., Schleinkofer, L., Dirnagl, U., 1993. Near infrared spectroscopy (NIRS): a new tool to study hemodynamic changes during activation of brain function in human adults. Neuroscience Letters 154, 101-104.

Virtanen, J., Noponen, T., Merilainen, P., 2009. Comparison of principal and independent component analysis in removing extracerebral interference from near-infrared spectroscopy signals. Journal of Biomedical Optics 14, 054032.

Wang, L., Jacques, S.L., Zheng, L., 1995. MCML--Monte Carlo modeling of light transport in multi-layered tissues. Computer Methods and Programs in Biomedicine 47, 131-146.

Wang, S., Shibahara, N., Kuramashi, D., Okawa, S., Kakuta, N., Okada, E., Maki, A., Yamada, Y., 2010. Effects of spatial variation of skull and cerebrospinal fluid

layers on optical mapping of brain activities. Optical Review 17, 410-420.

Wang, Z.-M., Panasyuk, G.Y., Markel, V.A., Schotland, J.C., 2005. Experimental demonstration of an analytic method for image reconstruction in optical diffusion tomography with large data sets. Optics Letters 30, 3338-3340.

Watanabe, E., Maki, A., Kawaguchi, F., Takashiro, K., Yamashita, Y., Koizumi, H., Mayanagi, Y., 1998. Non-invasive assessment of language dominance with near-infrared spectroscopic mapping. Neuroscience Letters 256, 49-52.

Watanabe, E., Maki, A., Kawaguchi, F., Yamashita, Y., Koizumi, H., Mayanagi, Y., 2000. Noninvasive cerebral blood volume measurement during seizures using multichannel near infrared spectroscopic topography. Journal of Biomedical Optics 5, 287-290.

Wyatt, J.S., Delpy, D.T., Cope, M., Wray, S., Reynolds, E.O.R., 1986. Quantification of Cerebral Oxygenation and Haemodynamics in Sick Newborn Infants by Near Infrared Spectrophotometry. The Lancet 328, 1063-1066.

Yamada, T., Umeyama, S., Matsuda, K., 2009. Multidistance probe arrangement to eliminate artifacts in functional near-infrared spectroscopy. Journal of Biomedical Optics 14, 064034.

Yamashita, Y., Maki, A., Koizumi, H., 1996. Near-infrared topographic measurement system: Imaging of absorbers localized in a scattering medium. Review of Scientific Instruments 67, 730-732.

Yang, Y., Soyemi, O.O., Landry, M.R., Soller, B.R., 2005. Influence of a fat layer on the near infrared spectra of human muscle: quantitative analysis based on two-layered Monte Carlo simulations and phantom experiments. Optics Express 13, 1570-1579.

Zhang, Q., Brown, E.N., Strangman, G.E., 2007a. Adaptive filtering for global interference cancellation and real-time recovery of evoked brain activity: a Monte Carlo simulation study. Journal of Biomed Optics 12, 044014.

Zhang, Q., Brown, E.N., Strangman, G.E., 2007b. Adaptive filtering to reduce global interference in evoked brain activity detection: a human subject case study. Journal of Biomedical Optics 12, 064009.

Zhang, Q., Strangman, G.E., Ganis, G., 2009. Adaptive filtering to reduce global interference in non-invasive NIRS measures of brain activation: How well and when does it work? Neuroimage 45, 788-794.

Zhang, R., Zuckerman, J.H., Giller, C.A., Levine, B.D., 1998. Transfer function analysis of dynamic cerebral autoregulation in humans. American Journal of Physiology - Heart and Circulatory Physiology 274, H233-H241.

Zhang, Y., Books, D.H., Franceschini, M.A., Boas, D.A., 2005. Eigenvector-based spatial filtering for reduction of physiological interference in diffuse optical imaging. Journal of Biomedical Optics 10, 011014.

Zhang, Y., Sun, J., Rolfe, P., 2011. Reduction of global interference in functional multidistance near-infrared spectroscopy using empirical mode decomposition and recursive least squares: a Monte Carlo study. Journal of the European Optical Society - Rapid Publications 6, 11033.

Ziehe, A., Müller, K., 1998. TDSEP -- an efficient algorithm for blind separation using time structure. Proceedings of ICANN 98. Springer Verlag, Berlin, pp. 675–680.

Acknowledgments

This work was done at the Graduate School of Science and Technology, Keio University. I would like to express my deep gratitude to my research supervisor, Professor Eiji Okada, for his thoughtful advice, unwavering support, and helpful discussions. I am also grateful to the rest of my thesis committee—Professor Nozomu Hamada, Professor Masaaki Ikehara, and Associate Professor Junichi Ushiba—for their helpful suggestions and insightful comments, which have helped to greatly improve this thesis.

I thank the members of the Okada Laboratory for giving me many suggestions and posing tough questions, which were invaluable for improving this research.

I would like to thank the team at Hitachi, Ltd., Central Research Laboratory, especially Dr. Hideaki Koizumi, Dr. Masashi Kiguchi, Dr. Kisou Kubota, and Dr. Atsushi Maki for fruitful discussions and a wealth of advice. Furthermore, I am deeply grateful to my colleagues at Hitachi, Ltd.—Dr. Hirokazu Atsumori, Dr. Hiroki Sato, Dr. Takusige Katura, Dr. Akiko N. Obata, Dr. Daisuke Suzuki, Dr. Yusuke Seki, Mr. Tsuyoshi Miyashita, Mr. Kuniaki Ozawa, Dr. Kunihiko Kido, Ms. Yukiko Ichige, Dr. Yukiko Hirabayashi, Mr. Yu Saito, Dr. Tsuyoshi Yamamoto, Dr. Tatsuya Tomaru, Dr. Toru Fujimura, Dr. Kei Utsugi, and Ms. Yukari Yamamoto—who gave me valuable advice and friendly help.

Moreover, I would like to thank my former colleagues at Hitachi, Ltd. for their

generous help in this research: Professor Naoki Tanaka, Professor Hideo Kawaguchi, Associate Professor Hirokazu Tanaka, Associate Professor Kyoko Yamazaki, Dr. Takamasa Yoshida, Dr. Yutaka Fuchino, Dr. Mariko Uchida, Dr. Miyuki Suda, and Dr. Ryuta Aoki.

I thank the people in the optical topography team at Hitachi Medical Corporation for their technical advices and useful suggestions.

I am deeply grateful to Dr. Toyoshige Kobayashi, Mr. Ryota Nakajima, Dr. Masaki Ikeda, Mr. Akio Iioka, and Mr. Ryosuke Takahashi for their kind support and invaluable guidance during my time at Hatoyama.

I would like to express my sincere gratitude to Ms. Yukari Tanikawa from The National Institute of Advanced Industrial Science and Technology for measuring the optical properties of the phantom that I prepared, and for useful discussions.

I thank Dr. Hiromichi Yamada and Dr. Atsushi Suzuki for preparing the phosphor, which was an indispensable material in my research. I also thank Dr. Toru Hisamitsu, Dr. Kazuo Saitoh, Dr. Minoru Sakairi, and Dr. Nobuyuki Osakabe for their general support. I would like to express my appreciation to Mr. Noboru Moriya and Mr. Keisuke Mori for their technical assistance and support in preparing the phantom and other experimental setups.

I would like to thank Ms. Norie Odaka, Ms. Mika Yonemitsu, Mr. Tadahiro Horita, Ms. Yukie Shimada, Ms. Rie Komine, and Dr. Yuko Isogaya for their general support and technical assistance.

I am also grateful to Professor Shin-ichi Nakasuka, who was my teacher when I was an undergraduate and master's student at the University of Tokyo, for giving me the motivation to go into brain research.

I gratefully acknowledge the Keio Leading-edge Laboratory of Science and Technology Ph.D. Program Research Grant.

Lastly I wish to thank my family. They showed me what's important in life. I thank Madoka, my wife, for her continuous support. In addition, I thank Madoka's parents, Mr. and Mrs. Kayama, for their understanding and valuable help. Further, I

wish to thank my parents, Kiyoshi and Hideko, my older brother, Shinichiro, and my younger sister, Rei, for supporting and encouraging me every step of the way.

Tsukasa Funane

List of publications

Original papers related to this doctoral dissertation

1. Funane, T., Atsumori, H., Suzuki, A., Kiguchi, M., 2010. Noncontact brain activity measurement system based on near-infrared spectroscopy. Applied Physics Letters 96, 123701/1-3.
2. Funane, T., Atsumori, H., Suzuki, A., Kiguchi, M., 2011. Noncontact optical brain activity measurement system using phosphor placed on skin. Japanese Journal of Applied Physics 50, 077001/1-9.
3. Funane, T., Atsumori, H., Kiguchi, M., Tanikawa, Y., Okada, E., 2011. Optical scanning system for light-absorption measurement of deep biological tissue. Review of Scientific Instruments 82, 093101/1-8.
4. Funane, T., Atsumori, H., Kiguchi, M., Tanikawa, Y., Okada, E., 2012. Dynamic phantom with two stage-driven absorbers for mimicking hemoglobin changes in superficial and deep tissues. Journal of Biomedical Optics 17, 047001/1-11.

Other articles

1. Nakasuka, S., Funane, T., Nakamura, Y., Nojiri, Y., Sahara, H., Sasaki, F., Kaya, N., 2006. Sounding rocket flight experiment for demonstrating "Furoshiki Satellite" for large phased array antenna. Acta Astronautica 59, 200-205.
2. Funase, R., Takei, E., Nakamura, Y., Nagai, M., Enokuchi, A., Yuliang, C., Nakada, K., Nojiri, Y., Sasaki, F., Funane, T., Eishima, T., Nakasuka, S., 2007. Technology demonstration on University of Tokyo's pico-satellite "XI-V" and its effective operation result using ground station network. Acta Astronautica 61, 707-711.
3. Funane, T., Atsumori, H., Sato, H., Kiguchi, M., Maki, A., 2009. Multi-wavelength measurement of cytochrome oxidase and water in biomedical tissues using optical topography system. Proceedings of SPIE 7174, 71740A/1-9.
4. Funane, T., Atsumori, H., Sato, H., Kiguchi, M., Maki, A., 2009. Relationship between wavelength combination and signal-to-noise ratio in measuring hemoglobin concentrations using visible or near-infrared light. Optical Review 16, 442-448.
5. Atsumori, H., Kiguchi, M., Obata, A., Sato, H., Katura, T., Funane, T., Maki, A., 2009. Development of wearable optical topography system for mapping the prefrontal cortex activation. Review of Scientific Instruments 80, 043704/1-6.
6. Atsumori, H., Kiguchi, M., Katura, T., Funane, T., Obata, A., Sato, H., Manaka, T., Iwamoto, M., Maki, A., Koizumi, H., Kubota, K., 2010. Noninvasive imaging of prefrontal activation during attention-demanding tasks performed while walking using a wearable optical topography system. Journal of Biomedical Optics 15, 046002/1-7.
7. Aoki, R., Funane, T., Koizumi, H., 2010. Brain Science of Ethics: Present Status and the Future. Mind, brain, and education 4, 188-195.

8. Funane, T., Kiguchi, M., Atsumori, H., Sato, H., Kubota, K., Koizumi, H., 2011. Synchronous activity of two people's prefrontal cortices during a cooperative task measured by simultaneous near-infrared spectroscopy. Journal of Biomedical Optics 16, 077011/1-10.
9. Kiguchi, M., Atsumori, H., Fukasaku, I., Kumagai, Y., Funane, T., Maki, A., Kasai, Y., Ninomiya, A., 2012. Note: Wearable near-infrared spectroscopy imager for haired region. Review of Scientific Instruments 83, 056101/1-3.

Appendix

Calculation of Hb change by modified Beer-Lambert law

The method for calculating Hb using multiple wavelengths of absorbance changes is described below. Given that the number of measurement components is N ($b_1 \cdots b_N$) and that of wavelengths is M ($\lambda_1 \cdots \lambda_M$), according to modified Beer-Lambert law (Delpy et al., 1988; Maki et al., 1995), optical density $OD(\lambda)$ (i.e., absorbance) can be expressed as

$$\begin{aligned} OD(\lambda) &= -\ln\left[\frac{I(\lambda)}{I_0(\lambda)}\right] \\ &= \varepsilon_{b_1}(\lambda)C_{b_1}L + \cdots + \varepsilon_{b_N}(\lambda)C_{b_N}L + a_{other}(\lambda)L + s(\lambda), \end{aligned} \tag{34}$$

where $I_0(\lambda)$ and $I(\lambda)$ denote the intensity of incident and transmitted light, respectively, $\varepsilon_{b_1}(\lambda), \cdots, \varepsilon_{b_N}(\lambda)$ denote extinction coefficients (based on natural

logarithm), $C_{b_1},\cdots, C_{b_N}$ denote the concentration of each substance in the living body, L denotes the effective optical path length, $a_{other}(\lambda)$ denotes optical loss by other absorbers, and $s(\lambda)$ denotes loss by scattering in the tissue. The superscript "*base*" indicates the baseline, and $OD^{base}(\lambda)$ can be expressed as

$$\begin{aligned} OD^{base}(\lambda) &= -\ln\left[\frac{I^{base}(\lambda)}{I_0(\lambda)}\right] \\ &= \varepsilon_{b_1}(\lambda)C_{b_1}^{base}L+\cdots+\varepsilon_{b_N}(\lambda)C_{b_N}^{base}L+a_{other}^{base}(\lambda)L+s(\lambda). \end{aligned} \tag{35}$$

Here, if

$$a_{other}(\lambda)=a_{other}^{base}(\lambda), \tag{36}$$

by subtracting Eq. (35) from Eq. (34), we have

$$\Delta OD = OD(\lambda)-OD^{base}(\lambda)=\log_{10}\left[\frac{I(\lambda)}{I^{base}(\lambda)}\right] \tag{37}$$

$$= \varepsilon_{b_1}(\lambda)\Delta C_{b_1}+\cdots+\varepsilon_{b_N}(\lambda)\Delta C_{b_N}, \tag{38}$$

where

$$\begin{cases} \Delta C_{b_1}=\left(C_{b_1}-C_{b_1}^{base}\right)L \\ \quad\vdots \\ \Delta C_{b_N}=\left(C_{b_N}-C_{b_N}^{base}\right)L \end{cases}. \tag{39}$$

The variables can then be expressed in matrix form as

$$\mathbf{A} = \left[\Delta OD(\lambda_1) \quad \cdots \quad \Delta OD(\lambda_M)\right], \tag{40}$$

$$\mathbf{C} = \left[\Delta C_{b_1} \quad \cdots \quad \Delta C_{b_N}\right], \tag{41}$$

$$\mathbf{K} = \begin{bmatrix} \varepsilon_{b_1}(\lambda_1) & \cdots & \varepsilon_{b_1}(\lambda_M) \\ \vdots & \ddots & \vdots \\ \varepsilon_{b_N}(\lambda_1) & \cdots & \varepsilon_{b_N}(\lambda_M) \end{bmatrix}, \tag{42}$$

such that the following equation holds:

$$\mathbf{A} = \mathbf{CK} . \tag{43}$$

Furthermore, the next equation is obtained:

$$\mathbf{AK}^T = \mathbf{CKK}^T \tag{44}$$

$$\therefore \mathbf{C} = \mathbf{AK}^T(\mathbf{KK}^T)^{-1} . \tag{45}$$

Equation (45) holds only when $2 \le N \le M$. Given that

$$\mathbf{K}^T(\mathbf{KK}^T)^{-1} \equiv \mathbf{F} = \begin{bmatrix} F_{11} & \cdots & F_{1N} \\ \vdots & \ddots & \vdots \\ F_{M1} & \cdots & F_{MN} \end{bmatrix}, \tag{46}$$

the concentration change of a substance can then be calculated as

$$\begin{cases} \Delta C_{b_1} = F_{11}\Delta OD(\lambda_1) + \cdots + F_{M1}\Delta OD(\lambda_M) \\ \qquad\qquad \vdots \\ \Delta C_{b_N} = F_{1N}\Delta OD(\lambda_1) + \cdots + F_{MN}\Delta OD(\lambda_M) \end{cases} . \tag{47}$$

Monte Carlo simulation

In a Monte Carlo simulation of photon migration in a scattering medium (Okada et al., 1997; Wang et al., 1995), the light is treated as a photon packet. From the optical properties of the tissue (absorption, scattering coefficients, anisotropic parameter, and refraction index), the behavior of an individual photon packet is calculated statistically by using random variables. The analysis is based on the assumption that a photon packet migrates in biological tissue with a random change of direction each time it is scattered, and that the light intensity decreases due to absorption by the tissue with increasing migration distance.

The Monte Carlo algorithm used in this research is based on the variance reduction technique (Hiraoka et al., 1993; van der Zee and Delpy, 1987). In this technique, when the scattering coefficient of a tissue is μ_s, the distance until the photon experiences the next scattering in the tissue is determined by using Eq. (48) with the random variable R $(0 < R \leq 1)$:

$$l = -\frac{\ln R}{\mu_s}. \tag{48}$$

When a photon packet passes through a boundary between tissues that have different μ_s values, the photon packet moves to the boundary position and scatters again from the boundary position in accordance with another random value.

The scattering direction (θ) is usually determined by the Henyey-Greenstein phase function:

$$p(\theta) = \frac{1}{4\pi} \frac{1 - g^2}{\left[1 + g^2 - 2g\cos\theta\right]^{3/2}}. \tag{49}$$

When the object is a turbid medium such as head tissue ($\mu_a << \mu'_s$) and the source-detector distance (ρ) is sufficiently large ($\rho >> \mu_s$), the approximation of isotropic scattering can be applied (Haeussinger et al., 2011). The scattering direction is thus determined by random values for all the directions. The scattering process is repeated until a photon packet exceeds the boundary of the model or the number of scatterings exceeds 10,000.

The photon transmittance was calculated as follows. The attenuation ratio of the jth ($1 \leq j \leq 1000$) detected photon At_j is expressed as

$$At_j = \exp\left(-\sum_i \left(L_{ij}\mu_{ai}\right)\right), \tag{50}$$

here L_{ij} denotes the partial optical path length of the jth photon in the ith layer (voxel) and μ_{ai} denotes the absorption coefficient of the ith layer (voxel).

The mean effective optical path length of the ith layer (voxel), L_i^{eff}, can be calculated by averaging the product of the optical path length and attenuation ratio of each photon as follows:

$$L_i^{eff} = \frac{\sum_j \left(At_j L_{ij}\right)}{\sum_j At_j}. \tag{51}$$

The transmittance of a photon, Tr, can be calculated as the ratio of detected intensity (sum of all attenuation ratios) and incident intensity (number of incident photons: Ni):

$$Tr = \frac{\sum_j At_j}{Ni}. \tag{52}$$

Although the Monte Carlo method can be used to analyze photon propagation in models having various shapes and optical properties, long computation times are necessary in order to obtain statistically stable result. It is often necessary to generate a model that has geometric symmetry in order to make the calculation faster.

List of acronyms

A/D	analog-digital
APD	avalanche photodiode
AR	amplitude ratio
BCI	brain-computer interface
CBV	cerebral blood volume
CCD	charge-coupled device
CMOS	complementary metal-oxide semiconductor
CNR	carrier-to-noise ratio
CSF	cerebrospinal fluid
CT	computed tomography
CW	continuous wave
DOT	diffuse optical tomography
DTTCI	3,3’-diethylthiatricarbocyanine iodide
EEG	electroencephalogram
FWHM	full width at half maximum
GPIB	general purpose interface bus
Hb	hemoglobin
ICA	independent component analysis
ICCD	intensified charge-coupled devices
ICG	indocyanine green
InP	indium phosphide

LA	lock-in amplifier
LED	light emitting diode
LD	laser diode
LDF	laser Doppler flowmetry
MRI	magnetic resonance imaging
NIRS	near-infrared spectroscopy
OD	optical density
OT	optical topography
PC	personal computer
PET	positron emission tomography
POM	polyoxymethylene
S-D	source-detector
SNR	signal-to-noise ratio
TDD-ICA	time delayed decorrelation ICA